

12-2010

DESIGN TOOL DEVELOPMENT FOR CELLULAR STRUCTURE SYNthesis TO ACHIEVE DESIRED PROPERTIES

Luke Berglind

Clemson University, lbergli@clemson.edu

Follow this and additional works at: https://tigerprints.clemson.edu/all_theses



Part of the [Art and Design Commons](#)

Recommended Citation

Berglind, Luke, "DESIGN TOOL DEVELOPMENT FOR CELLULAR STRUCTURE SYNthesis TO ACHIEVE DESIRED PROPERTIES" (2010). *All Theses*. 1043.

https://tigerprints.clemson.edu/all_theses/1043

This Thesis is brought to you for free and open access by the Theses at TigerPrints. It has been accepted for inclusion in All Theses by an authorized administrator of TigerPrints. For more information, please contact kokeefe@clemson.edu.

DESIGN TOOL DEVELOPMENT FOR CELLULAR STRUCTURE
SYNTHESIS TO ACHIEVE DESIRED PROPERTIES

A Thesis
Presented to
the Graduate School of
Clemson University

In Partial Fulfillment
of the Requirements for the Degree
Master of Science
Mechanical Engineering

by
Luke Berglind
December 2010

Accepted by:
Dr. Joshua Summers
Dr. John Ziegert
Dr. Paul Joseph

ABSTRACT

The effective properties of cellular materials are dependent both on the fixed material properties of the constituent material and the geometry of the cellular structure. As a result, the effective properties can be altered through geometric modifications without changes to the constituent material. Cellular materials present new opportunities in mechanical design due to the ability to produce new materials with customized properties which can improve the performance of existing designs. However, the task of designing the geometry to achieve desired properties presents additional challenges to the design process.

To increase the viability of customizable cellular materials in new product design, new methods are needed to help designers develop new materials efficiently and effectively. Two such design methods are presented in this thesis; for the design of honeycomb structures to achieve two effective shear properties simultaneously, and for the design of a compliant skin structure to achieve desired shape morphing behavior. The design methods presented here reflect an effort to develop systematic and automatable processes for the design of new cellular materials for two separate applications, using two separate approaches to the design problem.

This thesis discusses the development of both cellular structure design methods and the respective design algorithms created to implement the methods automatically. Numerical analysis is used to test the effectiveness of the methods for their respective design applications and design examples are provided for each method.

DEDICATION

This thesis is dedicated to my friends and family for their continual encouragement during my time as a graduate student, especially to my parents, Larry and Wenda Berglind, for their love and support.

ACKNOWLEDGMENTS

I would like to thank my committee members, Dr. Summers, Dr. Ziegert, and Dr. Joseph, for their support. A special thanks to Dr. Summers, Dr. Ju and the rest of the CEDAR lab for being supportive and encouraging guides throughout this process. Finally, I would like to acknowledge the NIST ATP program for providing financial support for a portion of this research.

TABLE OF CONTENTS

| | |
|--|-----|
| Abstract..... | ii |
| Dedication..... | iii |
| Acknowledgments..... | iv |
| Table of Contents | i |
| List of Tables | iii |
| List of Figures..... | iv |
| Chapter One: Introduction | 1 |
| 1.0 Tweel™ Shear Band..... | 2 |
| 1.1 Shape Morphing Airfoils | 9 |
| 1.2 Summary..... | 13 |
| Chapter Two: Shear Compliant Honeycomb Structure Synthesis | 14 |
| 2.0 Honeycomb Structure Analysis..... | 17 |
| 2.1 Parametric Studies | 28 |
| 2.2 Parameter System Comparison | 37 |
| 2.3 Honeycomb Design Method | 43 |
| 2.4 Honeycomb Design Algorithm | 45 |
| 2.5 Design for Target Shear Properties | 60 |
| 2.6 Honeycomb Design Summary | 73 |
| 2.7 design approach for different cellular topologies..... | 74 |
| Chapter Three: Morphing Skin Cellular Structure Synthesis | 79 |
| 3.1 Compliant Mechanisms | 79 |
| 3.2 Direct Displacement Synthesis..... | 84 |
| 3.3 Morphing Skin Design Using Direct Displacement..... | 88 |
| 3.4 Morphing Skin Design Method..... | 94 |
| 3.5 Morphing Skin Design Algorithm..... | 100 |
| 3.6 Example Problem: Sinusoidal Curve..... | 119 |

| | |
|--|-----|
| 3.7 Morphing Skin Design Summary | 127 |
| Chapter Four: Conclusions and Future work..... | 128 |
| 4.1 Honeycomb Design Method | 128 |
| 4.2 Morphing Skin Design Method..... | 131 |
| References..... | 139 |

LIST OF TABLES

| | |
|--|-----|
| Table 1.1: Shear band material property requirements. | 7 |
| Table 2.1: Conversion equations relating the conventional parameters and the new parameters. | 23 |
| Table 2.2: Structure geometries used in parametric studies for new parameters, R and d | 26 |
| Table 2.3: Structure geometries used in parametric studies for conventional parameters, h and l | 27 |
| Table 2.4: Parametric study data for the new parameters with one vertical cell..... | 31 |
| Table 2.5: Parametric study data for the new parameters with two vertical cells..... | 31 |
| Table 2.6: Parametric study data for the conventional parameters with one vertical cell..... | 37 |
| Table 2.7: Honeycomb design algorithm inputs and outputs | 46 |
| Table 2.8: Structural geometry and effective properties for Figure 2.32. | 65 |
| Table 2.9: Structural geometry and effective properties for Figure 2.33. | 67 |
| Table 2.10: Structural geometry and effective properties for Figure 2.34. | 69 |
| Table 2.11: Data results from Figure 2.32..... | 70 |
| Table 2.13: Resulting properties of the tapered bristle structure designed using analytical solution. | 77 |
| Table 3.1: Summary of the error results for the structure geometric parameters. | 123 |

LIST OF FIGURES

| | |
|---|----|
| Figure 1.1: Michelin Tweel™ | 2 |
| Figure 1.2: Major Tweel™ Components | 3 |
| Figure 1.3: Contact Pressure profile of the Tweel™ | 4 |
| Figure 1.4: Tweel Shear Band | 5 |
| Figure 1.5: Replace homogeneous material with cellular material to reduce hysteretic energy loss. | 6 |
| Figure 1.6: Shear band material property requirements. | 7 |
| Figure 1.7: Topology Optimization Solutions. | 8 |
| Figure 1.8: Chiral and Auxetic honeycombs having negative Poisson's ratio. | 8 |
| Figure 1.9: Variable camber morphing airfoil designed to change shape from the initial profile to the morphed profile. | 10 |
| Figure 1.10: a) Chiral core airfoil, b) Honeycomb core airfoil, c) Internal compliant mechanism airfoil. | 11 |
| Figure 1.11: Morphing airfoil skin design concepts; a) segmented scale design and b) corrugated structure with flexible skin design. | 12 |
| Figure 2.1: Conventional parameters for a two-dimensional honeycomb structure..... | 16 |
| Figure 2.2: Honeycomb structure using the new system of parameters for $N_v=1$ and $N_h=3$ | 17 |
| Figure 2.3: Honeycomb structure reaction to shear loading..... | 19 |
| Figure 2.4: Two structures having equal effective heights, R , and a different number of vertical cells, N_v | 21 |
| Figure 2.5: Outside the range of $0 < R < 2$, the cell wall members begin to overlap. | 21 |
| Figure 2.6: Typical structure analyzed in the parametric studies having 16 horizontal honeycomb cells | 24 |
| Figure 2.7: Boundary conditions used for analysis. | 25 |
| Figure 2.8: Non-feasible structures produced when the angled member length, l , is not long enough to connect the structure..... | 28 |

| | |
|---|----|
| Figure 2.9: Affects of R and d on G_{12}^* ($H=12.7\text{mm}$ $t=0.5\text{mm}$, $N_v=1$)..... | 29 |
| Figure 2.10: Affects of R and d on G_{12}^* ($H=12.7\text{mm}$ $t=0.5\text{mm}$, $N_v=2$)..... | 30 |
| Figure 2.11: Effects of R and d on $(\gamma_{12}^*)_{max}$ ($H=12.7\text{mm}$ $t=0.5\text{mm}$, $N_v=1$)..... | 32 |
| Figure 2.12: Effects of R and d on $(\gamma_{12}^*)_{max}$ ($H=12.7\text{mm}$ $t=0.5\text{mm}$, $N_v=2$)..... | 33 |
| Figure 2.13: Affects of h and l on G_{12}^* ($H=12.7\text{mm}$ $t=0.5\text{mm}$, $N_v=1$)..... | 35 |
| Figure 2.14: Affects of h and l on $(\gamma_{12}^*)_{max}$ ($H=12.7\text{mm}$ $t=0.5\text{mm}$, $N_v=1$)..... | 36 |
| Figure 2.15: Illustration of the parameter modifications required to comply with a given design space when h is changed from 4.2 to 7.0mm using the conventional system. | 39 |
| Figure 2.16: Illustration of how modifications to R and d affect the structure..... | 40 |
| Figure 2.17: Angle change required to maintain constant overall height, H , when angled member length, l , is constant, resulting in a change in horizontal separation..... | 42 |
| Figure 2.18: Schematic of the new design method..... | 44 |
| Figure 2.19: Affects of N_h on G_{12}^* when L and R are constant..... | 45 |
| Figure 2.20: Honeycomb design algorithm flow chart..... | 48 |
| Figure 2.21: Honeycomb Algorithm inputs..... | 49 |
| Figure 2.22: Overall honeycomb dimension inputs..... | 49 |
| Figure 2.23: Honeycomb algorithm wall thickness, t , and number of vertical cells, N_v | 51 |
| Figure 2.24: Honeycomb algorithm initial horizontal separation, d_1 | 52 |
| Figure 2.25: Visualization of honeycomb algorithm design step 1. | 53 |
| Figure 2.26: Honeycomb algorithm design step 1: Finding the effective height, R , to produce the desired maximum shear strain, $(\gamma_{12}^*)_{max}$ | 54 |
| Figure 2.27: Visualization of honeycomb design algorithm step 2. | 56 |
| Figure 2.28: Honeycomb algorithm design step 2: Finding the horizontal separation, d_f , to produce the desired effective shear modulus, G_{12}^* | 57 |

| | |
|--|-----|
| Figure 2.29: Linear relationship used to calculate N_{hf} for the desired shear modulus, G_{12}^* . The linear relationship is only true if effective height, R , is constant..... | 58 |
| Figure 2.30: Honeycomb algorithm outputs..... | 59 |
| Figure 2.31: Resulting effective properties for three target design cases..... | 61 |
| Figure 2.32: Resulting effective properties for targets: $G_{12}^*=4.25\text{Mpa}$, $10\% < (\gamma_{12}^*)_{max} < 10.5\%$ | 64 |
| Figure 2.33: Resulting effective properties for targets: $G_{12}^*=10.25\text{Mpa}$, $6\% < (\gamma_{12}^*)_{max} < 6.5\%$ | 66 |
| Figure 2.34: Resulting effective properties for targets: $G_{12}^*=2.25\text{Mpa}$, $15\% < (\gamma_{12}^*)_{max} < 15.5\%$ | 68 |
| Figure 2.35: 10 unit cells of the final structure design sheared at 10%..... | 71 |
| Figure 4.1: Straight Bristle structure shear band (left) and Tapered Bristle shear band (right)..... | 75 |
| Figure 4.2: Two step design process for the tapered bristle shear band..... | 76 |
| Figure 4.3: Tapered bristle structure resulting from the analytical design solution..... | 77 |
| Figure 3.1: a) Shape morphing antennae and b) morphing airfoil leading edge using compliant mechanisms..... | 80 |
| Figure 3.2: Pseudo-rigid-body model with a) a rigid link mechanism and b) the compliant mechanism counterpart..... | 81 |
| Figure 3.3: Ground structure approach with a) a predefined initial structure where the b) individual structure members are optimized to produce the desired results..... | 83 |
| Figure 3.4: Comparison of Iterative and Direct Displacement flow charts for finding unknown stiffness values..... | 86 |
| Figure 3.5: Direct Displacement used to solve spring stiffnesses for springs in series..... | 88 |
| Figure 3.6: Base structure for the morphing skin design method..... | 89 |
| Figure 3.7: Skin morphing through segment rotation..... | 92 |
| Figure 3.8: Principle used in the direct displacement method..... | 93 |
| Figure 3.9: Summary of the direct displacement synthesis method..... | 95 |
| Figure 3.10: Morphing skin design algorithm flow chart..... | 102 |

| | |
|--|-----|
| Figure 3.11: Algorithm flow chart inputs..... | 103 |
| Figure 3.12: Algorithm shape and load inputs..... | 104 |
| Figure 3.13: Geometric features for the truss elements..... | 105 |
| Figure 3.14: Algorithm flow chart development of the skin structures..... | 106 |
| Figure 3.15: Development of structure segments in terms of segment angle..... | 107 |
| Figure 3.16: Algorithm flow chart steps used to quantify the morphing behavior..... | 108 |
| Figure 3.17: Segment angle rotations and truss displacements..... | 109 |
| Figure 3.18: Algorithm inputs and outputs for the initial analysis step..... | 110 |
| Figure 3.19: Abaqus analysis produced from Python script file and the analysis results..... | 111 |
| Figure 3.20: Spring synthesis flow chart..... | 112 |
| Figure 3.21: Geometry used to find the required spring force from the reaction moment data..... | 113 |
| Figure 3.22: Diagram of the process used to account for spring force interactions along the skin structure..... | 114 |
| Figure 3.23: Load path used to determine spring stiffness along the skin..... | 115 |
| Figure 3.24: Free body diagram used to solve for spring thickness..... | 117 |
| Figure 3.25: Algorithm flow chart for checking the accuracy of the design..... | 118 |
| Figure 3.26: Initial and final desired shape with applied load..... | 120 |
| Figure 3.27: Two models synthesized using outward and inverted spring directions..... | 122 |
| Figure 3.28: Synthesized structure and constant spring thickness structure..... | 125 |
| Figure 3.29: Shape morphing profiles designed using direct displacement..... | 126 |
| Figure 4.4: Multiple loading conditions used to generate shape morphing characteristics not possible with a single force load condition..... | 133 |

| | |
|--|-----|
| Figure 4.5: Force and pressure loading conditions used to create uniform pressure profile..... | 135 |
| Figure 4.6: Closed profile morphing airfoil structures..... | 136 |
| Figure 4.7: Actuator integration to produce desired shape change behavior..... | 138 |

CHAPTER ONE: INTRODUCTION

Materials used in engineering design are selected to serve a specific purpose or aspect of a product based on material properties. The mechanical properties influence aspects of the final component design, such as the size and dimensions required to meet functional requirements. When conventional homogeneous materials are used, the properties of the component material are fixed and the component geometry must be designed to meet the functional requirements based on those properties.

Alternatively, the effective properties of cellular materials are dependent both on the fixed material properties of the constituent material and the geometry of the cellular structure. The additional influence of structural geometry differentiates cellular materials from conventional homogeneous materials with a fixed set of properties, allowing for the effective properties to be changed through geometric modification. The ability to customize the effective properties of a material presents new design opportunities in which materials can be designed with specific properties to satisfy component functionality based on multiple requirements. To increase the viability of cellular materials in new produce design, new methods are needed to aid engineers in the design of the structural geometry to achieve the properties desired for a particular application.

Two such methods are presented in this thesis for the design of cellular structures to achieve desired properties. The design methods are developed to address the specific design needs for two real world applications; a low energy loss honeycomb shear band design, and a morphing airfoil design using a cellular skin structure.

1.0 TWEEL™ SHEAR BAND

The Michelin Tweel™ (Figure 1.1) is a non-pneumatic tire concept currently under development at Michelin Americas Research and Development Corporation (MARC). Researchers from the Clemson Engineering Design Applications and Research (CEDAR) Lab at Clemson University have been tasked with the development of high efficiency shear compliant cellular materials to be used in the Tweel™ shear band to reduce rolling resistance. (1; 2; 3; 4; 5; 6; 7; 8)



Figure 1.1: Michelin Tweel™¹

¹ Gizmomag.com, 2010

The Tweel™ design has three major components; a rigid hub to attach the wheel to the vehicle, a shear beam, and deformable spokes connecting the hub to the shear beam (Figure 1.2) (9). The critical component of the Tweel™ design which allows it to function without air pressure is the shear beam which produces distributed contact pressure along the contact patch.

The shear beam, or shear band, is composed of a shear flexible material with two inextensible membranes at the inner and outer surfaces of the shear material. The inextensible membranes restrict tensile deformation at the boundaries of the shear layer so that the shear beam behaves as a Timoshenko beam, where all bending is a result of shearing deformation in the shear layer when deflected (1).

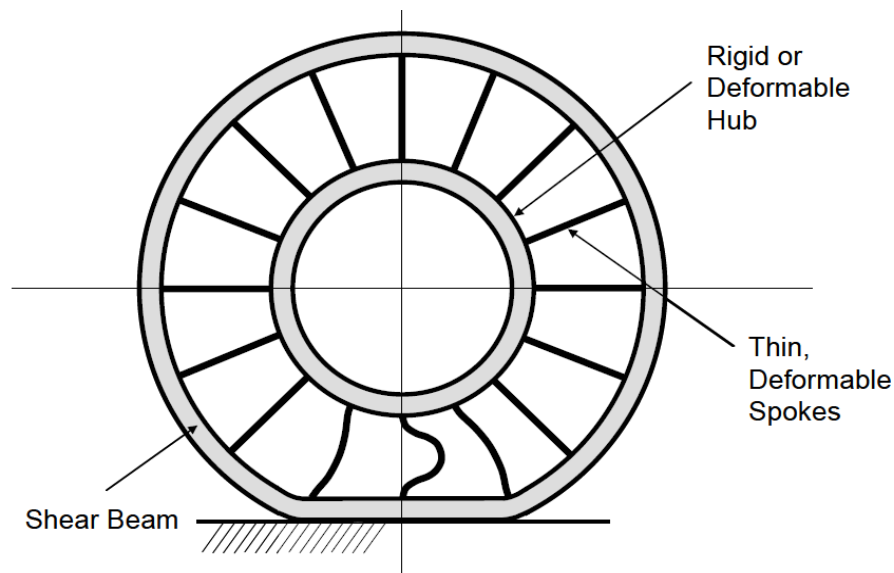


Figure 1.2: Major Tweel™ Components (1)

The deformation characteristics of the Timoshenko produce a distributed contact pressure profile and eliminates pressure spikes at the end of the contact region created by

Euler beams when applied to a flat surface (1). In Figure 1.3 a contact pressure plot is given for a Tweel™ model which shows how the pressure is distributed along the contact patch.

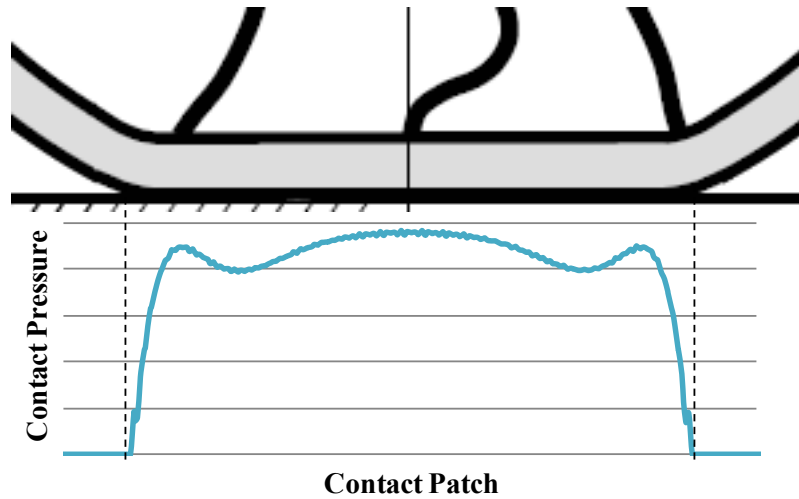


Figure 1.3: Contact Pressure profile of the Tweel™ (2)

The performance of the Tweel™ is dependent on the shear properties of the material used in the shear layer. The shear modulus, G , determines the surface contact pressure and subsequently the length of the contact patch when a given load is applied. The maximum shear strain, $(\gamma_{12})_{max}$, of the shear material does not directly affect the resulting contact pressure characteristics, however, the material must be able to withstand a certain level of shear strain before failure occurs based on the length of the contact patch.

In the current Tweel™ design, polyurethane (PU) is used as the shear material due to its low shear modulus and compliance (Figure 1.4). However, one drawback of PU is that it is an elastomeric material and exhibits high hysteretic energy loss under cyclic loading conditions, resulting in increased rolling resistance. To reduce the amount

of energy loss due to material deformation in the shear band, new materials are desired which can equal the performance characteristics of PU, but will also result in less hysteretic energy loss.

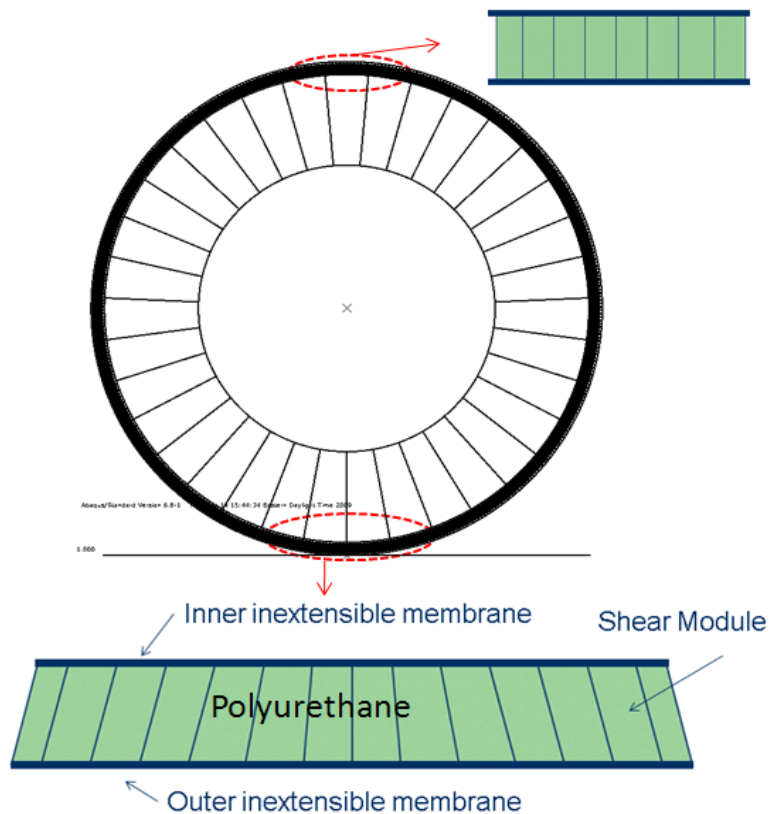


Figure 1.4: Tweel Shear Band (3)

One solution is to develop a shear compliant cellular material to replace PU as shown in Figure 1.5. This approach can reduce the amount of energy loss on the shear material by permitting the use of more efficient constituent materials. Once the material is selected, the geometry of the structure can be designed to produce the necessary effective shear properties.

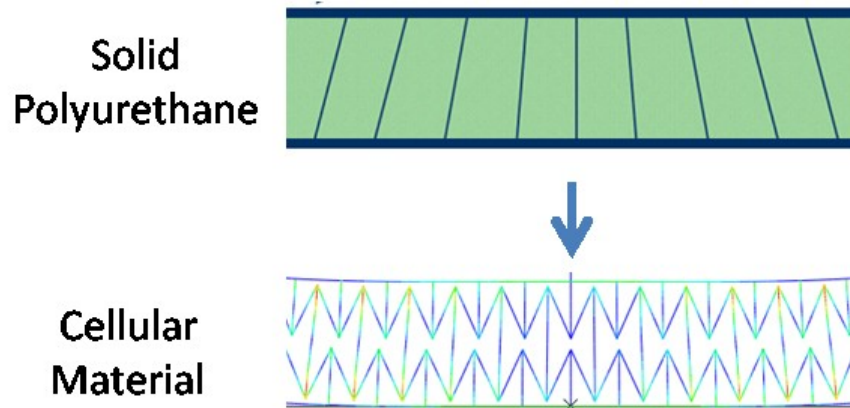


Figure 1.5: Replace homogeneous material with cellular material to reduce hysteretic energy loss. (3)

1.0.1 Cellular Structure Design Concepts

To recreate the performance characteristics of the PU shear band, the new cellular shear band material must have an effective shear modulus, G_{12}^* , of 4.25MPa and a maximum shear strain, $(\gamma_{12}^*)_{max}$, of at least 10% with a shear layer height of 12.7mm (1/2 inch)². Although the cellular structure used in the shear band must form a circular shape, for design purposes it is assumed that the structure is flat with an overall length of 250mm. The shear band material property requirements are given in Table 1.1 and in Figure 1.6.

² Note that actual Tweel™ design values are not used for proprietary reasons.

Table 1.1: Shear band material property requirements.

| | |
|--------------------------------|-----------------------------------|
| Effective Shear Stiffness | $G_{12}^* = 4.25\text{MPa}$ |
| Maximum Effective Shear Strain | $(\gamma_{12}^*)_{max} \geq 10\%$ |
| Overall Height | $H = 12.7\text{mm}$ |
| Overall Length | $L = 250\text{mm}$ |

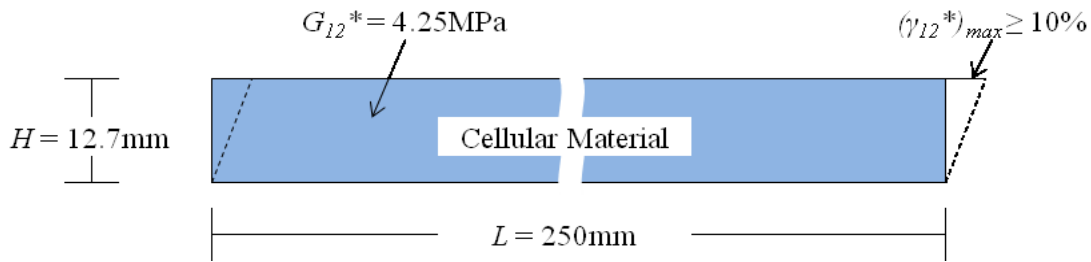


Figure 1.6: Shear band material property requirements.

The research conducted at the CEDAR lab has sought to develop a cellular structure which will produce the target effective shear properties. One of the objectives of this work is to develop a cellular geometry which can facilitate high shear modulus and high compliance simultaneously. Achieving the two target properties, G_{12}^* and $(\gamma_{12}^*)_{max}$, needed for the Tweel™ is made difficult due to the inverse relationship between the two target properties. Generally, as the shear modulus of a cellular structure increases, the amount of shear strain permitted before the stresses in the material reach the yielding point is decreased. Two of the approaches taken to find a cellular structure which is suitable for the current application are topology optimization and auxetic cellular design.

1.0.2 Topology Optimization

Topology optimization is used here to design a structure topology which will maximize the shear modulus and shear compliance. Several candidate solutions were produced using this method; however, due to issues inherent in topology optimization, such as the development of point flexures (Figure 1.7), the structures resulted in high stress concentrations and did not meet the requirements for the material.



Figure 1.7: Topology Optimization Solutions. (4)

Auxetic cellular structures are also considered as a solution. The chiral and auxetic honeycomb structures shown in Figure 1.8 which exhibit auxetic behavior (negative Poisson's ratio) have been shown to be highly shear compliant (5; 6). These structures are studied to determine if the target effective shear properties can be achieved by designing the geometric parameters.

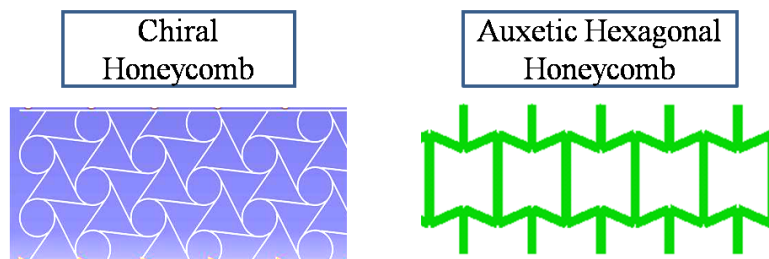


Figure 1.8: Chiral (7) and Auxetic honeycombs having negative Poisson's ratio.

Chapter Two: of this thesis details a portion of the work dedicated to the design of honeycomb structures to achieve the target effective shear properties. A method is developed to design the geometric parameters of a honeycomb structure to achieve the two desired effective properties, G_{12}^* and $(\gamma_{12}^*)_{max}$, simultaneously. The objective of the design method is to create a systematic process which can be automated to design structures for a specific application quickly and effectively.

1.1 SHAPE MORPHING AIRFOILS

In recent years, much research has been devoted to the development of shape morphing airfoil technologies to replace traditional fixed aircraft wings. The objective of this work is to create new airfoils which are able to change shape to perform more efficiently over a variety of flight conditions. (8)

The performance of a specific airfoil geometry is highly dependent on the speed and weight conditions of the aircraft (9; 10). For fixed wing aircraft, the airfoil geometry must be designed to perform optimally for a single set of conditions(10), and for all other conditions the performance decreases (8). The development of morphing airfoil designs can significantly improve aircraft performance by continually changing the airfoil profile to the optimum geometry for multiple flight conditions(10). The benefits of a morphing airfoil can be seen in Figure 1.9 where a variable camber morphing airfoil is shown. The morphing airfoil in Figure 1.9 can achieve high flight for low speeds using the initial profile, and achieve high performance at high speeds by deforming to the morphed profile.

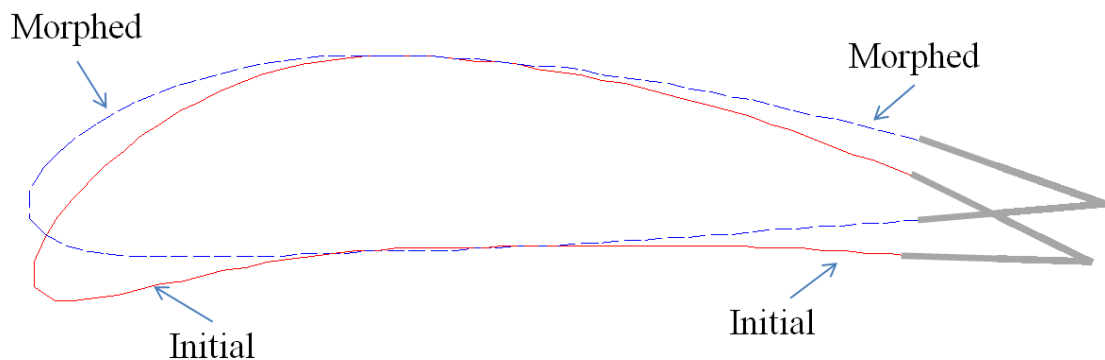


Figure 1.9: Variable camber morphing airfoil designed to change shape from the initial profile to the morphed profile.

Several approaches have been used in the development of a viable morphing airfoil concept. Spadoni et al (5) have investigated the use of shear compliant chiral cellular structures embedded within airfoils to allow for passive camber deformation (Figure 1.10a). Their research has shown that the stiffness of the structure can be tailored to produce different deflections by altering the parameters of the chiral core. The use of chiral cores motivated a brief investigation of a shear compliant honeycomb core airfoil at CEDAR (Figure 1.10b). However, this concept was not developed further due to limited capabilities in terms of controlling the overall shape morphing characteristics of the airfoil using shear compliance alone. That is, it is possible to control the magnitude of the shape change but not to control additional characteristics of the shape morphing behavior.

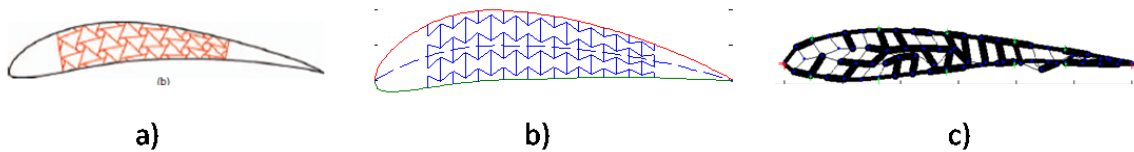


Figure 1.10: a) Chiral core airfoil (5), b) Honeycomb core airfoil (11), c) Internal compliant mechanism airfoil (9).

Other researchers have focused on compliant mechanism synthesis using Such methods as genetic algorithms to produce structures which deform from an initial desired shape to a final desired shape as shown in Figure 1.10c (12; 13; 14; 15; 9). Many of these solutions have yielded airfoil structures with desired morphing characteristics using aerodynamic forces (9) or actuator forces (14; 15) to cause deformation.

The majority of research on morphing airfoil technology has focused on the synthesis of internal compliant mechanisms which facilitate the morphing behavior, but few have considered the design of the skin material used to separate the internal structures and the fluid flow (8).

A smooth skin able to deform continuously while transferring loads is critical for the success of any morphing airfoil concept (8). Research on morphing airfoil skins attached to internal compliant structures has shown that the skin material should have low membrane stiffness to allow for stretching and compression and high lateral stiffness to prevent bending as a result of normal aerodynamic forces (8; 16; 10). Several concepts have been developed for such a material. Ramrakhyani et al (10) have suggested segmented skins similar to fish scales, where rigid members prevent bending due to aerodynamic loads and overlapping joints provide low membrane stiffness (Figure 1.11a). One disadvantage of this concept is that the overlapping segments result in

discontinuities in the surface, affecting the aerodynamics of the airfoil (8). Corrugated materials have also been suggested as an intermediate structure connecting the internal compliant mechanism to a flexible skin (10; 17). The corrugated structures have low membrane stiffness and provide out-of-plane stiffness to the skin (Figure 1.11b). However, they do not provide high in-plane bending stiffness needed to support aerodynamic loads for airfoil profile morphing (8).

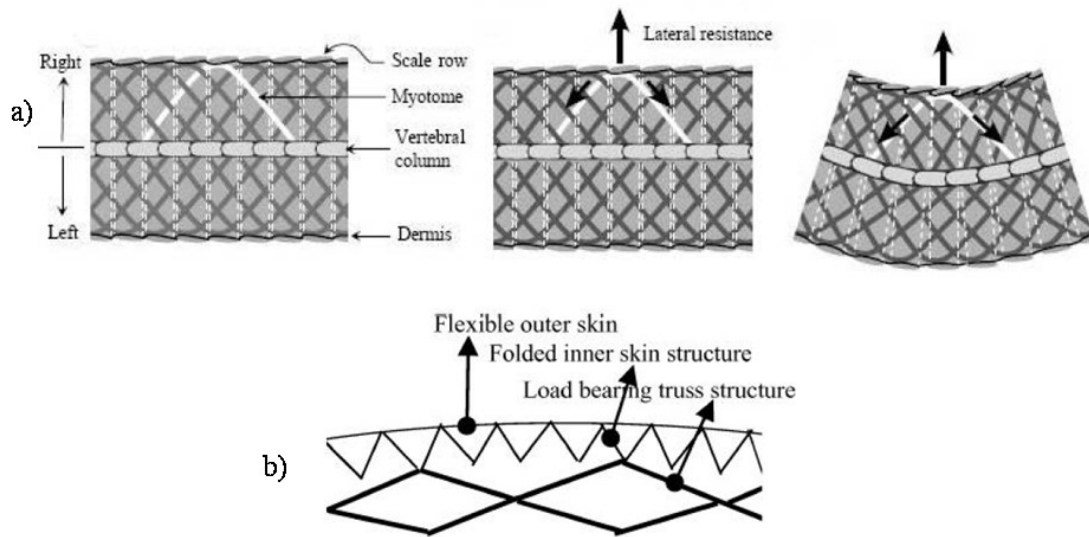


Figure 1.11: Morphing airfoil skin design concepts; a) segmented scale design (8) and b) corrugated structure with flexible skin (10) design.

The morphing skin concepts discussed in the previous paragraph are designed to serve two functions; 1) to provide a smooth and continuous aerodynamic surface, and 2) to transfer loads between the internal compliant structure and the external aerodynamic forces. The skins are designed to be passive elements in the morphing airfoil structure. That is, the skin deformation is dependent on the internal compliant structure and the

aerodynamic forces, and the skin itself is not designed to actively influence the morphing characteristics of the airfoil.

Chapter Three of this thesis introduces a new morphing skin design concept which intends to expand the functionality of morphing skins by making them active components in the morphing airfoil design. This is done by designing the skin itself to have desired morphing characteristics which do not depend entirely on an internal compliant structure. The objective of the morphing skin design concept developed in this thesis is to design a cellular skin structure to achieve desired morphing behavior by varying the stiffness properties along the skin surface. Moreover, this provides the second approach to the design of cellular materials that operate effectively beyond the constitutive material properties.

1.2 SUMMARY

The Michelin Tweel™ and the morphing airfoil are two examples of how customizable cellular materials can be used to improve existing designs and achieve performance characteristics not possible using homogeneous materials. However, the use of cellular materials adds complexity to the design process due to the dependence on geometry to achieve the properties desired for a particular application. The objective of this thesis is to begin to develop new methods that can be used to simplify the design of cellular structures for specific applications, ultimately making cellular materials more viable in new designs. The methods developed in this thesis serve as two examples of how new cellular structure design methods can improve the design process for two separate applications.

CHAPTER TWO: SHEAR COMPLIANT HONEYCOMB STRUCTURE SYNTHESIS

In ongoing research in the Clemson Engineering Design Application and Research Lab (CEDAR), new materials are sought which are able to mimic elastomeric shear properties yet are composed of low dampening materials to reduce energy loss under cyclic loading conditions (6; 3; 4; 2; 18). A previous study on a design of shear flexure with honeycombs shows that cellular solids having negative Poisson's ratio, called auxetic, have high shear flexibility (6).

Since the early work on the honeycomb mechanics by Gibson and Ashby (19), many analytical and numerical models have been developed to describe in-plane effective properties of honeycomb structures; for example, a refined cell wall bending model using beam stretching and hinging motion (20), an energy method model (21), a refined model with round shape at cell edges (22), and a model using the homogenization method (23). In-plane mechanical properties with different cell types (square, hexagonal, triangle, mixed squares and triangles, and diamond) were investigated by Wang and McDowell (24). Hexagonal and chiral shapes of honeycombs have also been studied for a functional design (25; 26; 27). A multifunctional approach requiring structural stability and fast heat transfer was investigated with honeycomb structures (28).

The practical applications of cellular structure design have been limited to the development of stiff and ultra-light sandwich cores for aircraft and aerospace structures, which are related to the honeycombs' out of plane properties (29; 30; 31; 32; 33), and rigidified inflatable structures for housing (34). Recently, honeycombs' in-plane

flexibility began to be designed in aerospace morphing technology (35; 36). However, only limited application based studies on design with honeycomb structures are available; one example is in the multifunctional design of components combining structural and thermal properties in the application of gas turbine engines (37). Huang and Gibson studied on the design of honeycombs for beam and plate structures (38).

Shear compliant hexagonal honeycomb materials are considered here to replace conventional materials such as polyurethane (PU) due to their lower densities, higher efficiencies under cyclic loading conditions, and their ability to be designed with specific mechanical properties. To be successful, the cellular material must have effective shear properties similar to those of elastomeric materials while reducing the affects of hysteretic energy loss. The material must have an effective shear modulus of between 4 and 4.5MPa and must be able to withstand shear strains up to 10% before yielding occurs in the material. Additionally, the material needs to have an overall height of 12.7mm and a length of 250mm (See Table 1.1).

This chapter introduces a method for the design of honeycomb cellular structures to achieve both target effective properties simultaneously. In the design of honeycomb structures, the conventional geometric parameters shown in Figure 2.1 (cell height, h , cell length, l , and cell angle, θ) have been used to find effective properties of honeycomb structures (19). However, the use of these parameters can be difficult when designing two target properties for a fixed design space based on previous work on this topic. These difficulties are due to the dependency of the overall dimensions, H and L , on the geometric parameters, h , l , and θ . That is, when a single geometric parameter is changed,

the overall dimensions of the structure change unless other geometric parameters are modified to comply with the fixed design space.

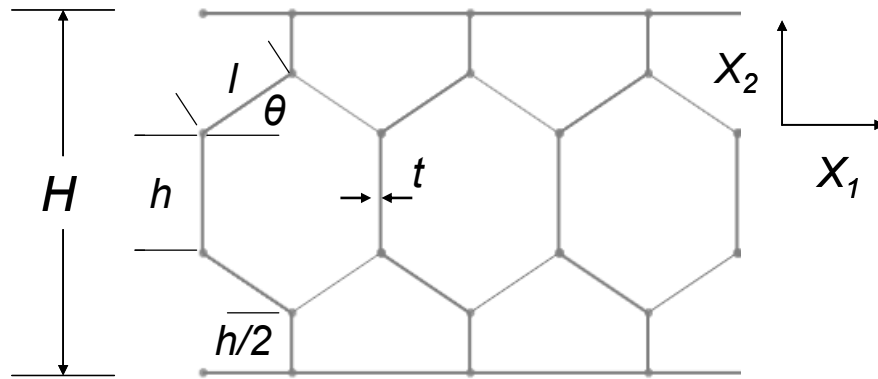


Figure 2.1: Conventional parameters for a two-dimensional honeycomb structure

This aspect of the conventional system of honeycomb parameters makes it difficult to control the geometry of the structure during the design process because the combination of parameter values must be selected to produce the fixed overall dimensions. For this reason, a new system is desired which will make the geometric parameters dependent on the overall dimensions.

A new system for describing honeycomb structures is introduced in which the geometry of the structure is dependent on the overall dimensions, H and L . In this system (Figure 2.2), conventional parameters are replaced by two new parameters, R and d ; where R describes the effective height of the vertical honeycomb members in one horizontal unit cell relative to the overall height of the structure, and d is the horizontal separation between honeycomb cells. These new parameters relate the honeycomb geometry to the overall dimensions of the design space, allowing for the design space to

be easily fixed. They are also independent of each other so that R or d can be freely modified without affecting the other.

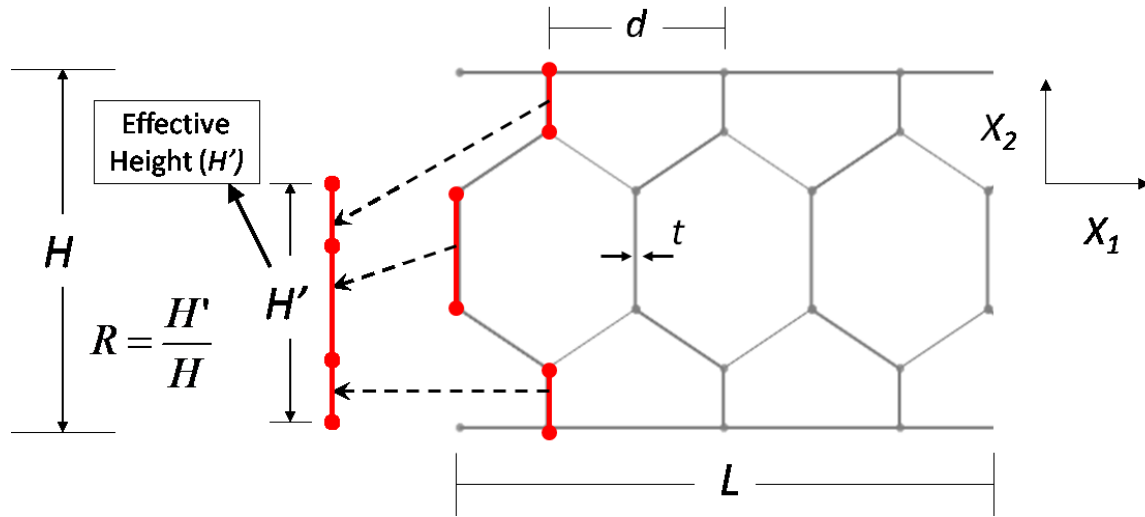


Figure 2.2: Honeycomb structure using the new system of parameters for $N_v=1$ and $N_h=3$.

The independent honeycomb features, R and d , are investigated to determine the affects each has on the target effective shear properties. Based on these findings, a new method for honeycomb structure design is developed which takes advantage of independent honeycomb features to design for the two effective properties simultaneously.

2.0 HONEYCOMB STRUCTURE ANALYSIS

Honeycomb cellular materials are formed to produce a regular pattern of hexagonal cells. The cells are oriented so that two of the hexagonal edges are parallel to the X_2 direction and the structures attach to the upper and lower membrane boundaries running parallel to the X_1 direction (Figure 2.1).

The analysis of honeycomb materials is performed by considering the structures to be a system of interconnected beam members with thickness t , where the vertical members have a length h , and the angled members have a length of l as shown in Figure 2.1. During analysis, the honeycomb members are modeled as 2D beam elements which experience bending deformation when in-plane shear loads are applied. The effective properties are derived by determining the resulting deflection of the beam system when a load is applied. By studying how dimensional modifications to the structures affect the resulting effective properties, it is possible to design the structures so that the resulting effective properties reach a target value.

2.0.1 New Parameter Development

The conventional honeycomb parameters (h , l , and θ) two disadvantages when used for the current design application. First, the parameters are not dependent on the overall dimensions of the material, H and L . Thus, if a single parameter is changed then overall dimensions will change. Second, all geometric parameters are coupled so that all parameters must be altered to comply with a fixed design space, making it difficult to control the geometry during the design process. A new system of parameterization is developed to address these challenges.

When a honeycomb structure is subjected to a shear load, the primary mode of deformation is from bending in the vertical members, as shown in Figure 2.3. As such, the new system of parameters is formed under assumption that the features of the highly deformed vertical members will have the most significant influence on the resulting shear

properties. The new system of parameters captures certain attributes of the vertical members relative to the structure as a whole. In effect, the objective of the new parameter system is to first identify the features of the structural geometry which have the greatest effect on G_{12}^* and $(\gamma_{12}^*)_{max}$, and then develop a system where the separate features can be controlled independently to achieve both target properties efficiently.

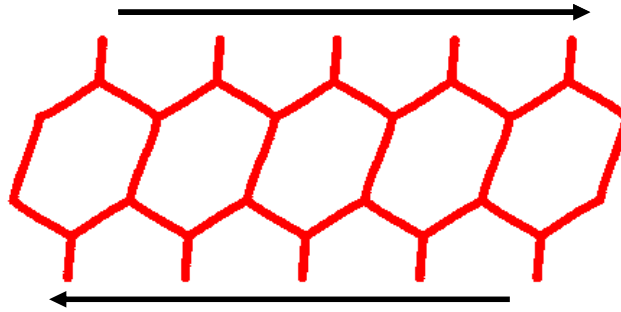


Figure 2.3: Honeycomb structure reaction to shear loading

In the new system (Figure 2.2), honeycomb structures are viewed as a series of vertical beam members located within the shear layer which are interconnected by relatively rigid angled members to form the honeycomb pattern. In this simplified view of honeycomb structures, the deformed vertical members in the structure are analogous to a parallel spring system, where the vertical members in each horizontal unit cell act as an effective spring element. The parallel spring analogy serves as the basis for the development of the honeycomb design method, where the parameters R and d describe the features of the vertical spring members which affect the stiffness and compliance of the spring system.

From this perspective, two generalizations are made about the resulting effective properties, G_{12}^* and $(\gamma_{12}^*)_{max}$. First, there are two features of the structure which affect

G_{12}^* , the stiffness of the deformed vertical members, and the horizontal density of the vertical members. Second, only one feature significantly influences $(\gamma_{12}^*)_{max}$, the compliance of the vertical members.

For a constant wall thickness, t , an increase in vertical members length will result in a decrease in the member stiffness, decreasing G_{12}^* , and an increase in the member compliance, increasing $(\gamma_{12}^*)_{max}$. In the new system of parameters the lengths of the vertical members are described using the effective height, R , which is a ratio of the sum of the vertical member lengths in one horizontal cell, H' , and overall height, H , as shown in Figure 2.2 and Figure 2.4.

Equation 2.1:
$$R = \frac{H'}{H}$$

R is a unitless variable and independent of the number of vertical layers, N_v , so as N_v increases, the individual heights of the vertical members will decrease, but the combined length will remain constant. This is illustrated in Figure 2.4, where two structures are shown with equal overall height H , equal effective height, R , but different number of vertical cells. The structure with two vertical cells has more vertical members running from the bottom to the top of the structure, but the total length of the vertical members for one horizontal cell is equal to that of the single vertical cell structure.

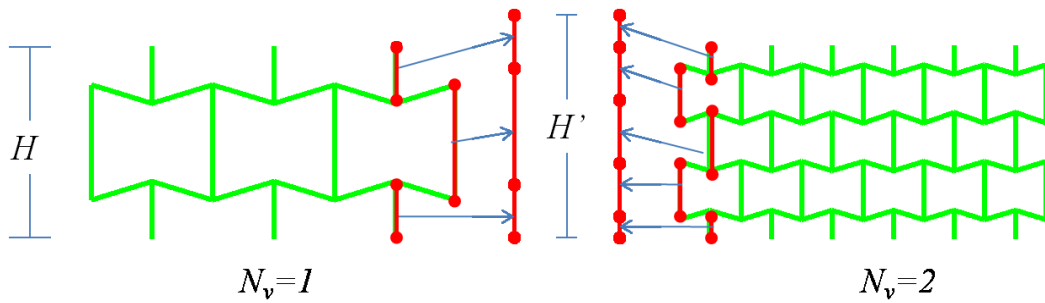


Figure 2.4: Two structures having equal effective heights, R , and a different number of vertical cells, N_v .

Additionally, R is limited to $0 < R < 2$ to prevent zero vertical member lengths and cell overlap. As illustrated in Figure 2.5, when R is at the limits of the specified range the resulting cells either have no vertical members at $R=0$, or the cell wall members come into contact at $R=2$. Outside the specified range, the honeycomb cells are not possible due to cell wall overlap, as shown at $R = -.4$ and $R = 2.4$.

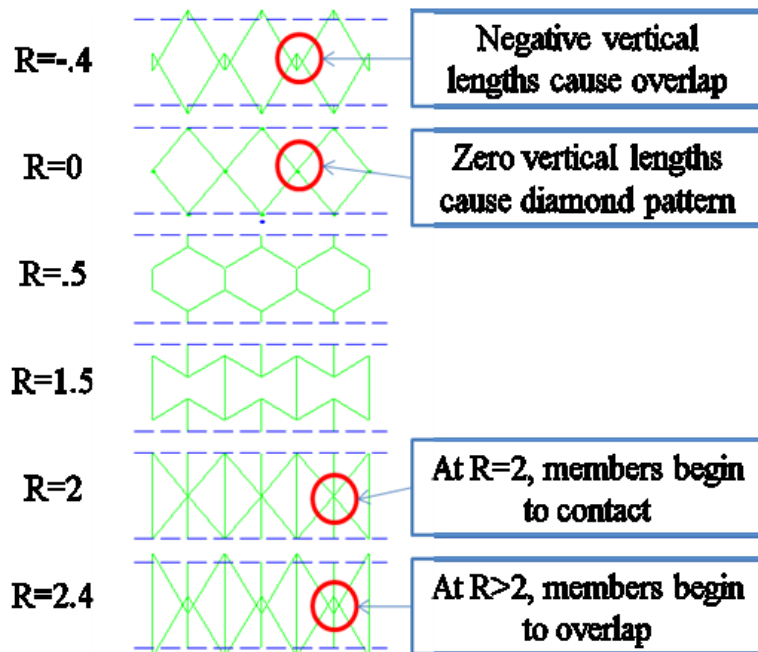


Figure 2.5: Outside the range of $0 < R < 2$, the cell wall members begin to overlap.

In the generalized view of honeycomb structures, with a constant wall thickness, t , and constant vertical member length, an increase in the horizontal density will require more horizontal cells, N_h , to be deformed over a given length of the material. The increase in the number of deformed members should result in an increase of G_{12}^* . That is, as the distance between the horizontal cells decreases, more vertical members must be deformed and the structure will become more stiff. The horizontal density of the vertical members is determined in the new system by the horizontal separation, d , of the horizontal cells.

Equation 2.2:
$$d = \frac{L}{N_h}$$

As the new parameters are independent of each other but dependent on the overall design space dimensions, R and d can be modified independently without affecting each other or the overall dimensions. The values of R and d can be calculated for a known structure described by the conventional parameters using Equation 2.3 and Equation 2.4, and the conversion equations to go from one system to the other are given in Table 2.1.

Equation 2.3:
$$R = \frac{2hN_v}{H}$$

Equation 2.4:
$$d = 2l\cos\theta$$

Table 2.1: Conversion equations relating the conventional parameters and the new parameters.

| Conventional to New | New to Conventional |
|------------------------------|--|
| Known: h, l, θ, N_v | Known: R, d, H, N_v |
| $H = N_v(2h + 2l\sin\theta)$ | $h = \frac{RH}{2N_v}$ |
| $R = \frac{2hN_v}{H}$ | $\theta = \tan^{-1}\left(\frac{H(1-R)}{dN_v}\right)$ |
| $d = 2l\cos\theta$ | $l = \frac{d}{2\cos\theta}$ |

2.0.2 New Parameter Analysis

Parametric studies are performed on the new parameters to determine their effects on G_{12}^* and $(\gamma_{12}^*)_{max}$. The studies were performed using a program developed in Matlab 7.6.0 which works in concert with Abaqus CAE version 6.8-1 and is executed using an Intel Quad Core CPU operating at 2.4GHz and 3.25GB RAM. The honeycomb structures are generated and modified in Matlab, while Abaqus is used for analysis. The material used in the analysis is polycarbonate with a modulus of elasticity of 2.7GPa, flexural yield stress of 80MPa (39), and a Poisson's ratio of 0.42.

For each analysis step, the structures are subjected to simple shear and the desired results are the shear modulus, G_{12}^* , and the maximum allowable shear strain, $(\gamma_{12}^*)_{max}$. The structures are modeled using quadratic beam elements which are able to model transverse shear affects, and the material is modeled as linear elastic. In each analysis, a

single static analysis step is performed on a honeycomb structure having sixteen horizontal cells as shown in Figure 2.6.

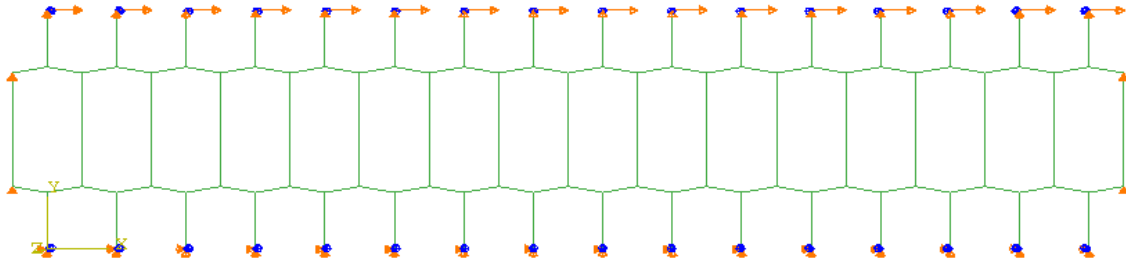


Figure 2.6: Typical structure analyzed in the parametric studies having 16 horizontal honeycomb cells

To simulate simple shear, the boundary conditions shown in Figure 2.7 are applied. The bottom members are fully constrained at the base and the free ends of the top members are subjected to a displacement, δ , in the X_1 direction to produce a 0.1% shear strain. The free ends of the members at the top and bottom membrane locations are constrained to allow for no rotation or X_2 displacement. The rotation constraints simulate rigid connections at the locations where the honeycomb structure attaches to the membranes. One additional constraint is applied to the end members on both the right and left hand side of the structure to prevent displacement in the X_2 direction. The purpose of these constraints is to attempt to reduce end effects in the analysis by ensuring that the end vertical members do not displace more than the vertical members in the middle of the structure.

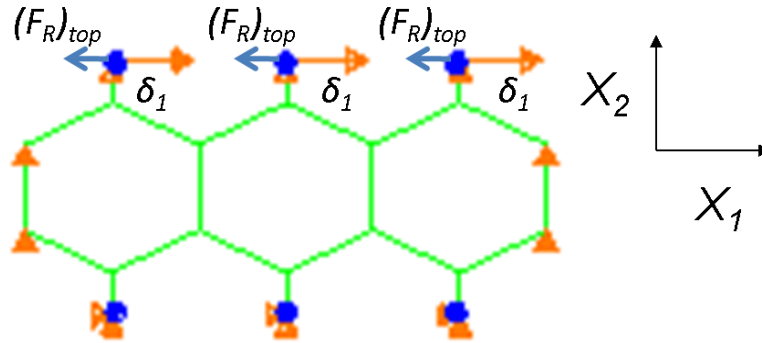


Figure 2.7: Boundary conditions used for analysis.

The shear modulus, G_{12}^* , is calculated using the reaction force method. The sum of the reaction forces, $(F_R)_{top}$, at the locations of the displacement boundary conditions, δ_1 , are used with the top surface area to find the effective shear stress, τ^* . In Equation 2.5, the top surface area is the total length of the structure, L , by the out-of-plane depth of the structure, b , where b is assumed to be one. The effective shear strain, γ^* , is found using the known displacement of the top members and the overall height, H , using Equation 2.6. The resulting effective modulus, G_{12}^* , is then found using Equation 2.7.

Equation 2.5:
$$\tau^* = \frac{\Sigma(F_R)_{top}}{bL}$$

Equation 2.6:
$$\gamma^* = \frac{\delta}{H}$$

Equation 2.7:
$$G^* = \frac{\tau^*}{\gamma^*}$$

The maximum allowable shear strain is calculated using Von Mises stress results. In the elastic range of the material, the linear stress strain relationship is used to calculate $(\gamma_{12}^*)_{max}$ using Equation 2.8,

Equation 2.8:
$$(\gamma_{12}^*)_{max} = \frac{\sigma_y \gamma_{12}^*}{(\sigma_{vm})_{max}}$$

Where γ_{12}^* is the effective shear strain used in the analysis, σ_y is the yield strength of a material, and $(\sigma_{vm})_{max}$ is the maximum Von Mises stress found in the finite element analysis.

The parametric studies for R and d are performed for both the one and two vertical cell configurations. For each configuration, the unitless variable R is varied from 0.4 to 1.75 in increments of 0.15, and d is varied from 4mm to 10mm in increments of 3mm. A summary of the structures used in the parametric study is provided in Table 2.2. The multiple values for d and N_v used for each R value are indicated in Table 2.2. The parametric study will produce the effective properties for each combination of R , d , and N_v values.

Table 2.2: Structure geometries used in parametric studies for new parameters, R and d

| t (mm) | N_v | R | d (mm) |
|----------|-------|------|----------|
| 0.5 | 1, 2 | 0.4 | 4, 7, 10 |
| 0.5 | 1, 2 | 0.55 | 4, 7, 10 |
| 0.5 | 1, 2 | 0.7 | 4, 7, 10 |
| 0.5 | 1, 2 | 0.85 | 4, 7, 10 |
| 0.5 | 1, 2 | 1 | 4, 7, 10 |
| 0.5 | 1, 2 | 1.15 | 4, 7, 10 |
| 0.5 | 1, 2 | 1.3 | 4, 7, 10 |
| 0.5 | 1, 2 | 1.45 | 4, 7, 10 |
| 0.5 | 1, 2 | 1.6 | 4, 7, 10 |
| 0.5 | 1, 2 | 1.75 | 4, 7, 10 |

The parametric studies for the conventional system of parameters, h , l , and θ , were performed for only the single vertical cell configuration. The value of h is varied

from 4.0mm to 11.5mm with l values of 3mm, 4.5mm, and 7mm. Table 2.3 shows the structure geometries used in the conventional parameter studies.

Table 2.3: Structure geometries used in parametric studies for conventional parameters, h and l

| h (mm) | θ (degrees) | l (mm) |
|----------|--------------------|-----------|
| 4 | 23.06 | 3, 4.5, 6 |
| 4.5 | 17.96 | 3, 4.5, 6 |
| 5 | 13.00 | 3, 4.5, 6 |
| 5.5 | 8.14 | 3, 4.5, 6 |
| 6 | 3.34 | 3, 4.5, 6 |
| 6.5 | -1.43 | 3, 4.5, 6 |
| 7 | -6.22 | 3, 4.5, 6 |
| 7.5 | -11.05 | 3, 4.5, 6 |
| 8 | -15.96 | 3, 4.5, 6 |
| 8.5 | -21.00 | 4.5, 6 |
| 9 | -26.21 | 4.5, 6 |
| 9.5 | -31.67 | 4.5, 6 |
| 10 | -37.47 | 4.5, 6 |
| 10.5 | -43.76 | 6 |
| 11 | -50.81 | 6 |
| 11.5 | -59.13 | 6 |

The use of fixed angled member length, l , in the conventional study limits the number of possible structures as h increases. In Table 2.3, for values of h greater than 8mm, the structure is not possible using $l=3$ mm because the angled members are not long enough to connect the vertical members as shown in Figure 2.8. The same is true when $l=4.5$ mm and h is greater than 10mm.

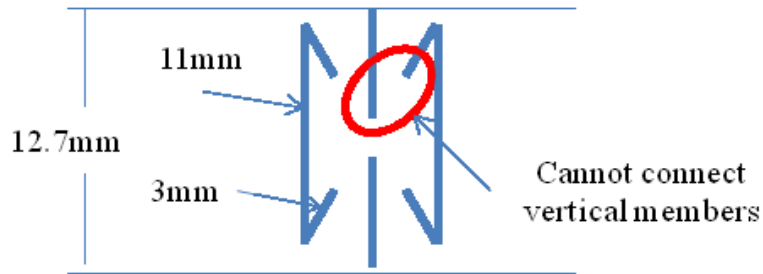


Figure 2.8: Non-feasible structures produced when the angled member length, l , is not long enough to connect the structure.

2.1 PARAMETRIC STUDIES

Parametric studies are conducted to explore the effective shear modulus and maximum effective shear strain with respect to the conventional approach. These studies are presented here.

2.1.1 Effective Shear Modulus

The study results show that an increase in effective height, R , results in a decrease of G_{12}^* . Furthermore, an increase in horizontal separation, d , results in a decrease in G_{12}^* . As R increases from 0.4 to 1.8, the increasing lengths of the deformed vertical members cause them to become less stiff, resulting in a decrease to G_{12}^* . This is illustrated in Figure 2.9, where the structures having the shortest vertical member lengths, at $R=0.4$, result in the highest modulus, and the structures with the longest vertical member lengths, at $R=1.75$, result in the lowest modulus. When d is increased from 4 to 10mm, the horizontal density of the deformed vertical members decreases and fewer members must be deformed over a given length, resulting in a decrease in G_{12}^* . The results are shown for one vertical cell configuration in Figure 2.9 and for two vertical cell configuration in Figure 2.10.

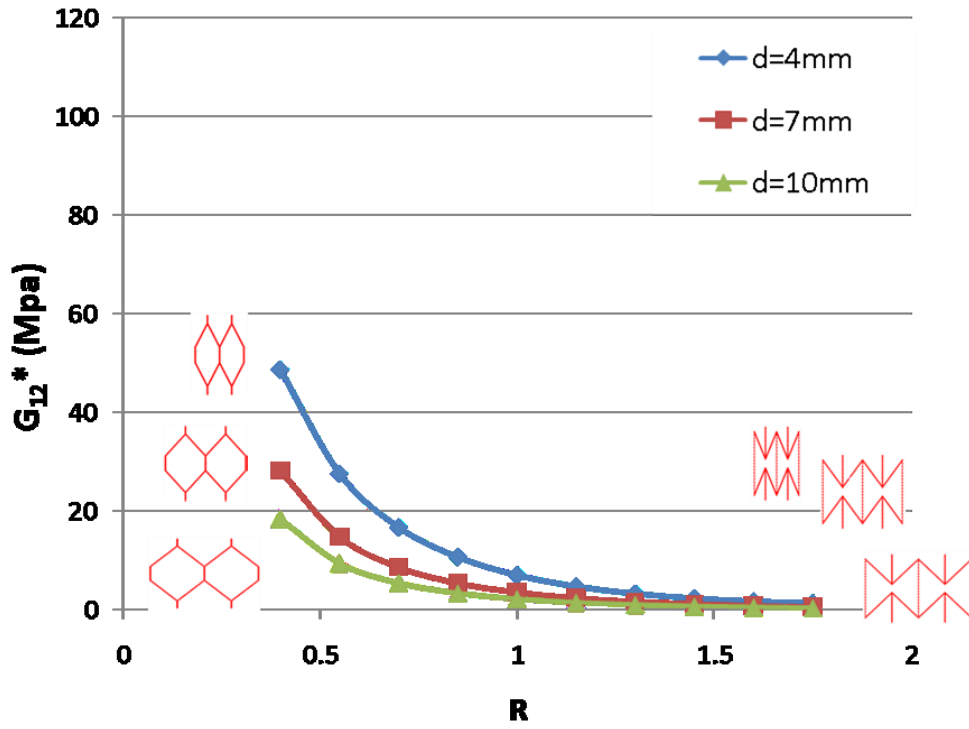


Figure 2.9: Affects of R and d on G_{12}^* ($H=12.7\text{mm}$ $t=0.5\text{mm}$, $N_v=1$).

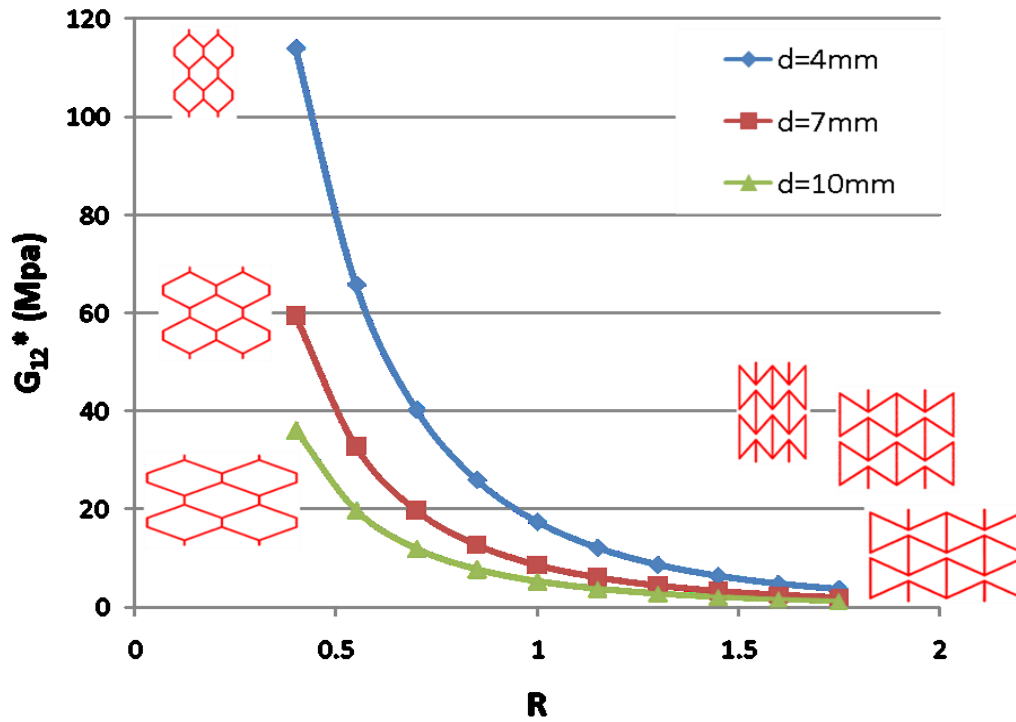


Figure 2.10: Affects of R and d on G_{12}^* ($H=12.7\text{mm}$ $t=0.5\text{mm}$, $N_v=2$).

The number of vertical cell layers, N_v , also influences G_{12}^* . The same values for R and d were used in Figure 2.9 and Figure 2.10, however G_{12}^* is significantly greater in Figure 2.10 when $N_v=2$. Although the effective heights of the vertical members are equal, when N_v is increased the effective vertical member length is more constrained, causing the structure to become more stiff.

The resulting effective shear properties from the new parameter studies are listed in Table 2.4 and Table 2.5.

Table 2.4: Parametric study data for the new parameters with one vertical cell

| $t = 1.5mm, N_v = 1$ | | $G_{12}^* (Mpa)$ | | | $(\gamma_{12}^*)_{max} (\%)$ | | |
|----------------------|----------|------------------|--------------|--------------|------------------------------|--------------|--------------|
| R | $d (mm)$ | $d = 4mm$ | $d = 7mm$ | $d = 10mm$ | $d = 4mm$ | $d = 7mm$ | $d = 10mm$ |
| 0.4 | 4, 7, 10 | 48.57 | 28.24 | 18.33 | 2.99 | 2.94 | 3.16 |
| 0.55 | 4, 7, 10 | 27.52 | 14.85 | 9.43 | 3.87 | 4.09 | 4.50 |
| 0.7 | 4, 7, 10 | 16.66 | 8.68 | 5.46 | 5.07 | 5.53 | 6.13 |
| 0.85 | 4, 7, 10 | 10.62 | 5.45 | 3.43 | 6.62 | 7.31 | 8.09 |
| 1 | 4, 7, 10 | 6.98 | 3.58 | 2.27 | 8.65 | 9.52 | 10.45 |
| 1.15 | 4, 7, 10 | 4.68 | 2.44 | 1.56 | 11.21 | 12.16 | 13.21 |
| 1.3 | 4, 7, 10 | 3.22 | 1.71 | 1.11 | 14.36 | 15.31 | 16.42 |
| 1.45 | 4, 7, 10 | 2.28 | 1.24 | 0.81 | 18.10 | 19.00 | 20.14 |
| 1.6 | 4, 7, 10 | 1.67 | 0.91 | 0.61 | 22.39 | 23.24 | 24.37 |
| 1.75 | 4, 7, 10 | 1.25 | 0.69 | 0.47 | 27.20 | 28.00 | 29.11 |

Table 2.5: Parametric study data for the new parameters with two vertical cells

| $t = 0.5mm, N_v = 2$ | | $G_{12}^* (Mpa)$ | | | $(\gamma_{12}^*)_{max} (\%)$ | | |
|----------------------|----------|------------------|--------------|--------------|------------------------------|--------------|--------------|
| R | $d (mm)$ | $d = 4mm$ | $d = 7mm$ | $d = 10mm$ | $d = 4mm$ | $d = 7mm$ | $d = 10mm$ |
| 0.4 | 4, 7, 10 | 113.90 | 59.47 | 36.14 | 2.29 | 2.49 | 2.85 |
| 0.55 | 4, 7, 10 | 65.71 | 32.75 | 19.72 | 2.94 | 3.33 | 3.84 |
| 0.7 | 4, 7, 10 | 40.21 | 19.71 | 11.87 | 3.80 | 4.42 | 5.08 |
| 0.85 | 4, 7, 10 | 25.91 | 12.67 | 7.67 | 4.94 | 5.73 | 6.55 |
| 1 | 4, 7, 10 | 17.41 | 8.57 | 5.23 | 6.37 | 7.29 | 8.25 |
| 1.15 | 4, 7, 10 | 12.08 | 6.02 | 3.72 | 8.02 | 9.13 | 10.22 |
| 1.3 | 4, 7, 10 | 8.63 | 4.37 | 2.72 | 9.91 | 11.12 | 12.46 |
| 1.45 | 4, 7, 10 | 6.32 | 3.25 | 2.05 | 12.04 | 13.32 | 14.80 |
| 1.6 | 4, 7, 10 | 4.74 | 2.48 | 1.58 | 14.45 | 15.77 | 17.34 |
| 1.75 | 4, 7, 10 | 3.63 | 1.92 | 1.24 | 17.15 | 18.48 | 20.12 |

2.1.2 Maximum Effective Shear Strain

The test results show that the maximum effective shear strain, $(\gamma_{12}^*)_{max}$, increases as R is increased. This again is attributed to the increased length of the deformed vertical members within the structure. As R increases, the vertical lengths increase and are able to permit larger deflections before yielding occurs. The results are provided in Figure 2.11 for the one vertical cell configuration and in Figure 2.12 for the two vertical cell configuration.

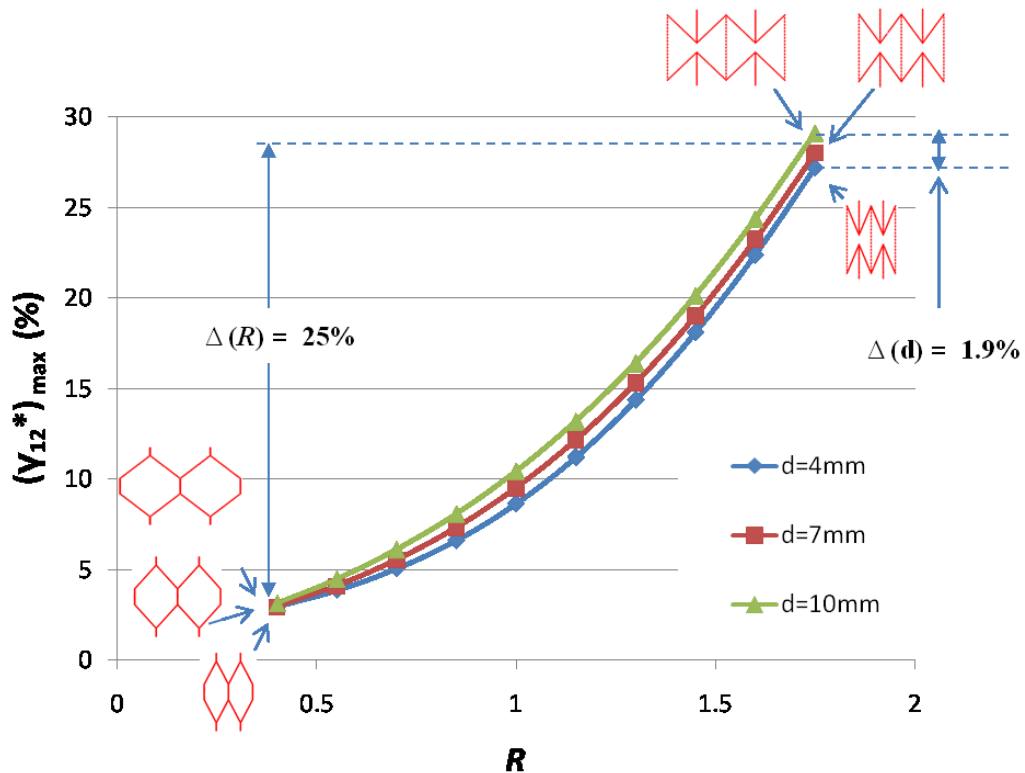


Figure 2.11: Effects of R and d on $(\gamma_{12}^*)_{max}$ ($H=12.7\text{mm}$ $t=0.5\text{mm}$, $N_v=1$).

The significant finding from this study is the relatively small influence the horizontal separation, d , has on the maximum shear strain, $(\gamma_{12}^*)_{max}$. In Figure 2.11 it can be seen that the three lines representing the three horizontal separations have nearly uniform offsets as they increase. Over the range of d values used in this study, from 4 to

10mm, the largest difference in $(\gamma_{12}^*)_{max}$ between the maximum and minimum d values for the same effective height, R , is $\Delta(d)=2\%$. The influence of d on $(\gamma_{12}^*)_{max}$ is therefore small when compared to the effects of effective height, R , which produces a difference in $(\gamma_{12}^*)_{max}$ of approximately 25% over the range of R values used in the study.

The results from Figure 2.12 for the two vertical cell configuration provide the same conclusions on the effects of d on $(\gamma_{12}^*)_{max}$, though the influence of d is larger in this case than in the single vertical cell case. In the two vertical cell configuration, the largest difference in $(\gamma_{12}^*)_{max}$ values with a fixed effective height, R , is $\Delta(d)=3\%$ over the range of d values used in the study, and the difference in $(\gamma_{12}^*)_{max}$ over the range of R values is approximately 16%.

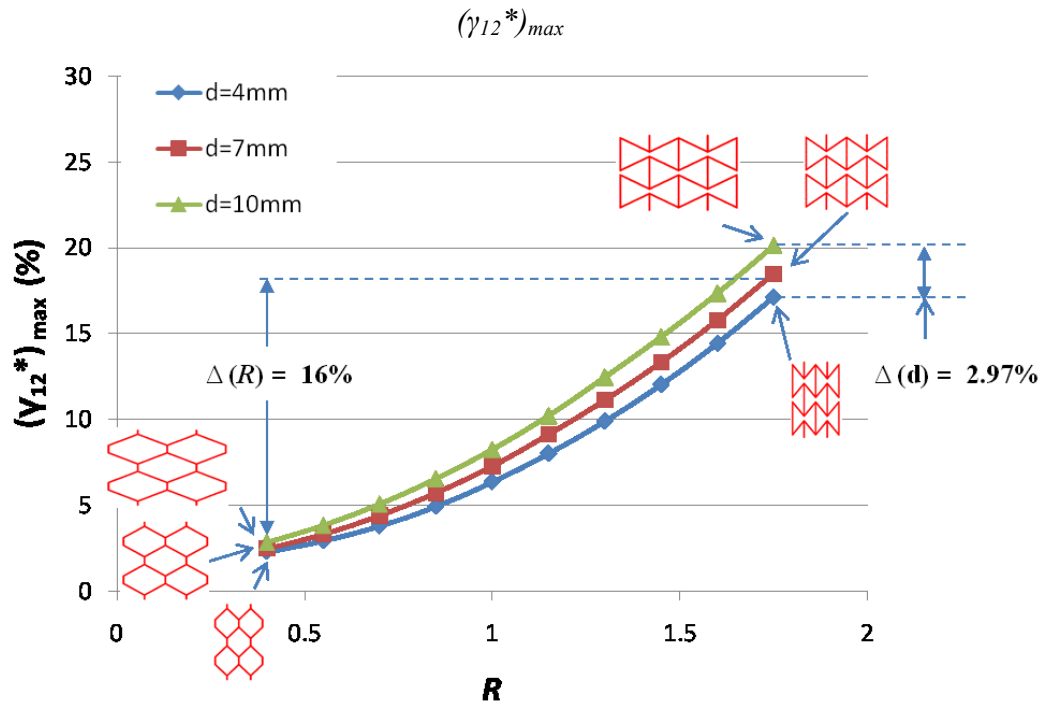


Figure 2.12: Effects of R and d on $(\gamma_{12}^*)_{max}$ ($H=12.7\text{mm}$ $t=0.5\text{mm}$, $N_v=2$).

The relatively small influence of d on $(\gamma_{12}^*)_{max}$ can be attributed to the way in which the parameters, R and d , affect the dimensions of the deformed vertical members; because R and d are decoupled and only R governs the lengths of the vertical members, changes in d do not alter the dimensions of the individual vertical members. As a result, for a fixed effective height, R , the vertical members with the same lengths will begin to yield at approximately the same level of strain regardless of the horizontal separation.

2.1.3 Conventional Parameter Results

The parametric study results for the conventional geometric parameters, h and l , closely resemble the results for the new parameters, R and d . This is to be expected due to the relationships between R and h , and d and l , where R directly describes h in terms of the overall height, H , and d is used to produce l values which give the correct horizontal separation. One difference between the two system studies is that the conventional system requires an additional step to ensure that the overall height, H , is maintained. In the conventional studies, in order to maintain constant l values, the angle θ must continually be modified so that the overall height of the structure is equal to H .

The results for effective shear modulus in Figure 2.13 show that an increase in l causes G_{12}^* to decrease and an increase in h generally causes G_{12}^* to decrease. The use of a constant angled member length, l , causes the shape of the resulting plots to be different from the plots using a constant horizontal separation, d . This is due to the changing angle associated with a constant l value which causes the overall length of the structure to change as h increases with constant l . In the new parameter studies, a

constant d value produces a constant overall structure length, L , used in Equation 2.5 to calculate τ^* , whereas the continually changing overall length in the conventional study causes L to change in Equation 2.5, affecting the shape of the curve.

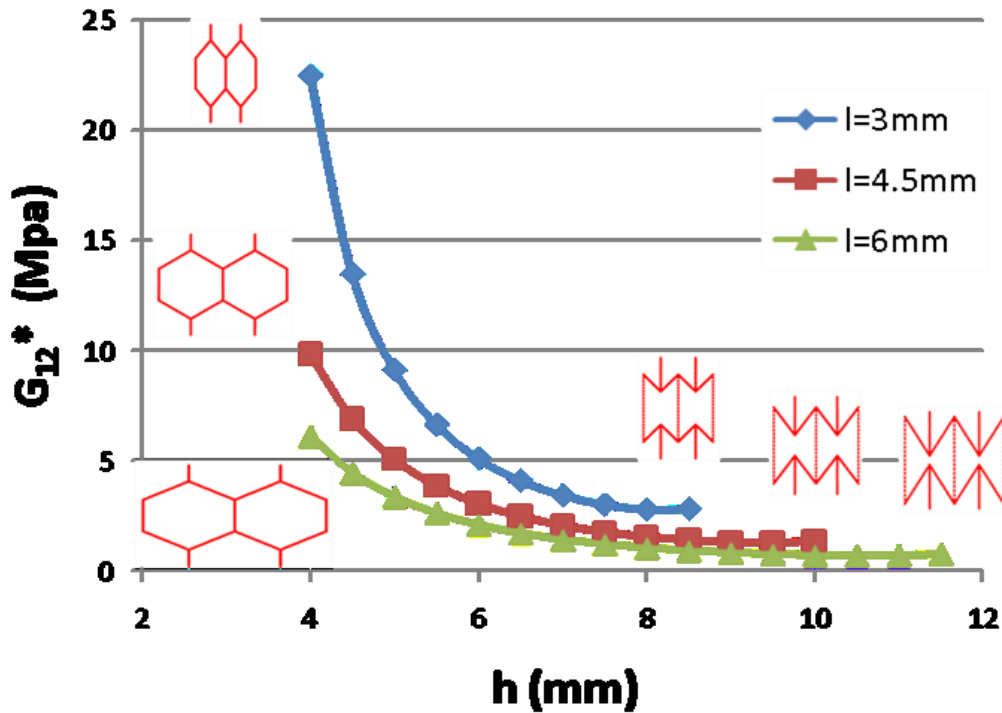


Figure 2.13: Affects of h and l on G_{12}^* ($H=12.7\text{mm}$ $t=0.5\text{mm}$, $N_v=1$).

The results for maximum effective shear strain in Figure 2.14 show that an increase in h will cause an increase in $(\gamma_{12}^*)_{max}$ and that an increase in l causes only a small increase in $(\gamma_{12}^*)_{max}$. Just as d has a relatively small influence on $(\gamma_{12}^*)_{max}$ when R is held constant, the parameter l also has a relatively small influence on $(\gamma_{12}^*)_{max}$ when h is fixed due to the constant lengths of the deformed vertical members.

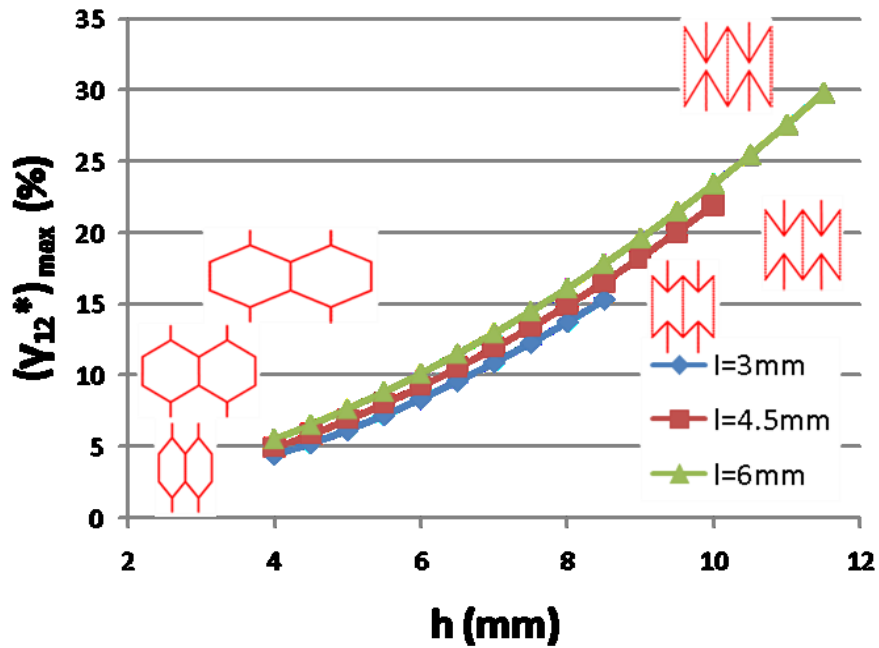


Figure 2.14: Affects of h and l on $(\gamma_{12}^*)_{max}$ ($H=12.7\text{mm}$ $t=0.5\text{mm}$, $N_v=1$).

The resulting effective shear properties for the conventional parameter studies are listed in Table 2.6. The structures with no resulting properties are those which are not feasible due to angled member lengths which are too short to connect the structure as illustrated in Figure 2.8.

Table 2.6: Parametric study data for the conventional parameters with one vertical cell

| $N_v = 1$ | | | $G_{12}^* (Mpa)$ | | | $(\gamma_{12}^*)_{max} (\%)$ | | |
|-----------|----------|-----------|------------------|-------------|-------------|------------------------------|--------------|--------------|
| $h (mm)$ | θ | $l (mm)$ | $l = 3mm$ | $l = 4.5mm$ | $l = 6mm$ | $l = 3mm$ | $l = 4.5mm$ | $l = 6mm$ |
| 4 | 23.06 | 3, 4.5, 6 | 22.48 | 9.84 | 6.09 | 4.46 | 4.93 | 5.52 |
| 4.5 | 17.96 | 3, 4.5, 6 | 13.47 | 6.90 | 4.43 | 5.24 | 5.86 | 6.53 |
| 5 | 13.00 | 3, 4.5, 6 | 9.11 | 5.06 | 3.33 | 6.17 | 6.89 | 7.64 |
| 5.5 | 8.14 | 3, 4.5, 6 | 6.62 | 3.85 | 2.59 | 7.22 | 8.01 | 8.84 |
| 6 | 3.34 | 3, 4.5, 6 | 5.08 | 3.03 | 2.06 | 8.36 | 9.23 | 10.13 |
| 6.5 | -1.43 | 3, 4.5, 6 | 4.07 | 2.45 | 1.67 | 9.59 | 10.53 | 11.50 |
| 7 | -6.22 | 3, 4.5, 6 | 3.41 | 2.03 | 1.39 | 10.90 | 11.91 | 12.95 |
| 7.5 | -11.05 | 3, 4.5, 6 | 2.98 | 1.73 | 1.17 | 12.28 | 13.37 | 14.48 |
| 8 | -15.96 | 3, 4.5, 6 | 2.76 | 1.51 | 1.01 | 13.75 | 14.91 | 16.10 |
| 8.5 | -21.00 | 4.5, 6 | 2.80 | 1.36 | 0.89 | 15.32 | 16.53 | 17.80 |
| 9 | -26.21 | 4.5, 6 | - | 1.27 | 0.79 | - | 18.25 | 19.59 |
| 9.5 | -31.67 | 4.5, 6 | - | 1.24 | 0.72 | - | 20.05 | 21.47 |
| 10 | -37.47 | 4.5, 6 | - | 1.31 | 0.68 | - | 21.95 | 23.43 |
| 10.5 | -43.76 | 6 | - | - | 0.65 | - | - | 25.48 |
| 11 | -50.81 | 6 | - | - | 0.66 | - | - | 27.61 |
| 11.5 | -59.13 | 6 | - | - | 0.72 | - | - | 29.83 |

2.2 PARAMETER SYSTEM COMPARISON

Either system can be used to design a honeycomb material having both a target effective shear modulus and maximum effective shear strain. However, the new system has advantages over the conventional system which can improve the efficiency of the design process.

2.2.1 Design Space Constraints

When designing a cellular material for any application, the resulting material must comply with a specified volume of space. In the case of honeycomb structures, designing for a specific volume can be difficult using the conventional parameters because they are

not related to the design space dimensions. With a set design space, when one parameter is changed, the others must also be modified to maintain a constant volume.

In Figure 2.15 an example design space is set at $H=12.7\text{mm}$ and $L=22\text{mm}$ and the structure needs to be modified so that h increases from 4.2 to 7mm. In Figure 2.15.a, the structure complies with the design space with $h=4.2\text{mm}$, $l=4.2\text{mm}$, and $\theta=30$ degrees. When h is increased from 4.2 to 7mm in Figure 2.15.b the overall height of the structure is greater than the design space height. To reduce the height to equal the design space height, θ is decreased from 30 degrees to -9 degrees in Figure 2.15.c. However, this causes the overall length to increase beyond the design space length, L . Figure 2.15.d shows that final structure having $h=7\text{mm}$ which complies with the design space after all parameters are adjusted. These processes cause additional complexity to the design process because the combination of parameter values must produce the correct overall dimensions in addition to producing the desired effective properties.

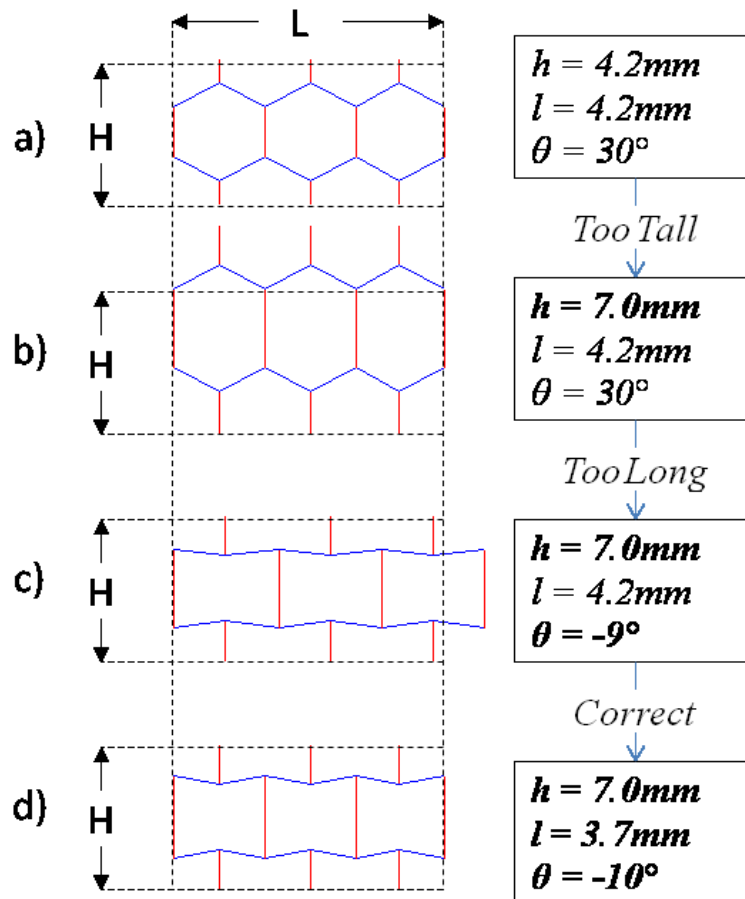


Figure 2.15: Illustration of the parameter modifications required to comply with a given design space when h is changed from 4.2 to 7.0mm using the conventional system.

The new system of parameters reduces this complication by associating each new parameter to the overall design space, where R is related to the overall height by $R=H'/H$, and d is related to the total length by $d=L/N_h$. Based on these relations, the parameters can be changed without altering the overall dimensions of the material. Additionally, the two new parameters are fully independent of each other, allowing for one parameter to be fixed while the other is altered, as illustrated in Figure 2.16.

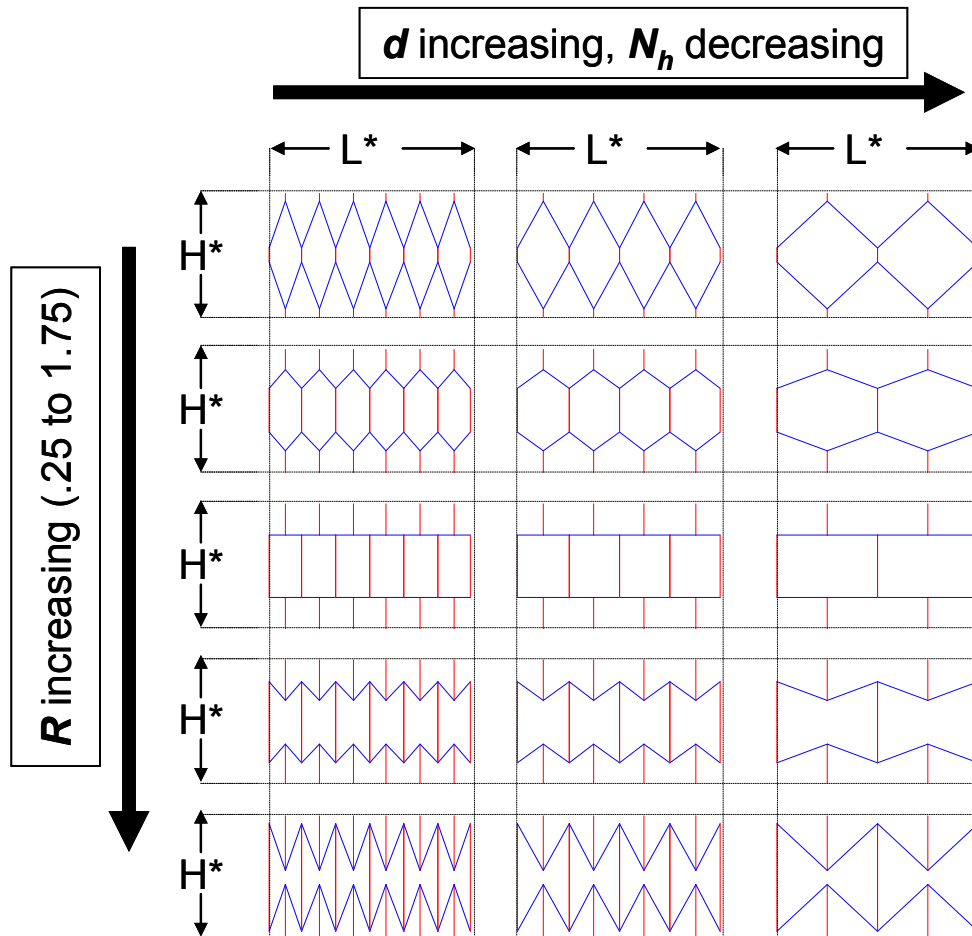


Figure 2.16: Illustration of how modifications to R and d affect the structure.

For all of the structures shown in Figure 2.16, the design space height, H , and length, L , are held constant. Moving from top to bottom, the effective height, R , is increased, causing the lengths of the vertical members to increase while maintaining a constant overall height, H . Moving from left to right, the horizontal separation, d , is increased and the number of horizontal cells is decreased to comply with the overall design space.

2.2.2 Parameter-Property Relations

The parameter-property relationships found in the parametric studies do share some resemblance between the two systems. The effect of $R(h, H)$ is positively correlated to $(\gamma_{12}^*)_{max}$ and are generally correlated negatively with G_{12}^* , and $d(l, \theta)$ is negatively correlated with G_{12}^* and has small effects on $(\gamma_{12}^*)_{max}$.

One significant difference between the two systems is in the parameter relationships to the effective shear modulus, G_{12}^* . This is due to differences in the definition of d and l . When l is held constant while h increases as shown in Figure 2.13, the additional angle parameter, θ , must also change with h for the overall height to remain constant. The change in angle causes the horizontal separation, and subsequently, the overall length, L , to change.

As a result, the changes in G_{12}^* are due to both the vertical member stiffness and the horizontal density of the vertical members along the length of the structure. That is, the changing overall length, L , affects the shear strain found in Equation 2.5, and a different number of vertical members must be deformed over a given length of the structure. The effects of both the vertical member stiffness and density on effective shear modulus can be seen in Figure 2.17 which shows the effective shear modulus, G_{12}^* , horizontal separation, d , and θ as h increases and l is constant at 3mm. When the angle is positive, as shown in Figure 2.17.a, increases in h cause the horizontal separation, d , to increase due to a corresponding decrease in θ required to maintain a constant length l . The increase in h decreases the stiffness of the vertical members and the corresponding increase in d decreases the density of the deformed members. Together, both of these

factors contribute to decreased effective shear modulus and result in a sharp decline in G_{12}^* when h is small. When the angle is negative, as shown in Figure 2.17.c, increases in h cause d to decrease. In this region, increases in h cause the member density to increase while the member stiffness continues to decrease. These two factors have opposite effects on effective shear modulus, causing the plot for G_{12}^* to flatten despite increasing h .

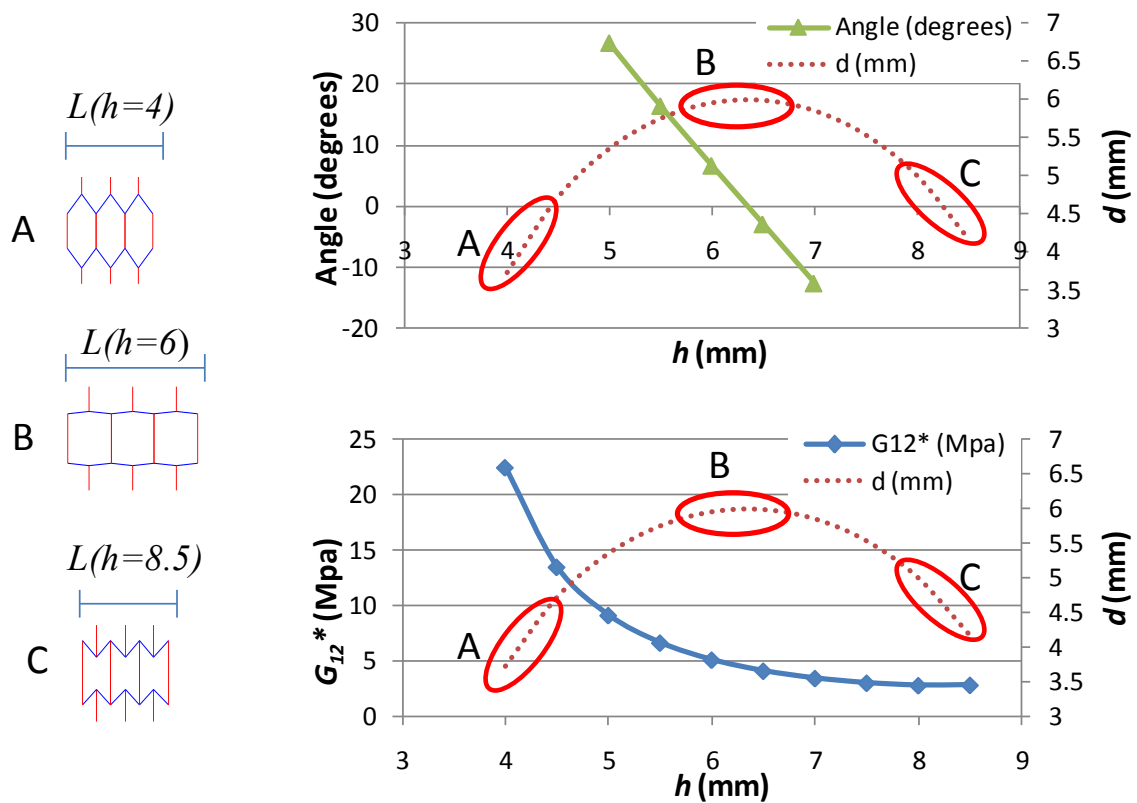


Figure 2.17: Angle change required to maintain constant overall height, H , when angled member length, l , is constant, resulting in a change in horizontal separation

In the new system, when d is held constant changes to R do not affect the overall length, L , so the number of deformed members over a given length of the structure

remains constant. As a result, the changes to G_{12}^* as R increases in Figure 2.9 are due only to the effects of the changing stiffness of the vertical members.

2.3 HONEYCOMB DESIGN METHOD

In the new system of parameters, when the wall thickness, t , and vertical layers, N_v , are held constant, only one of the remaining design variables, R , significantly affects $(\gamma_{12}^*)_{max}$. This aspect is used in a new design method to design for both G_{12}^* and $(\gamma_{12}^*)_{max}$ at the same time. In this method, t and N_v are fixed initially and R and d are designed to produce the desired G_{12}^* and $(\gamma_{12}^*)_{max}$ in two steps. In the first step, d is temporarily fixed and a value for R is found to give the target value of $(\gamma_{12}^*)_{max}$. In the second step, the value of R found in step 1 is held constant and a value for d is found giving the target value of G_{12}^* . As discussed in Section 2.1.2, d has a relatively small affect on $(\gamma_{12}^*)_{max}$, so that changes to d in step 2 will cause only small changes to the value of $(\gamma_{12}^*)_{max}$ found in step 1. Figure 2.18 illustrates how both effective properties are designed for using this method.

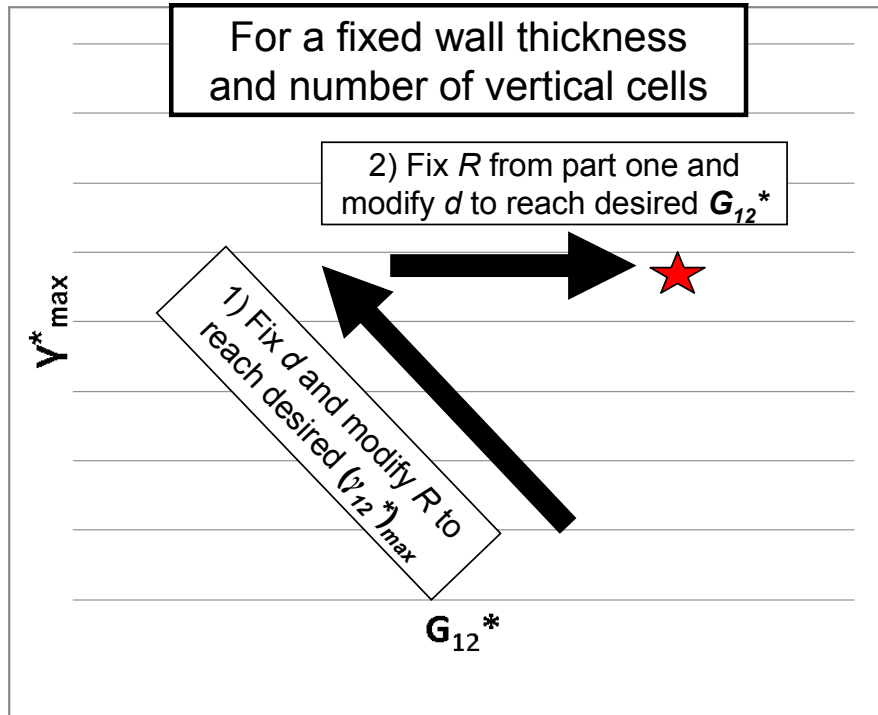


Figure 2.18: Schematic of the new design method

2.3.1 Affects of N_h on G_{12}^*

To design the structure to comply with the design space length, the values for d must be chosen so that the number of horizontal cells, N_h , in Equation 2.2 is an integer value. In the second step of the design process when R is fixed, it is beneficial to use L and integer values for N_h to design for d to ensure that the resulting structures have the desired dimensions. In Figure 2.19, the design length, L , is fixed and G_{12}^* is plotted as N_h increases.

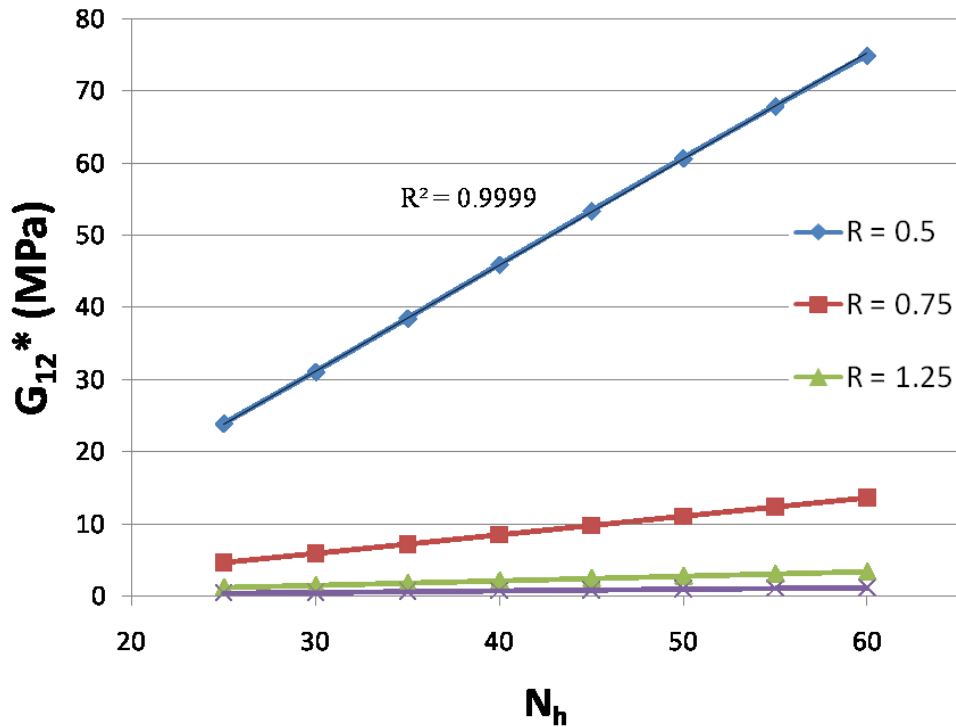


Figure 2.19: Affects of N_h on G_{12}^* when L and R are constant.

The results show that for a fixed overall length, L , and effective height, R , G_{12}^* will increase linearly as the number of horizontal cells increase. To more efficiently design d , this linear relationship can be used to find a value for N_h giving the target G_{12}^* and d can be calculated using Equation 2.2.

2.4 HONEYCOMB DESIGN ALGORITHM

A honeycomb design algorithm is developed and implemented using the new method to aid in the design process. The inputs for the algorithm, shown in Table 2.7, are the constituent material properties, the wall thickness and number of vertical cell layers, and the desired effective shear properties. The outputs are the resulting structural geometry and the resulting effective properties. Within the algorithm, the steps

developed in the honeycomb design method are automated to design the geometry parameters, R and d , to target the desired effective shear properties.

Table 2.7: Honeycomb design algorithm inputs and outputs

| INPUTS | OUTPUTS |
|---|--|
| Constituent Material Properties <ul style="list-style-type: none"> • Young’s Modulus (E) • Poisson’s Ratio (ν) • Yield Stress (σ_{max}) Structure Parameters <ul style="list-style-type: none"> • Overall Height (H) • Overall Length (L) • Wall Thickness (t) • Vertical Cells (N_v) Target Properties <ul style="list-style-type: none"> • Effective Shear modulus (G_{12}^*) • Max Effective Shear Strain $((\gamma_{12}^*)_{max})$ | Resulting Structure <ul style="list-style-type: none"> • Effective Height (R) • Horizontal Separation (d) • Horizontal Cells (N_h) Resulting Properties <ul style="list-style-type: none"> • Effective Shear modulus (G_{12}^*) • Max Effective Shear Strain $((\gamma_{12}^*)_{max})$ |

The honeycomb design algorithm is implemented using a Matlab program which works with Abaqus FEA. The Matlab program is responsible for constructing the honeycomb geometry based on the input parameters and for performing all calculations and iterative processes required for the design process. The Matlab program also creates analysis jobs in Abaqus by generating Abaqus input files containing all of the material, geometry, and boundary condition information required for the analysis. After the Abaqus analysis is completed, Matlab extracts the desired results which are then used in the algorithm.

2.4.1 Honeycomb Design Algorithm Flow Chart

The honeycomb design algorithm flow chart is provided in Figure 2.20. The algorithm begins by taking the necessary input information about the structure (Table 2.7) and determines the initial horizontal separation, d_I , used in the first step of the design process. The algorithm then executes the two step process to design the geometry required to produce the desired effective shear properties. After the process is completed, the final geometry and effective properties are stored and the input parameters can be modified to generate additional designs.

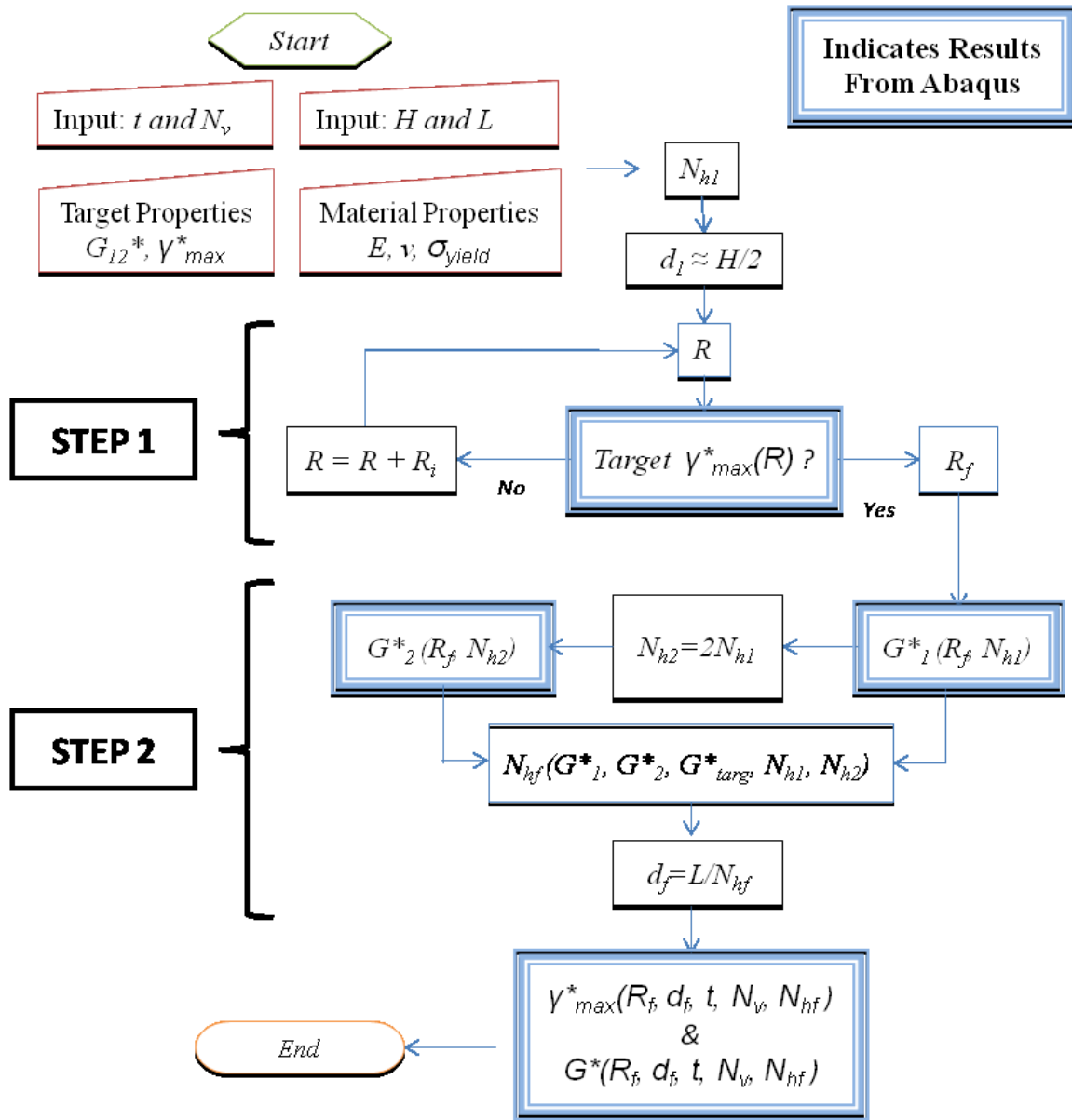


Figure 2.20: Honeycomb design algorithm flow chart.

2.4.1.1 Honeycomb Algorithm Inputs

The inputs for the program, shown in Figure 2.21, are the constituent material properties, the overall design space dimensions, the target effective properties, and the cell wall thickness and the number of vertical cells.

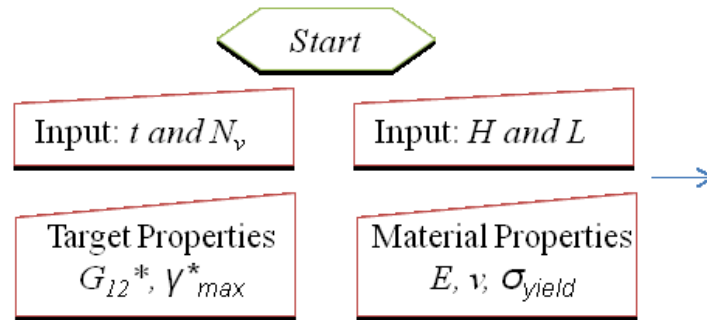


Figure 2.21: Honeycomb Algorithm inputs.

The overall design space dimensions are input in terms of the overall height, H , and the overall length, L . A third depth dimension is not required due to the assumption of plane stress used in the analysis and because the desired information from the analysis, G_{12}^* and $(\gamma_{12}^*)_{max}$, are independent of the structure depth. These dimensions determine the total area occupied by the honeycomb structure as shown in Figure 2.22. Three dimensional honeycomb structure design is deemed out of scope for this research and is reserved for future work.

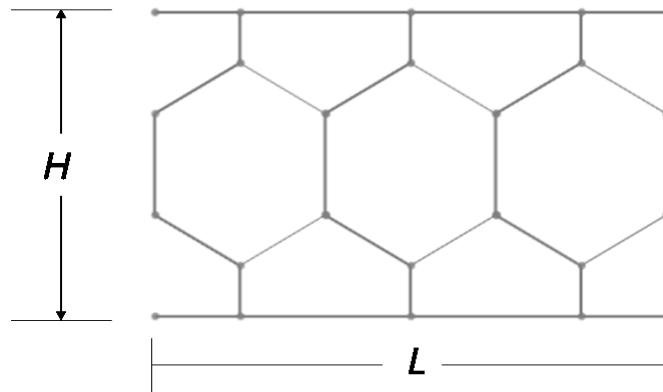


Figure 2.22: Overall honeycomb dimension inputs.

The material property inputs are the mechanical properties of the constituent material used to build the honeycomb structures. The analysis used in this algorithm is

only concerned with the elastic range of material deformation before yielding occurs. As such, the analysis assumes that the material is elastic and the only properties of importance are the Elastic modulus, E , Poisson's ratio, ν , and the yield stress of the material, σ_y .

The target effective shear properties are input into the algorithm in two ways due to the different methods used by the algorithm to design for each property. The maximum shear strain is designed through an iterative process, where the parameter R is modified until the resulting $(\gamma_{12}^*)_{max}$ is within an input minimum and maximum range. The effective shear modulus, G_{12}^* , is design by modifying the parameter d in a single calculation so the target value can be input as a single value. For example, if it is desired that $(\gamma_{12}^*)_{max}$ be approximately 10.25% and G_{12}^* be approximately 4.25 MPa, the target inputs will be $G_{12}^*=4.25\text{Mpa}$ and $10\% < (\gamma_{12}^*)_{max} < 10.5\%$.

The final inputs into the system (Figure 2.23) are the cell wall thickness, t , and the number of vertical cell layers, N_v . The wall thickness describes the beam thickness of each member of the honeycomb structure and has a significant influence on the final structural geometry as the effective properties are dependent on the deformation characteristics of these members. The number of vertical cell layers, N_v , determines the number of honeycomb unit cells within the overall height, H , dimension of the structure. The number of vertical cell layers is typically small (from one to two) due to the assumption that the overall height, H , is small relative to the length, L , for the current application.

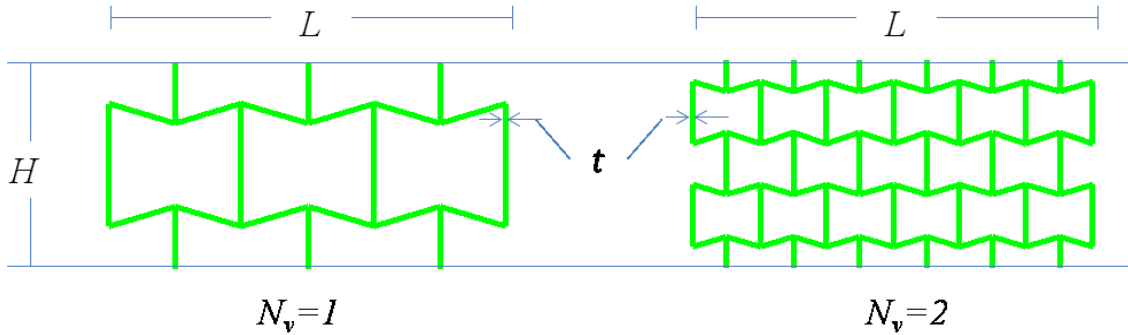


Figure 2.23: Honeycomb algorithm wall thickness, t , and number of vertical cells, N_v .

2.4.1.2 Initial Horizontal Separation, d_1

Before the design method can continue, there must be an initial horizontal separation value, d_1 , to be used in the first design step. In the first design step, an initial horizontal separation, d_1 , is held constant and the effective height, R , is modified to achieve the target range for $(\gamma_{12}^*)_{max}$. According to the assumptions made in the development of the design method, the initial horizontal separation should not matter in the first design step because it is assumed that future changes to d will not affect the resulting value for $(\gamma_{12}^*)_{max}$ found in step one. In reality, large modifications to d in step two of the design do have some effect on $(\gamma_{12}^*)_{max}$ which can cause the final $(\gamma_{12}^*)_{max}$ value to fall outside of the target range. For this reason, it is necessary to have an initial value for d to be used in step one which is similar to the final horizontal separation values produced. That is, the initial value for d should be somewhat representative of the final designed value to prevent large changes to $(\gamma_{12}^*)_{max}$.

In the current form, the initial horizontal separation is calculated to be approximately equal to half the overall height H . It is approximate because a whole

number of horizontal cells, N_{hl} , must extend along the length, L , of the structure. To find d_l , the number of horizontal cells is first calculated using Equation 2.9.

Equation 2.9
$$N_{hl} = \left\| \frac{2L}{H} \right\|$$

This gives a whole number for N_{hl} which will produce horizontal separations of $d_1 = \frac{L}{N_{hl}} \approx \frac{H}{2}$.

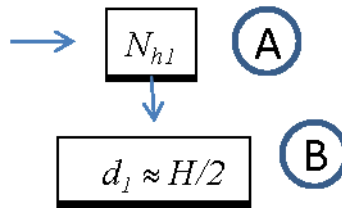


Figure 2.24: Honeycomb algorithm initial horizontal separation, d_l .

The use of the initial separation of $d_1 \approx \frac{H}{2}$ is shown to be an appropriate initial value in the example problems discussed in Section 2.5. In those examples, the honeycomb algorithm is tested by designing eight different structures for each of three target design scenarios. In each case, the final designed horizontal separations, d_f , are both greater than and less than the initial separation of $d_l=6.3\text{mm}$ with an overall height of $H=12.7\text{mm}$, meaning that the initial value of $d_1 \approx \frac{H}{2}$ will require d to increase and decrease to achieve the desired G_{l2}^* depending on the input dimensions of the structures.

2.4.1.3 Honeycomb Design Step 1: Design for $(\gamma_{l2}^*)_{\max}$

The first step in the design process is to find the effective height, R , which will result in maximum shear strain, $(\gamma_{l2}^*)_{\max}$, within the target range. Figure 2.25 illustrates the basic process used in the algorithm for design step 1, where many structures are given

which have the same horizontal separation, d , and different effective heights, R . The algorithm uses an iterative process in which d is held constant, and the parameter R is modified until the resulting maximum effective shear strain, $(\gamma_{12}^*)_{max}$, is within a specified range.

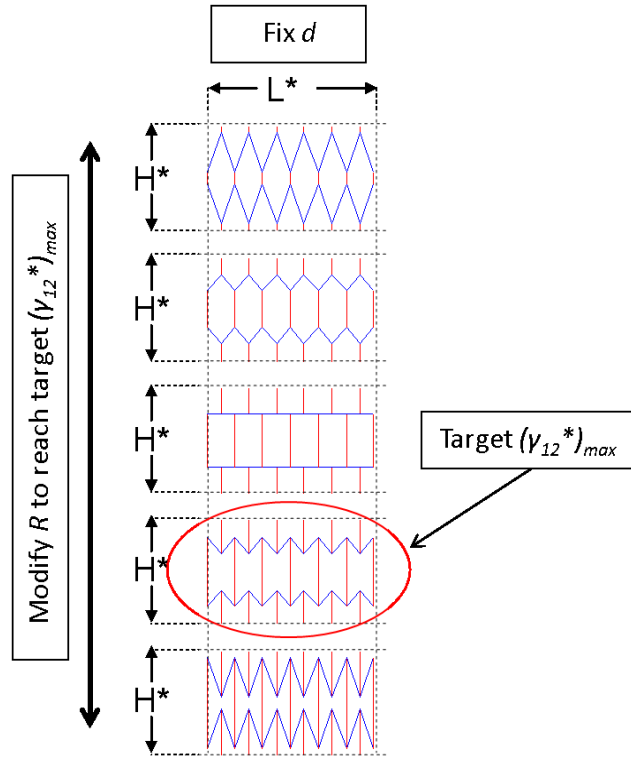


Figure 2.25: Visualization of honeycomb algorithm design step 1.

Figure 2.26 provides the flow chart for this design step, where the initial horizontal separation, d_I , is fixed, and a bisection loop is used to design R .

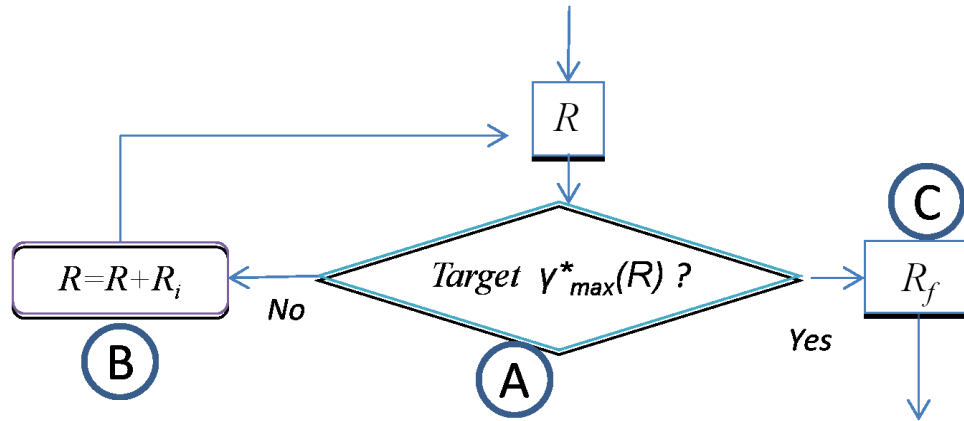


Figure 2.26: Honeycomb algorithm design step 1: Finding the effective height, R , to produce the desired maximum shear strain, $(\gamma_{12}^*)_{max}$.

The bisection method starts with an initial value for R and an upper and lower bound for the possible values of R . The algorithm then finds the corresponding value for $(\gamma_{12}^*)_{max}$, and depending on whether $(\gamma_{12}^*)_{max}$ is greater than or less than the target range, a new value for R is calculated which is the midpoint between the current R value and the upper or lower bound. In the next iteration, a new bound is set at the previous R value. As there is a positive correlation between R and $(\gamma_{12}^*)_{max}$, if $(\gamma_{12}^*)_{max}$ is below the target range, the previous R value becomes the new lower bound, and if it is above the target range, the previous R value becomes the new upper bound. The bisection method has two properties which make it advantageous for this application; it quickly approaches the solution because each iteration reduces the range of possible values by half, and it can be used to limit the range of possible solution values as required for R . Additionally, the bisection methods guarantees solution convergence if it is possible to achieve the desired $(\gamma_{12}^*)_{max}$ within the range limit of R due to the continuous positive relationship shown in Figure 2.11.

The bisection loop is initialized by placing bounds on the possible resulting values for R . As mentioned in previous sections, R must be greater than 0 and less than 2 to prevent the structural members from overlapping. The algorithm sets the initial bounds as $0.2 < R < 1.8$, and uses $R=1$ for the first iteration. In Figure 2.26a, the corresponding value for $(\gamma_{12}^*)_{max}$ is found in an Abaqus analysis and a new value for R is calculated using the bisection method in Figure 2.26b. When the resulting $(\gamma_{12}^*)_{max}$ is within the target range, the bisection loop is ended and the final effective height, R_f , is sent to the second design step.

2.4.1.4 Honeycomb Design Step 2: Design for G_{12}^*

In the second design step of the algorithm, the value for R_f found in step one is held constant and a final value for d , d_f , is found to give the target G_{12}^* . Figure 2.27 illustrates the basic process used in design step 2, where multiple structures are shown with equal effective heights, R , and different horizontal separations, d . The objective of this step is to determine which horizontal separation, d , will result in the target effective shear modulus, G_{12}^* , when R is equal to the designed value, R_f , from design step 1.

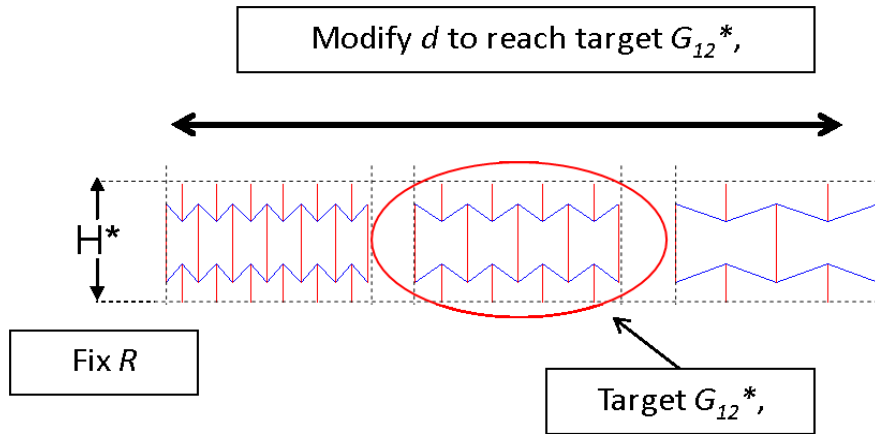


Figure 2.27: Visualization of honeycomb design algorithm step 2.

In Figure 2.28 the algorithm flow chart for this step is provided. This step of the algorithm uses the number of horizontal cells, N_h , to find the final horizontal separation, d_f , because of the linear relationship between N_h and G_{12}^* which allows for d_f to be calculated directly without the need for an iterative process. The use of N_h in this step also makes it easier to ensure that there are a whole number of horizontal cells along the length of the structure.

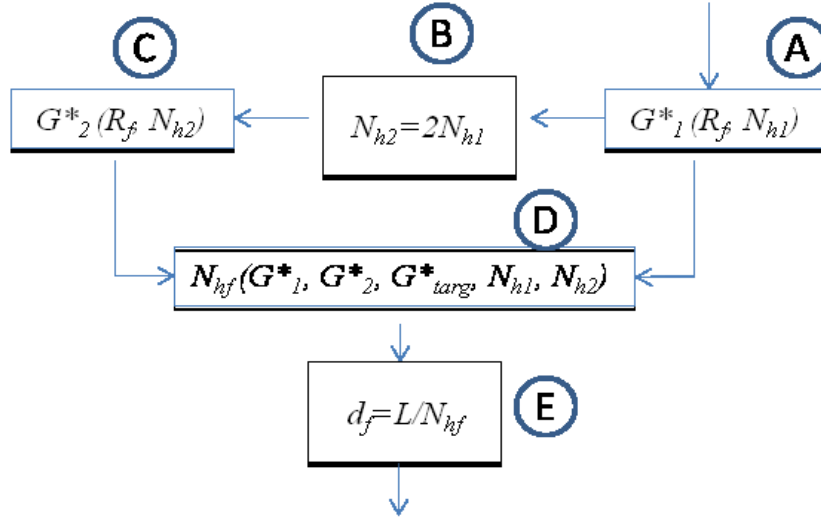


Figure 2.28: Honeycomb algorithm design step 2: Finding the horizontal separation, d_f , to produce the desired effective shear modulus, G_{12}^* .

In order to use the linear relationship between N_h and G_{12}^* , shown in Figure 2.29, two data points are required before the final number of horizontal cells can be calculated. The first data point, shown in Figure 2.28a, is the effective modulus using the same number of horizontal cells as used in design step 1. A second data point is then found using twice the number of horizontal cells, N_{h2} , as used in step one as shown in Figure 2.28a-b. Using these two data points, $G_{12}^*(N_{h1})$ and $G_{12}^*(N_{h2})$, a final number of horizontal cells can be found to produce the desired effective shear modulus, $G_{12}^*(N_{hf})$, using Equation 2.10:

$$\text{Equation 2.10: } N_{hf} = \left[N_{h1} + \left(\frac{(G_{12}^*)_{targ} - (G_{12}^*)_1}{(G_{12}^*)_2 - (G_{12}^*)_1} \right) (N_{h2} - N_{h1}) \right]$$

The final horizontal separation, d_f , can then be calculated based on N_{hf} and the overall length, L , using the equation: $d_f = \frac{L}{N_{hf}}$.

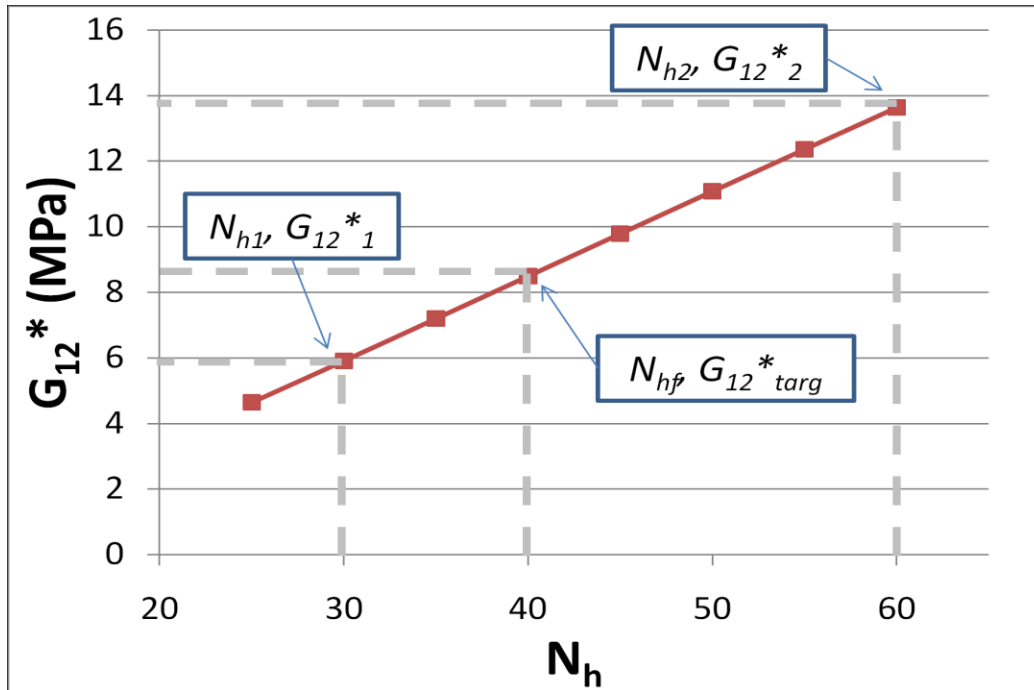


Figure 2.29: Linear relationship used to calculate N_{hf} for the desired shear modulus, G_{12}^* . The linear relationship is only true if effective height, R , is constant.

2.4.1.5 Honeycomb Algorithm Outputs

Once the final geometry parameters, R_f and d_f , are known, the algorithm executes one final analysis to find the final resulting effective properties, G_{12}^* and $(\gamma_{12}^*)_{max}$. The final property and geometry information is then reported before the algorithm ends as shown in Figure 2.30. If multiple designs are desired having different combinations of wall thickness and vertical cells, these input parameters can be changed automatically and the algorithm will continue to run with the new conditions, producing many designs at once.

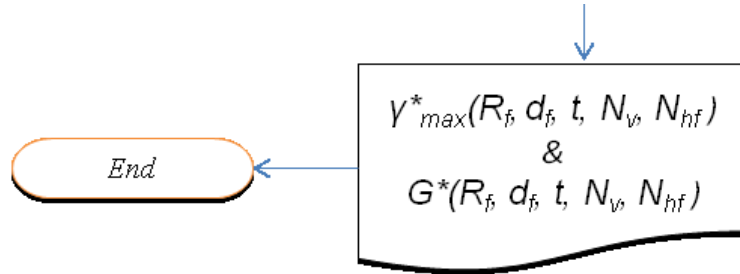


Figure 2.30: Honeycomb algorithm outputs.

2.4.2 Honeycomb Algorithm Properties

The algorithm is developed to be a generic process for designing honeycomb structures for both shear modulus and shear compliance within a specific design space. There are, however, some limitations to this process which must be considered.

First, the use of beam elements for the analysis requires some precaution when analyzing the final results. As they do not account for cell wall overlap at the points of connection, structures resulting in low aspect ratios should be further analyzed using non-beam elements.

Second, although changes to $d(N_h, L)$ do not significantly affect $(\gamma_{12}^*)_{max}$ relative to R , large changes to d in the second step of the algorithm will cause the resulting value of $(\gamma_{12}^*)_{max}$ to drift from the original value found in step one. This can result in structures having $(\gamma_{12}^*)_{max}$ outside the range specified by the user. In order to decrease the amount of drift, N_{hf} should be chosen so that it is closer to the final value, N_{hf} .

Finally, as there are no limits placed on N_{hf} , the resulting structures can have a small horizontal separation, d , causing large cell wall overlap.

2.5 DESIGN FOR TARGET SHEAR PROPERTIES

The honeycomb design algorithm is validated by using it to design honeycomb structures to reach three sets of desired properties. The three target property combinations are selected to test the algorithm over a variety of design applications; the first design requires moderate target values for both G_{12}^* and $(\gamma_{12}^*)_{max}$, and the final two designs require one high target value and one low target value. Each structure is designed to have equal design space dimensions of $H=12.7\text{mm}$ and $L=250\text{mm}$ and uses polycarbonate as the base material.

As discussed in the previous section, the design algorithm approaches the target property values by modifying the geometry of the honeycomb structure with a given cell wall thickness and number of vertical cell layers. Here, eight different initial structures are modified to reach the target properties. The eight structures have cell wall thickness of 0.5, 0.75, 1, and 1.25mm with either one or two vertical unit cells. For each target solution, all eight of the initial structures are modified producing eight separate designs.

In each execution of the algorithm, two loops are used in Matlab to change the cell wall thickness and to change the number of vertical cell layers. The steps discussed in the previous section are executed to find the values for R and d for each combination of cell wall thickness and vertical cells within the loop. After completion, the geometry data and the resulting effective properties are stored and the design process repeats for the next combination of wall thickness and vertical cells. The only difference for the three design scenarios are the desired properties input into the algorithm; in the first example the target values are $G_{12}^*=4.25\text{Mpa}$ and $10\% < (\gamma_{12}^*)_{max} < 10.5\%$, in the second example

the values are $G_{12}^*=2.25\text{Mpa}$ and $15\% < (\gamma_{12}^*)_{\max} < 15.5\%$, and in the third example the values are $G_{12}^*=10\text{Mpa}$ and $6\% < (\gamma_{12}^*)_{\max} < 6.5\%$.

2.5.1 Validation Results

The resulting effective properties for the three design cases are shown in Figure 2.31. Each collection of data points represents a different algorithm execution with different target properties, and the individual points represent the resulting properties for different combinations of wall thickness and vertical cells.

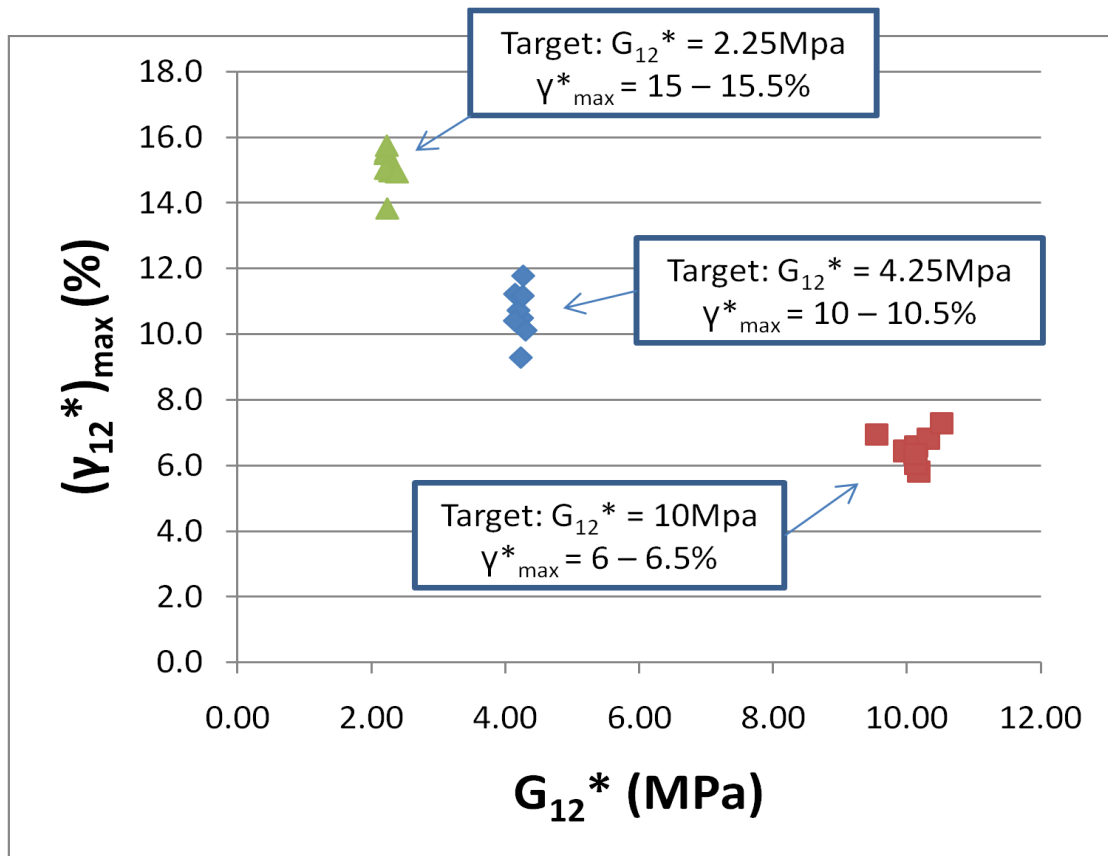


Figure 2.31: Resulting effective properties for three target design cases.

In Figure 2.32 through Figure 2.34, the individual design cases are provided in more detail and show that not all of the resulting structures are within the target property ranges. However, from Figure 2.31 it can be seen that the design algorithm is capable of generating multiple honeycomb structures to closely match the target property combinations over a range of design cases.

The results for the individual design cases are shown in Figure 2.32 through Figure 2.34 and the geometry data is provided in Table 2.8 through Table 2.10. The labels in the figures correspond to the structures described in the tables, and the dashed lines indicate the target properties; where the target values for maximum shear strain lie between the two horizontal lines and the target value for effective shear modulus is the vertical line.

Figure 2.32 shows the resulting properties for the design case where both target property values are moderate ($G_{12}^*=4.25\text{Mpa}$, $10\% < (\gamma_{12}^*)_{max} < 10.5\%$). The horizontal dashed lines displayed in Figure 2.32 represent the upper and lower target boundaries for $(\gamma_{12}^*)_{max}$, and the vertical line represents the target value for G_{12}^* . An ideal design would result in effective properties which lie along the vertical dashed line in between the two horizontal lines.

Of the eight structures designed using the algorithm, three (structures B, E, and G) achieved the desired range for $(\gamma_{12}^*)_{max}$, and all but one (structure A) result in values above the minimum target value for $(\gamma_{12}^*)_{max}$. Considering that the objective of this design is to produce structures which have a specific shear modulus while also being able to reach a certain level of shear strain before yielding occurs, the structures resulting in

maximum shear strains above the specified target level are considered to be viable structures as they are greater than the minimum value required. As a result, seven of the eight structures produced by the algorithm reach the maximum shear strain constraints for the material.

Of the seven viable structures, three (structures B, F, and H) have effective shear modulus values with errors less than 0.5% of the target value of $G_{12}^*=4.25\text{Mpa}$, and the remaining four structures (structures C, D, E, and G) have errors of less than 2.6%.

Observing Figure 2.32, structure B is considered to be the best structure for the specified target properties as it has the target effective shear modulus and is within the target range for $(\gamma_{12}^*)_{max}$. However, the purpose of the honeycomb design algorithm is not to design the structures to achieve the target properties exactly, rather, the objective is to quickly produce many structures which approximate the target values without the use of optimization. The resulting structures can be judged based on additional criteria such as weight and manufacturability, and the final structure can then be further refined to achieve an acceptable level of error.

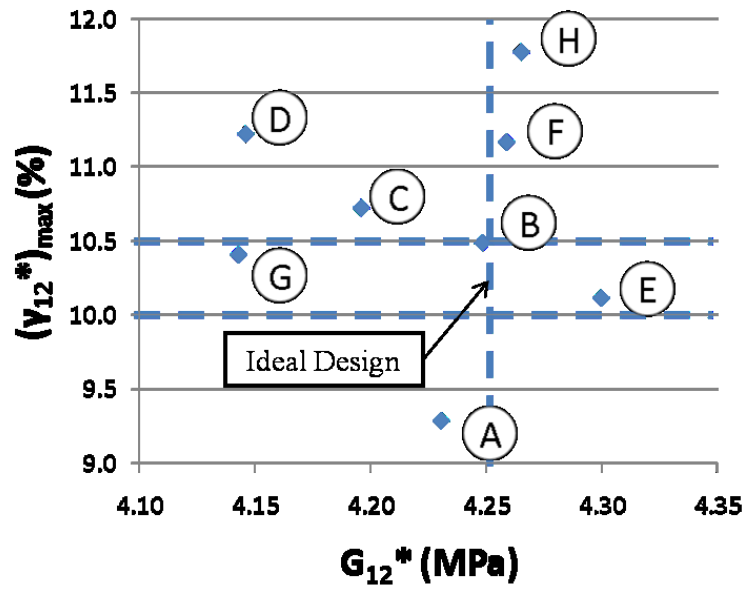
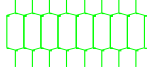
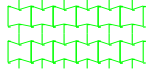

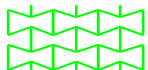
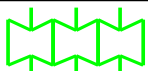

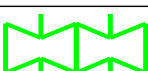
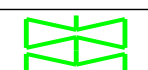


Figure 2.32: Resulting effective properties for targets: $G_{12}^*=4.25\text{Mpa}$, $10\% < (\gamma_{12}^*)_{max} < 10.5\%$

Table 2.8: Structural geometry and effective properties for Figure 2.32.

| Target: $G_{12}^* = 4.25\text{Mpa}$ $\gamma_{\max}^* = 10 - 10.5\%$ | | Thickness (mm) | N_v | N_h | R | d (mm) | G_{12}^* (Mpa) | G_{12}^* (Error) | γ_{\max}^* (%) | γ_{\max}^* (Error) |
|--|---|-------------------|-------|-------|-------|-----------|---------------------|-----------------------|--------------------------|------------------------------|
| A ₁ |  | 0.5 | 1 | 81 | 0.95 | 3.1 | 4.23 | -0.5% | 9.3 | -7.1% |
| B ₁ |  | 0.5 | 2 | 62 | 1.2 | 4.0 | 4.25 | 0.0% | 10.5 | 0.0% |
| C ₁ |  | 0.75 | 1 | 48 | 1.25 | 5.2 | 4.20 | -1.3% | 10.7 | 2.2% |
| D ₁ |  | 0.75 | 2 | 31 | 1.45 | 8.1 | 4.15 | -2.5% | 11.2 | 6.9% |
| E ₁ |  | 1 | 1 | 31 | 1.3 | 8.1 | 4.30 | 1.2% | 10.1 | 0.0% |
| F ₁ |  | 1 | 2 | 21 | 1.5 | 11.9 | 4.26 | 0.2% | 11.2 | 6.4% |
| G ₁ |  | 1.25 | 1 | 20 | 1.425 | 12.5 | 4.14 | -2.5% | 10.4 | 0.0% |
| H ₁ |  | 1.25 | 2 | 14 | 1.6 | 17.9 | 4.27 | 0.4% | 11.8 | 12.2% |

In Figure 2.33 the results are provided for the design case where high shear modulus and low maximum shear strain are required ($G_{12}^*=10.25\text{Mpa}$, $6\% < (\gamma_{12}^*)_{\max} < 6.5\%$). Of the eight structures produced in this example, three (structures B, E, and G) are within the target range for $(\gamma_{12}^*)_{\max}$, and all but structure A are above the minimum required maximum shear strain. Of the viable structures, four (structures C, E, F, and G) have errors of less than 1.2% from the desired effective shear modulus of $G_{12}^*=10.25\text{Mpa}$, and the remaining viable structures have errors of less than 6.9%.

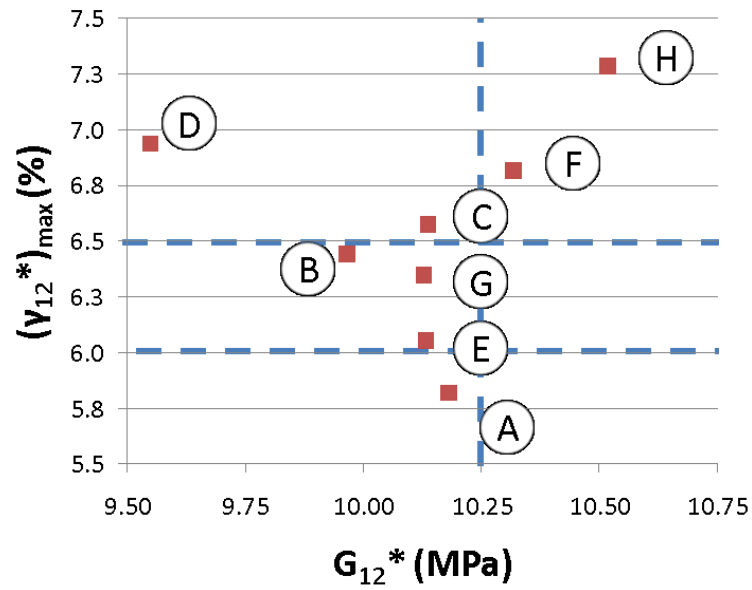
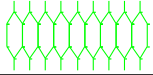
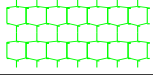
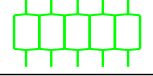

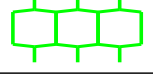





Figure 2.33: Resulting effective properties for targets: $G_{12}^*=10.25$ Mpa, $6\% < (\gamma_{12}^*)_{max} < 6.5\%$

Table 2.9: Structural geometry and effective properties for Figure 2.33.

| Target: $G_{12}^* = 10\text{Mpa}$ $\gamma_{\max}^* = 6 - 6.5\%$ | | thickness (mm) | N_v | N_h | R | d (mm) | G_{12}^* (Mpa) | G_{12}^* (Error) | γ_{\max}^* (%) | γ_{\max}^* (Error) |
|--|---|-------------------|-------|-------|-------|-----------|---------------------|-----------------------|--------------------------|------------------------------|
| A ₂ |  | 0.5 | 1 | 88 | 0.675 | 2.8 | 10.18 | 1.8% | 5.8 | -3.3% |
| B ₂ |  | 0.5 | 2 | 68 | 0.9 | 3.7 | 9.97 | -0.3% | 6.4 | 0.0% |
| C ₂ |  | 0.75 | 1 | 54 | 0.95 | 4.6 | 10.14 | 1.4% | 6.6 | 1.5% |
| D ₂ |  | 0.75 | 2 | 32 | 1.05 | 7.8 | 9.55 | -4.5% | 6.9 | 6.2% |
| E ₂ |  | 1 | 1 | 32 | 0.95 | 7.8 | 10.13 | 1.3% | 6.1 | 0.0% |
| F ₂ |  | 1 | 2 | 22 | 1.05 | 11.4 | 10.32 | 3.2% | 6.8 | 4.6% |
| G ₂ |  | 1.25 | 1 | 22 | 1.05 | 11.4 | 10.13 | 1.3% | 6.3 | 0.0% |
| H ₂ |  | 1.25 | 2 | 15 | 1.1 | 16.7 | 10.52 | 5.2% | 7.3 | 12.3% |

In Figure 2.34 the results are provided for the design case where low shear modulus and high maximum shear strain are required ($G_{12}^*=2.25\text{Mpa}$, $15\% < (\gamma_{12}^*)_{\max} < 15.5\%$). Of the eight structures produced in this example, four (structures C, E, F, and G) are within the target range for $(\gamma_{12}^*)_{\max}$, and all but two structures (structures A, and F) are above the minimum required maximum shear strain. All of the viable structures have errors of less than 1.4% from the desired effective shear modulus of $G_{12}^*=2.25\text{Mpa}$.

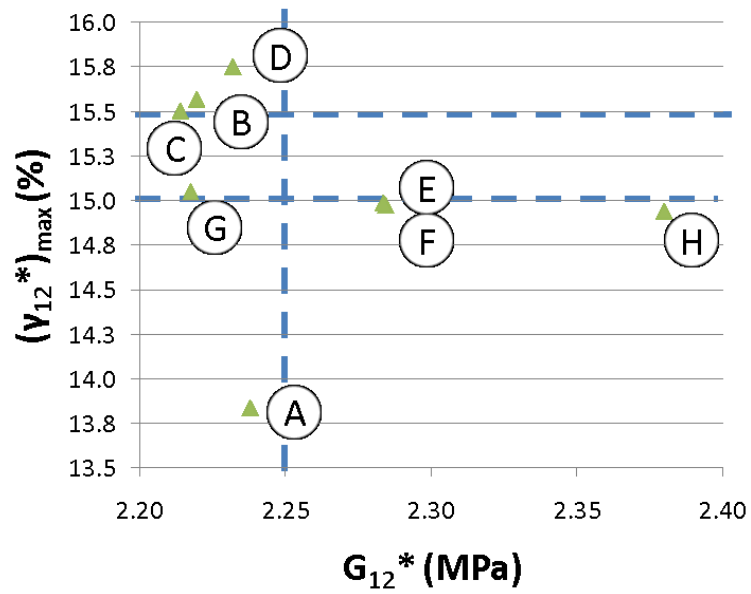
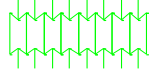


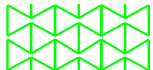



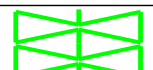


Figure 2.34: Resulting effective properties for targets: $G_{12}^*=2.25$ Mpa, $15\% < (\gamma_{12}^*)_{\max} < 15.5\%$.

Table 2.10: Structural geometry and effective properties for Figure 2.34.

| Target: $G_{12}^* = 2.25\text{Mpa}$ $\gamma_{\max}^* = 15 - 15.5\%$ | | thickness (mm) | N_v | N_h | R | d (mm) | G_{12}^* (Mpa) | G_{12}^* (Error) | γ_{\max}^* (%) | γ_{\max}^* (Error) |
|--|---|-------------------|-------|-------|-------|-----------|---------------------|-----------------------|--------------------------|------------------------------|
| A ₃ |  | 0.5 | 1 | 79 | 1.175 | 3.2 | 2.24 | -0.4% | 13.8 | -8.0% |
| B ₃ |  | 0.5 | 2 | 61 | 1.5 | 4.1 | 2.22 | -1.3% | 15.6 | 0.6% |
| C ₃ |  | 0.75 | 1 | 44 | 1.5 | 5.7 | 2.21 | -1.8% | 15.5 | 0.0% |
| D ₃ |  | 0.75 | 2 | 29 | 1.775 | 8.6 | 2.23 | -0.9% | 15.8 | 1.9% |
| E ₃ |  | 1 | 1 | 30 | 1.6 | 8.3 | 2.28 | 1.3% | 15.0 | 0.0% |
| F ₃ |  | 1 | 2 | 18 | 1.775 | 13.9 | 2.28 | 1.3% | 15.0 | 0.0% |
| G ₃ |  | 1.25 | 1 | 19 | 1.75 | 13.2 | 2.22 | -1.3% | 15.0 | 0.0% |
| H ₃ |  | 1.25 | 2 | 11 | 1.775 | 22.7 | 2.38 | 5.8% | 14.9 | -0.7% |

2.5.2 Honeycomb Design Algorithm Discussion

2.5.2.1 Design for Additional Properties

In the current form, the design algorithm is intended to be used as an exploratory tool to discover what structures may be suitable for a particular application. The purpose of using multiple structures having initial wall thicknesses and vertical cells is to provide multiple options which can be chosen based on additional criteria.

For example, in the design case shown in Figure 2.32 with target values of 4.25MPa for G_{12}^* , and at least 10% for $(\gamma_{12}^*)_{\max}$, seven of the eight structures successfully achieve the shear property requirements. If an additional criterion for this

material is to minimize weight, than the effective density of the structure can be used to choose amongst the structures.

The relative density describes the amount of volume occupied by the structure within the design space and is calculated using Equation 2.11, where ρ_s is the density of the constituent material. The relative densities for all of the structures in this design case are given in the final column of Table 2.11.

Equation 2.11:
$$\frac{\rho^*}{\rho_s} = \frac{t \left(\frac{h}{l} + 2 \right)}{2 \cos(\theta) \left(\frac{h}{l} + \sin^2(\theta) \right)}$$

Table 2.11: Data results from Figure 2.32

| # | t (mm) | N _v | N _{hf} | R | d _f (mm) | G ₁₂ * (MPa) | (τ ₁₂ *) _{max} (%) | ρ*/ρ _s |
|---|--------|----------------|-----------------|------|---------------------|-------------------------|--|-------------------|
| 1 | 0.5 | 1 | 81 | 0.95 | 3.09 | 4.23 | 9.29 | 0.23 |
| 2 | 0.5 | 2 | 62 | 1.20 | 4.03 | 4.25 | 10.49 | 0.31 |
| 3 | 0.75 | 1 | 48 | 1.25 | 5.21 | 4.20 | 10.73 | 0.32 |
| 4 | 0.75 | 2 | 31 | 1.45 | 8.06 | 4.15 | 11.22 | 0.39 |
| 5 | 1 | 1 | 31 | 1.30 | 8.06 | 4.30 | 10.12 | 0.34 |
| 6 | 1 | 2 | 21 | 1.50 | 11.90 | 4.26 | 11.17 | 0.45 |
| 7 | 1.25 | 1 | 20 | 1.43 | 12.50 | 4.14 | 10.41 | 0.36 |
| 8 | 1.25 | 2 | 14 | 1.60 | 17.86 | 4.27 | 11.78 | 0.51 |

From Table 2.11, structure two has the lowest relative density of 0.31 and is selected as the best candidate for the light weight cellular material. The geometric parameters and the resulting effective properties of the final design are shown in Table 2.12 and Figure 2.35 shows the structure sheared at 10%.

Table 2.12: Geometric parameters and effective properties of the final structure design.

| t (mm) | N_v | N_h | R | d (mm) | h (mm) | l (mm) | θ |
|---------------|-------------------------|-------------------------|------------|---------------|---------------|---------------|----------------------------|
| 0.5 | 2 | 62 | 1.2 | 4.03 | 3.81 | 2.11 | -17.5 |

| G_{12}^* (MPa) | $(\gamma_{12}^*)_{\max}$ (%) | ρ^*/ρ_s |
|------------------------------------|--|-----------------------------------|
| 4.25 | 10.49 | 0.31 |

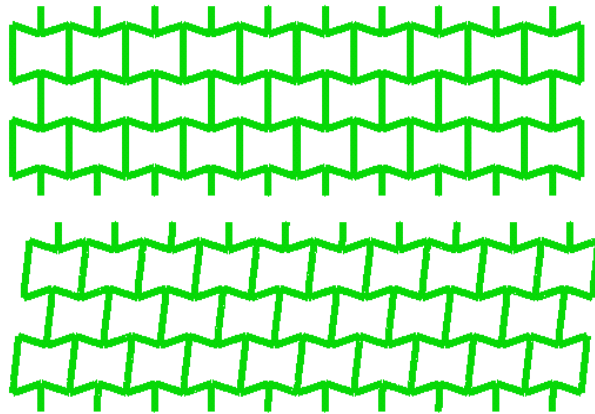


Figure 2.35: 10 unit cells of the final structure design sheared at 10%.

Another likely criterion for judging the structures is manufacturability. Manufacturability is a major concern in cellular structure development due to the intricacy of the structures and the small thicknesses of the thin walled sections. One advantage of the current design method is that the cell wall thickness, t , is an input to the algorithm and not a variable in the design process. As such, the wall thickness can be selected prior to design based on manufacturing limitations to determine if it is possible to achieve the target properties with the minimum thickness.

2.5.2.2 Target Property Error

The results from Figure 2.31 show that the honeycomb design algorithm can successfully produce many structures which closely match a desired set of shear properties for a range of design scenarios.

The resulting error for both target properties is caused by modifications to the parameter d in the second step of the design algorithm. In the first step of the algorithm, the horizontal separation, d , of the structure is held constant and the effective height, R , is modified so that the maximum effective shear strain, $(\gamma_{12}^*)_{max}$, is between the upper and lower bounds. At this point in the algorithm, all of the structures successfully achieve the target $(\gamma_{12}^*)_{max}$ range.

The basis for the design method used in the algorithm is that modifications to d have little effect on the maximum shear strain as indicated by Figure 2.11. However, for large changes to d in the second algorithm step, the final resulting maximum shear strain can drift significantly from the initial value found in step one. In the current form, the algorithm always sets the initial value of d_I to be half of the overall structure height, so $d_I=H/2$. One possible solution to reduce the error in $(\gamma_{12}^*)_{max}$ is to select the initial value for d in step one which is closer to the final value found in step two to reduce the amount of drift.

In the second step of the algorithm, the effective shear modulus is designed for by utilizing the linear relationship between the number of horizontal cells, N_h , and G_{12}^* to determine the final value of d . One constraint for the design method is that the overall

length of the structure, L , must be achieved, requiring N_h to be an integer. This causes some error to the resulting G_{12}^* value due to the discrete nature of N_h .

The source of the error in the algorithm results is ultimately due to the assumption used to develop the design method. The resulting design method may not produce exact properties; however, it is to be used as a conceptual design tool to produce many structures with approximate effective properties quickly and without the need for optimization.

2.6 HONEYCOMB DESIGN SUMMARY

A new system of parameterization was developed to increase the efficiency of honeycomb structure design for a target effective shear modulus and maximum effective shear strain simultaneously. With this system, a designer is able to easily normalize the design space and modify the structure so that the resulting properties change in a predictable way due to the parameter-property relationships. Additionally, the new system successfully decouples one of the design parameters and one of the target properties, simplifying the process of designing for two target properties. Based on the new parameterized system, a new design method was developed to design for the two effective properties simultaneously and an algorithm was created using this method to search for solutions using multiple topologies.

The algorithm was used to search for structures with an effective shear modulus between 4 and 4.5MPa able to reach an effective shear strain of at least 10%. Of the eight structures produced by the algorithm, seven were successful in satisfying the effective property requirements and the structure with the lowest relative density was

selected for the final design. The final structure design has an effective shear modulus, G_{12}^* , of 4.25MPa and maximum effective shear strain, $(\gamma_{12}^*)_{max}$, of 10.49% with a relative density of 0.31. In this case, the algorithm was successful in producing one structure which achieved the target properties with high precision. However, the primary objective of the method is to be used as a conceptual design tool. Any of the resulting structures can be selected based on additional criteria and then further refined to achieve the target property values to within acceptable level of error.

2.7 DESIGN APPROACH FOR DIFFERENT CELLULAR TOPOLOGIES

The underlying principal used in the development of the honeycomb design method is the assumption that the bending vertical members of the honeycomb structure are analogous to springs in parallel when a shear load is applied. This simplification of the design problem allows for two assumptions to be made about the general approach to design for the two target properties. The first assumption is that the maximum achievable strain is limited by the maximum allowable deflection in the effective spring members. The second assumption is that the shear modulus of the structure is dependent on the number of parallel spring elements over a given length of the structure. The basic two step approach to achieve both effective properties simultaneously is based on these assumptions, where the spring elements are first designed to achieve a desired strain, and then the number of spring elements is designed to produce the desired modulus.

The same design approach developed for honeycomb structures can also be used to design other cellular topologies to achieve target effective shear properties. The critical aspect is to identify the features in the structure which are the effective spring

members. For the hexagonal honeycomb topology, it was found that the effective spring members in the system are the vertical members, and the additional angled members serve primarily as structural support for the vertical spring members. As such, the design focus is on the geometry of the vertical members, and the angled members are considered to be secondary components required to complete the structure.

As an example, the bristle structure shear band (see Figure 2.36) is considered to show that the basic design approach is applicable to other cellular structures (10). For the simple bristle structure, all of the members are considered to be spring elements as there are no additional support members in the structure. The same design steps used for the honeycomb structures are used here for the bristle structure, though the geometric variables used in the design process will differ.

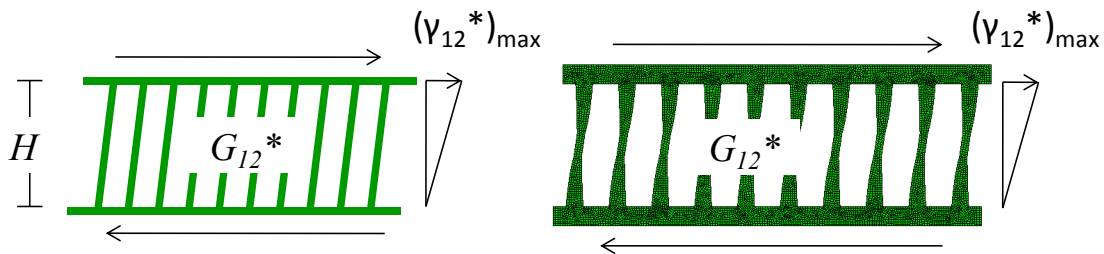


Figure 2.36: Straight Bristle structure shear band (left) and Tapered Bristle shear band (right).

In the bristle structure shear band, the lengths of the spring members are constrained by the overall height of the shear layer, H . As such, the spring member lengths cannot be used as a variable to achieve the target shear strain as was done in the honeycomb design method. With a constrained length, the remaining variable to achieve the desired strain is the bristle thickness, or in the case of a tapered bristle design, the

shape of the bristles. Once the geometry of the individual bristles is known, the separation between the bristles is used to produce the desired modulus.

The simplified geometry of the bristle structure also makes an analytical solution to the design more feasible, as all of the individual spring members are independent of each other. Recent work on the design of an aluminum tapered bristle shear band (2) has shown that an analytical model following the two step design process shown in Figure 2.37 can produce structures which approximate the desired shear properties effectively.

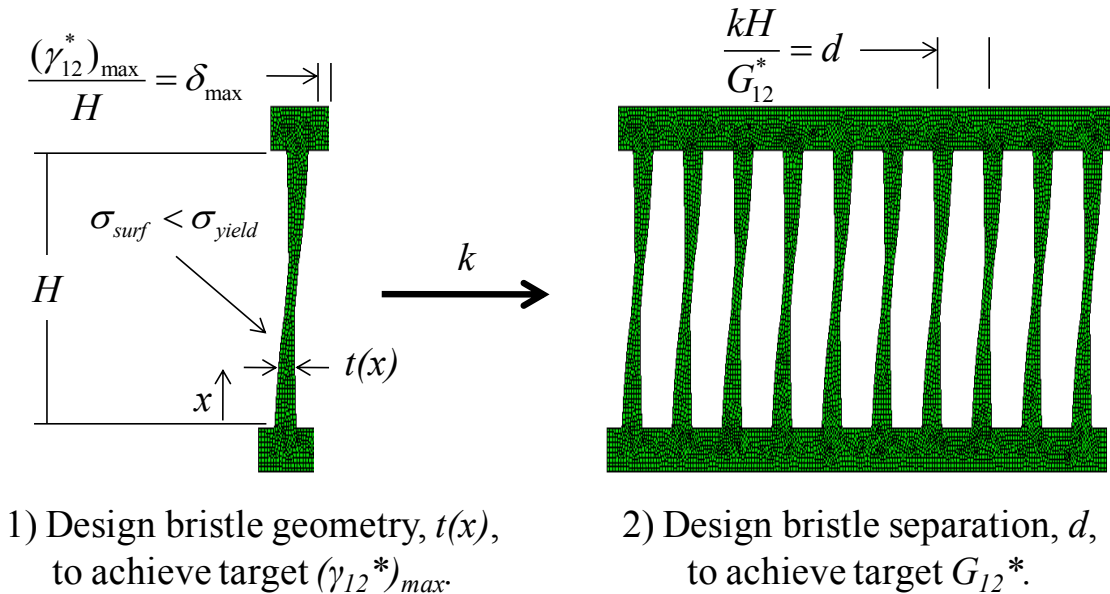


Figure 2.37: Two step design process for the tapered bristle shear band.

In the first design step in Figure 2.37, the thickness profile of the individual bristles is first determined analytically so that the maximum stress in the bristle is below the yield stress at the deflection required for $(\gamma_{12}^*)_{max}$. Based on the geometry, the bending stiffness, k , of the bristle is then used to calculate the required separation, d , between the bristles to produce the desired shear modulus, G_{12}^* , in design step two.

The analytical solution is used to design a shear band with a height of 38.1mm to achieve a target shear modulus of 2.5MPa, and a maximum material stress of 310MPa at a shear strain of 15%. The bristle profile is design to achieve this using 2014-T6 aluminum as the constituent material, with a modulus of elasticity of $E=72\text{GPa}$, and a yield stress of $\sigma_y=410\text{MPa}$ (40). In Figure 2.38 an Abaqus model of the resulting structure is given at a strain level of 0.7% and 15%, and a summary of the property results are given in Table 2.13.

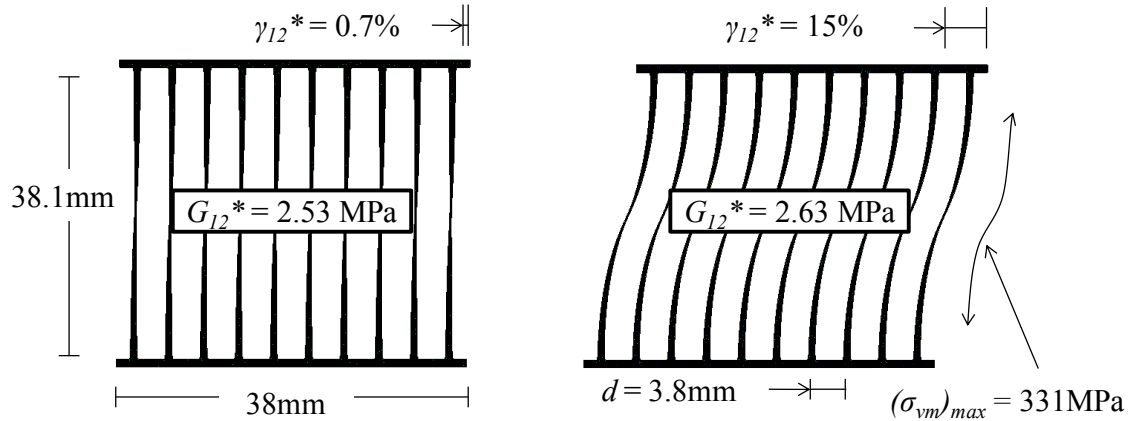


Figure 2.38: Tapered bristle structure resulting from the analytical design solution.

Table 2.13: Resulting properties of the tapered bristle structure designed using analytical solution.

| Property | Analytical | FEA | Error |
|--------------------------------------|------------|----------|-------|
| $(\sigma_{vm})_{max}$ (at 15% shear) | 310 MPa | 331 MPa | 6.80% |
| G_{12}^* (at 0.7% shear) | 2.5 MPa | 2.53 MPa | 1.20% |
| G_{12}^* (at 15% shear) | 2.5 MPa | 2.63 MPa | 4.80% |

The results from the analysis show that the resulting shear modulus has an error of 1.2% for small strains, however, due to the nonlinear deformation of the bristles, the error

increases as the strain increases. It also shows that the resulting stress in the bristles at maximum shear strain has an error of 6.8% of the target value; however, the maximum stress is still below the yield stress of the material.

As with the honeycomb design method, the analytical solution is intended to be used as an exploratory tool, to quickly and effectively produce structures which approximate the target effective properties, and higher accuracy can be achieved through further refinement. The example of the tapered bristle shear band design illustrates that the basic design approach developed for the honeycomb design method can also be used to develop design methods to achieve target shear properties for other structural topologies.

CHAPTER THREE: MORPHING SKIN CELLULAR STRUCTURE SYNTHESIS

The objective of the honeycomb design method discussed in Chapter Two is to design a cellular structure to achieve a single set of desired target properties. It is assumed that the target properties are known before hand, and the geometric parameters are designed and repeated in the structure to achieve the desired properties throughout the material. In this chapter, the objective is to achieve a desired morphing behavior using a cellular structure with varying properties. As such, the focus of the design process is shifted from achieving a single set of known properties, to achieving an unknown set of varying effective properties to produce a desired shape change.

The varying properties of the cellular structure discussed in this chapter are achieved by regulating the compliance of individual members in the structure. As such, the morphing skin design method is comparable to compliant mechanism synthesis methods which can also be used to achieve desired shape morphing characteristics.

3.1 COMPLIANT MECHANISMS

Compliant mechanisms are monolithic structures that use material deformation to achieve the desired mechanical characteristics. There are several benefits to using compliant mechanisms rather than rigid-body mechanisms (41). When used in place of rigid body mechanisms, they can improve production costs by requiring fewer parts and allowing for more cost effective manufacturing techniques such as injection molding, and improve performance by reducing the component weight and the affects of backlash found in mechanical joints (41).

In addition to the improvement of existing mechanisms, compliant mechanisms offer possibilities for the development of new shape morphing components. In recent years, researchers have worked to develop new components such as morphing antennae (42) and morphing airfoils (13; 43; 44; 9) (Figure 3.1) designed to morph to new shapes as conditions change to improve performance.

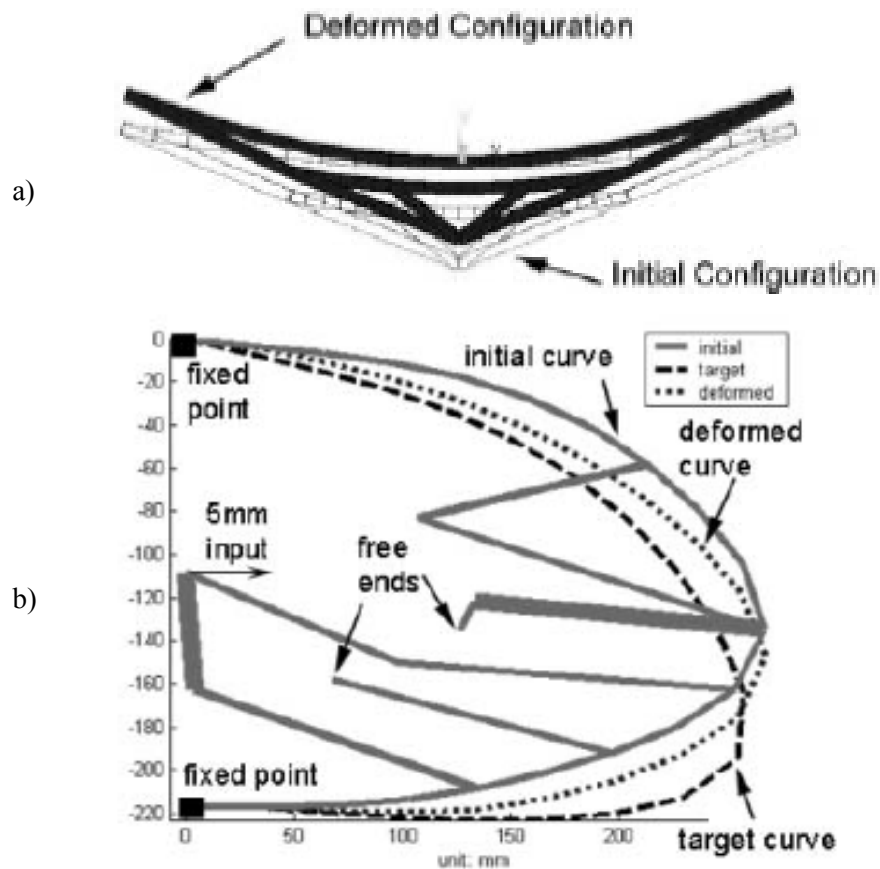


Figure 3.1: a) Shape morphing antennae (42) and b) morphing airfoil leading edge (13) using compliant mechanisms.

3.1.1 Compliant Mechanism Synthesis Methods

The objective of mechanism synthesis, be it rigid-body or compliant, is to establish relationships between forces and displacements at one or more points of a structure. Two established techniques for compliant mechanism synthesis can be found in literature, pseudo-rigid-body (Figure 3.2) and continuum structure optimization. Pseudo-rigid-body synthesis methods use rigid-body synthesis to design a mechanism, and modifications are made to account for the addition of compliant members (41; 45; 46). Continuum structure optimization methods utilize various optimization techniques, primarily genetic algorithms, for synthesis (47; 13; 42; 48; 44; 9).

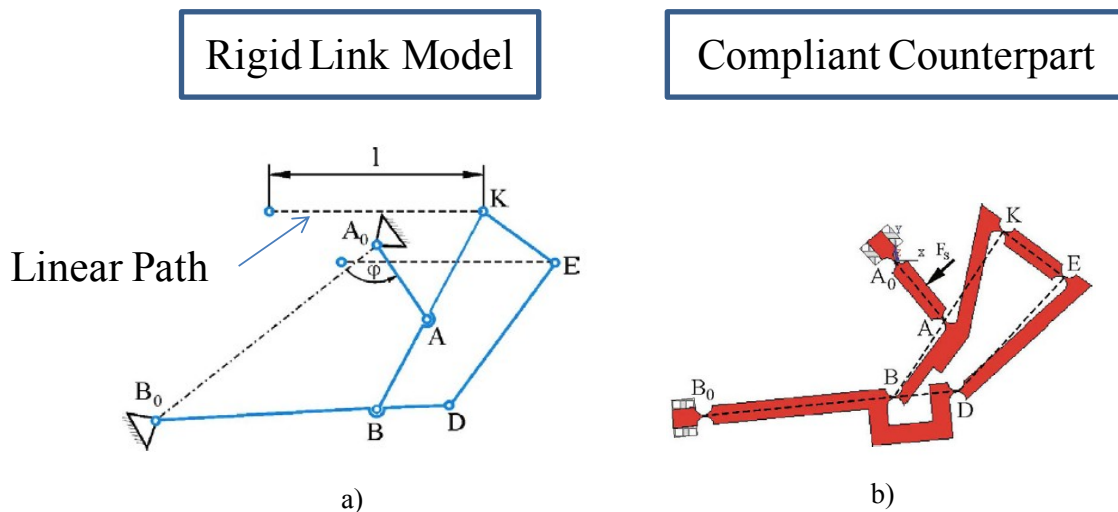


Figure 3.2: Pseudo-rigid-body model with a) a rigid link mechanism and b) the compliant mechanism counterpart. (46)

The pseudo-rigid-body model is a method that links rigid-body kinematics to compliant mechanism kinematics, simplifying the design process by allowing the more complex compliant members to be modeled as rigid members. In Figure 3.2 an example is given where the pseudo-rigid-body method is used to design a compliant structure

which produces a linear path at point K. The actual design and analysis is done using a rigid link model (Figure 3.2a) with modifications added to reflect the characteristics of compliant members, such as reactionary moments caused by flexible joints (Figure 3.2b) (41; 46). The strength of the pseudo-rigid-body model is that it allows for the compliant mechanism to be modeled and analyzed in a simplified manner. However, it can be difficult to capture all of the behaviors of a compliant mechanism in a rigid link model effectively (49). For instance, if a mechanism is loaded at the center of a cantilever beam segment, the response of the mechanism will be different than if it is loaded at the joint (41).

Continuum structure synthesis methods use optimization algorithms to design the structures. The methods used for shape morphing applications are genetic algorithms that simulate natural selection in nature. They operate by randomly generating designs which are analyzed to determine how well the design performs based on the design objective. This process repeats many times and at each step the “good” design features are encouraged in future runs until a successful structure is achieved. (47)

Within genetic algorithms, there are two methods to define the domain and to generate designs. The ground structure approach defines an initial structure consisting of many predefined beams as shown in Figure 3.3a. This approach uses size optimization to optimize the thicknesses of the individual beams to produce the desired performance (Figure 3.3b) (50; 45; 42; 44; 9). The homogenous approach does not begin with an initial structure but uses topology optimization which starts with a solid mesh domain, where each element of the mesh domain is considered to be variable which is either

present or not present. The design is achieved by selectively removing material elements until the desired functionality is met (44; 9; 51).

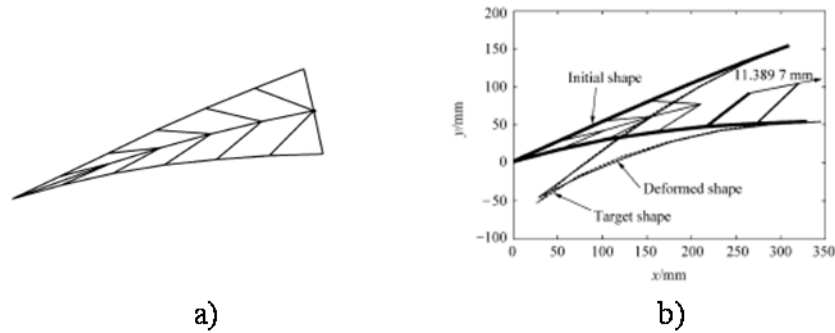


Figure 3.3: Ground structure approach with a) a predefined initial structure where the b) individual structure members are optimized to produce the desired results.³

The optimization objective function for compliant mechanisms is set up to minimize the difference in displacement of the actual structure and the desired displacement at the output points (9). Other objective functions can be included within the optimization depending on the design scenario, such as minimizing material volume for light weight structures (9). For shape morphing applications the objective of the optimization remains the same, except that multiple control points must be considered simultaneously (42).

Optimization methods are computationally expensive due to the finite element analysis involved and the number of iterations that must be run to reach a solution. When more output points are added the problem becomes more complex, requiring more

³ (43)

iterations and increasing the computational expense. This results in a tradeoff between the precision of the results and the computational time of the analysis (42; 13; 44; 9). There are also issues with these methods that have yet to be resolved which can cause the resulting designs to be infeasible, such as point flexures generated by topology optimization (47).

3.2 DIRECT DISPLACEMENT SYNTHESIS

The direct displacement synthesis method developed in this thesis is comparable to the ground structure optimization method discussed in the previous section. However, it differs greatly in the approach taken to solve for the unknown variables in the system. Both methods begin with a predefined structure and the objective of the synthesis is to design the individual structure members to produce the desired result. The ground structure approach uses genetic algorithms to iteratively design the members, whereas the direct displacement method uses data from a single analysis to design the individual members analytically.

The direct displacement approach was first developed to increase the efficiency of building seismic design. To reduce the amount of damage incurred during a seismic event, the building stiffness must be designed to be flexible, yet stiff enough to permit limited lateral displacement to prevent high strains in the structure (52). Other methods used for building design begin with an initial building stiffness which is then analyzed to determine whether it satisfies the displacement constraints. If not satisfied, the initial stiffness is then revised and reanalyzed. In direct displacement design, the allowable lateral displacements are determined first along with the equivalent lateral forces present

during an earthquake scenario. The effective stiffness of the building is then directly calculated to produce the desired displacement when the forces are applied (52) and the structural members of the building can then be designed directly to produce the required stiffness of the building (52; 53). By using this approach, direct displacement design can increase the efficiency of seismic design by reducing the need for iterative processes (52).

Building seismic design differs considerably from the shape morphing applications discussed in this thesis; however, there are several similarities which make these processes applicable to certain shape morphing compliant mechanisms. Buildings are constructed from multiple floors having different effective stiffnesses which, when combined, determine how the building will deform when lateral loads are present. Similarly, compliant mechanisms are formed from many members with different stiffnesses which determine the final shape of the structure when loaded. In this thesis, the direct displacement synthesis method developed for the design of the stiffness variables in a building is modified for the design of individual elements of a compliant mechanism.

3.2.1 Direct Displacement Design Approach

The direct displacement method differs from the previously discussed synthesis methods in the way the unknown variables in the system are designed. In Figure 3.4, the processes used for both iterative and direct displacement synthesis are compared. The objective for both processes is to determine the unknown stiffness variables which will produce a desired outcome. The iterative process begins the design by first assigning

stiffness values, and then analyzing the structure under specified loading conditions to determine how well the structure performs with the assigned stiffnesses. If the resulting displacements in the structure do not meet the requirements, the stiffnesses are reassigned and the process repeats until the requirements are met.

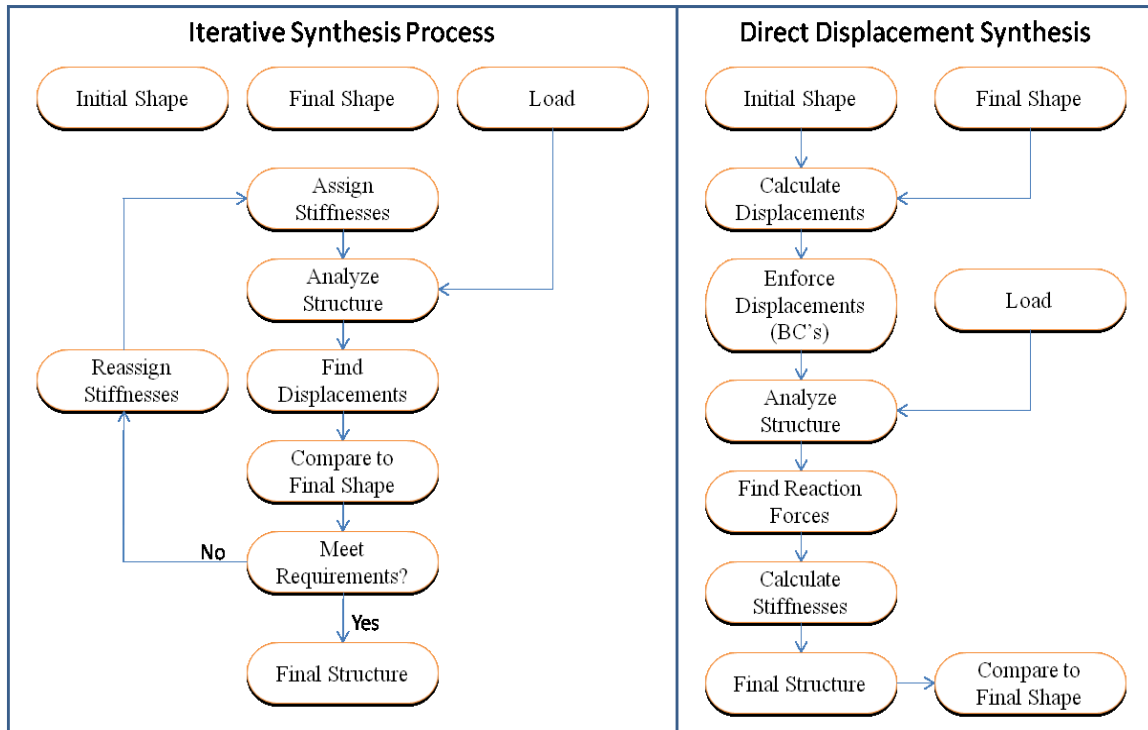


Figure 3.4: Comparison of Iterative and Direct Displacement flow charts for finding unknown stiffness values.

In direct displacement synthesis, some of the steps used in the iterative process are inverted so that the unknown variables can be calculated directly without the need for iteration. The direct displacement method begins by first calculating the required displacements of different elements in the structure and enforces those displacements on the structure using boundary conditions. A single analysis is then run where the structure is constrained to the desired final shape and the load is applied. This analysis provides

the reaction forces for each element of the structure, and this, along with the known displacement data, allows for the individual stiffnesses to be calculated directly.

The direct displacement method can be demonstrated by a simple spring series example in which the stiffnesses of three springs in series must be designed to produce specific displacements when a load is applied. In Figure 3.5.A an initially unloaded system of springs is shown having initial spring locations of H_i , and each spring has a total relative height of h_i . When a load, F , is applied to the system, the springs must deform so that the final spring locations are at H'_i , as shown in Figure 3.5.B. In the direct displacement method, the spring stiffnesses required to produce the desired deflections are designed by first analyzing the system in the deformed state (Figure 3.5B). During the analysis, the desired force, F , is applied to the system and the desired deflections from H to H' are enforced using boundary conditions.

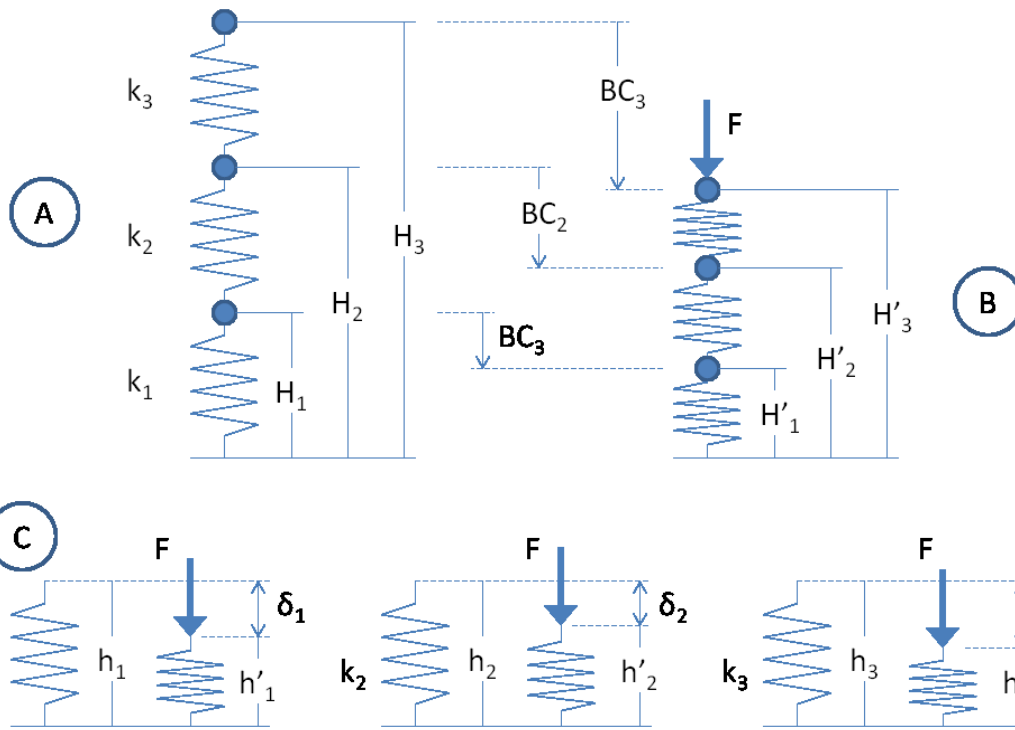


Figure 3.5: Direct Displacement used to solve spring stiffnesses for springs in series.

The results from the analysis provide the reaction forces for each spring member, where in this simple example, all springs will have a reaction force of F . The reaction force data along with the desired relative deflections of each spring, δ_i , are then combined to calculate the spring stiffnesses individually as shown in Figure 3.5.C, using the equation: $k_i = \frac{F}{\delta_i}$. In essence, the direct displacement method is able to achieve the design by discretizing the system as a whole into individual design problems for each variable.

3.3 MORPHING SKIN DESIGN USING DIRECT DISPLACEMENT

In the previous section the direct displacement method is discussed as a means to design individual elements of a spring series system to achieve desired displacements for

different spring sections. The same concept is used here for the design of morphing skins, where a skin structure having many springs in series is designed to achieve a desired shape.

The geometric framework for the morphing skin, shown in Figure 3.6, is a skin having rigid triangular truss segments which are connected along the skin surface using compliant hinge members to allow relative rotation between the segments. Compliant spring members are then placed between each truss segment to control the force-displacement relationship between the top points of the trusses. As the truss segments are hinged about the skin surface, these force-displacement relationships translate to a bending stiffness for each segment of the skin.

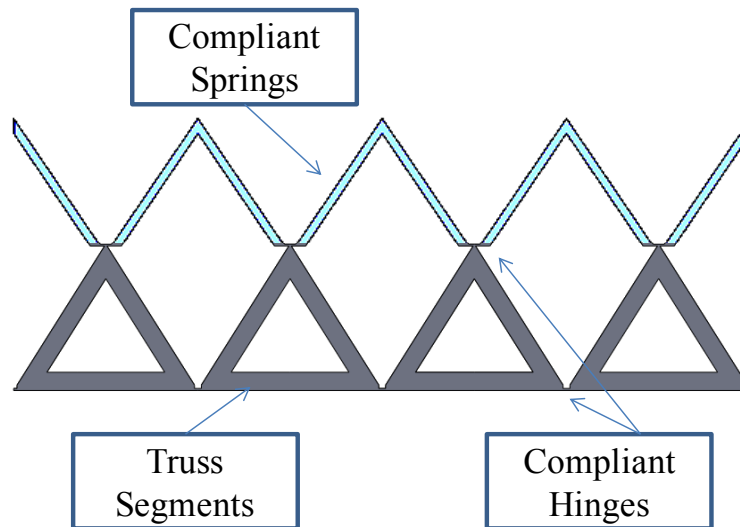


Figure 3.6: Base structure for the morphing skin design method.

For morphing skin design, the direct displacement method combines some aspects of the pseudo-rigid-body model and the ground structure approach, where a base structure is established before synthesis and the structural components are attached using

compliant hinges. As in the pseudo-rigid-body model, the base skin structure is formed from many rigid segments attached using the compliant hinges, causing the skin to behave more as a kinematic system, where the skin segment links can rotate relative to each other. As with the ground structure approach, the topology of the structure is known before synthesis occurs; however, the direct displacement method differs greatly in how the unknown variables in the system, the spring stiffnesses, are designed for.

The objective in morphing skin design is to understand how the segment links along the skin must interact with each other to produce a desired shape change and to design the structure to facilitate those relationships. In the simple example of springs in series, the relationships required are the relative displacements and forces experienced between the springs. Using this information, it is possible then to specify the spring stiffnesses so that the desired displacements occur when the load is applied. For the morphing skin structure, the required information is the relative angular displacement between the segments and the moments experienced by each segment. This is achieved by applying the load and analyzing the structure when it is in the desired morphed shape using boundary conditions to find the reaction moments. This information can then be used to design the individual spring components to achieve the same result when the boundary conditions are removed.

3.3.1 Morphing Skin Design Concept

Direct displacement is used to determine the spring thicknesses required in the system to facilitate a specific shape change when acted on by an external force. If the

input forces used to cause the shape change are known, then the required stiffness of each segment can be designed directly so that the angular displacement of each segment is equal to the rotation required for the desired shape change. That is, when a force is applied to the skin, each segment will experience different moment reactions as a result of the load. By controlling the bending stiffness from segment to segment based on these moments, it is possible then to design the spring stiffnesses so that each segment responds with the desired rotational deflection when the load is applied. Before the spring thicknesses can be designed, information is required about the desired morphing behavior of the skin and how the skin segments must interact with each other.

For a skin to morph from an initial shape to a final desired shape, each segment along the skin must rotate to form the new profile. In Figure 3.7, the concept used to achieve shape morphing via segment rotation is illustrated. In order to morph from the initial straight line to the morphed curve, each segment must rotate by a certain angle, $\delta\theta_i$. These segment rotations are analogous to the total displacements of the spring sections in the spring series example. The total rotation angles, $\delta\theta_i$, are required to understand the overall morphing behavior of the skin, however, relative angle displacements are also required to understand how the individual segments interact with each other when morphed. The relative segment rotations, $\delta\theta_i - \delta\theta_{i-1}$, are the changes in angle experienced by each segment relative to the adjacent segment when morphed. The relative segment rotations are used to break down the design of the whole structure into individual components and are analogous to the relative displacements in the spring series example.

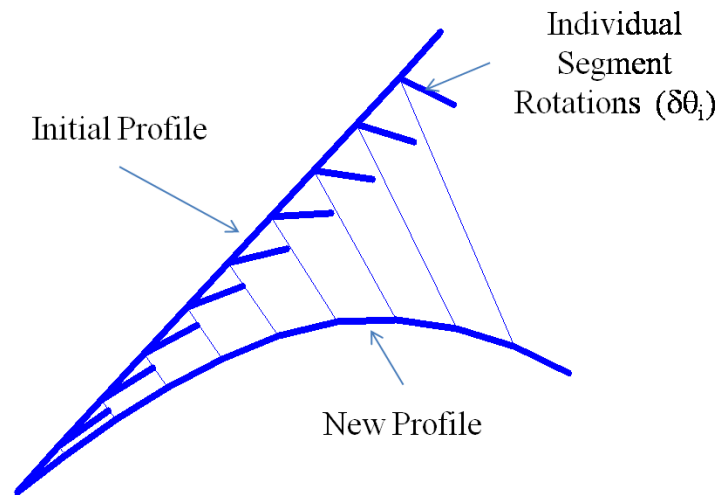


Figure 3.7: Skin morphing through segment rotation

The principal used to control morphing behavior in the direct displacement method is that the force displacement/rotation relationship between two adjacent segments along the skin will determine how the two segments displace relative to each other when a load is applied. Consider a skin broken down to 2 segments, where segment 1 is to be stationary and segment 2 is to rotate by a specified amount when a downward force is applied to the end as shown in Figure 3.8. When the segment is rotated it results in a relative displacement between the two top points of the segment trusses. If a free rotating linear spring is added to connect these two points, then the force-displacement relationship of the spring can be converted to a moment-rotation relationship for segment 2.

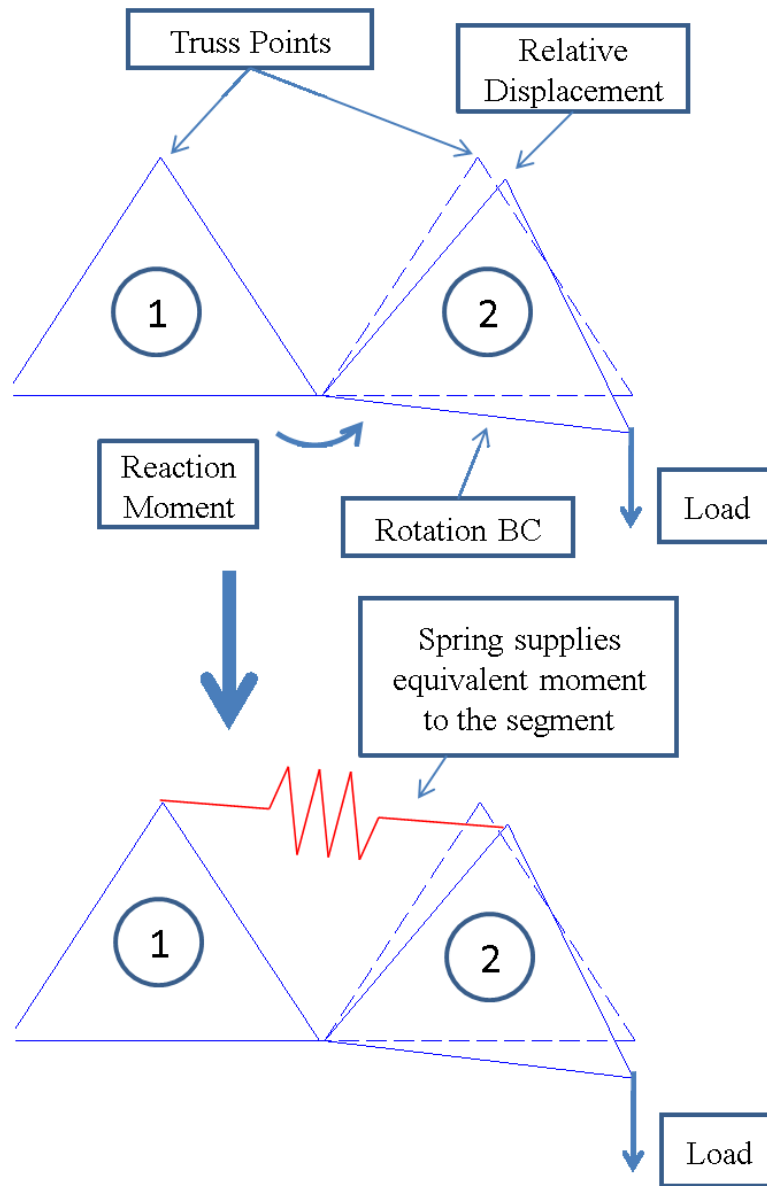


Figure 3.8: Principle used in the direct displacement method.

Direct displacement is used to determine how stiff the linear spring must be to produce the desired rotation in the segment when the load is applied. Before the linear springs are added to the structure a finite element analysis is performed in which rotation boundary conditions are applied to the two segments and the downward load is applied to the end as shown in Figure 3.8. The rotation boundary conditions constrain the structure

to the shape that is desired for the given load, making it possible to determine what reaction moments must be present in the structure to maintain this shape when the load is applied. To replicate the same shape change when the rotation boundary conditions are removed, the linear spring connecting the two truss points must supply a moment to segment 2 equal to that of the removed boundary condition. The stiffness of the spring can then be calculated by converting the moment-rotation relationship to a force-displacement relationship between the two truss points.

As more segments are added to the structure the complexity of the shape morphing behavior increases, but the same principle is used for synthesis. During the direct displacement analysis, rotation boundary conditions are applied to all segments and the results will supply the reaction moments for all segment. This system of reaction moments can then be converted to a system of force-displacement relationships between the segments and the stiffness of each spring member can be designed individually.

3.4 MORPHING SKIN DESIGN METHOD

A morphing skin design method using direct displacement is developed to design a skin structure which will morph from an initial shape to a final desired shape when acted on by a specific load. The purpose of this design method is to provide a systematic process for the design of morphing skins. The general operation of the design method is summarized in Figure 3.9 and involves five major steps; 1) develop structural geometry, 2) quantify morphing characteristics, 3) reaction moment analysis, 4) spring synthesis, and 5) error analysis. An overview of these steps is discussed in the following sections and further detail is provided the morphing skin design algorithm section.

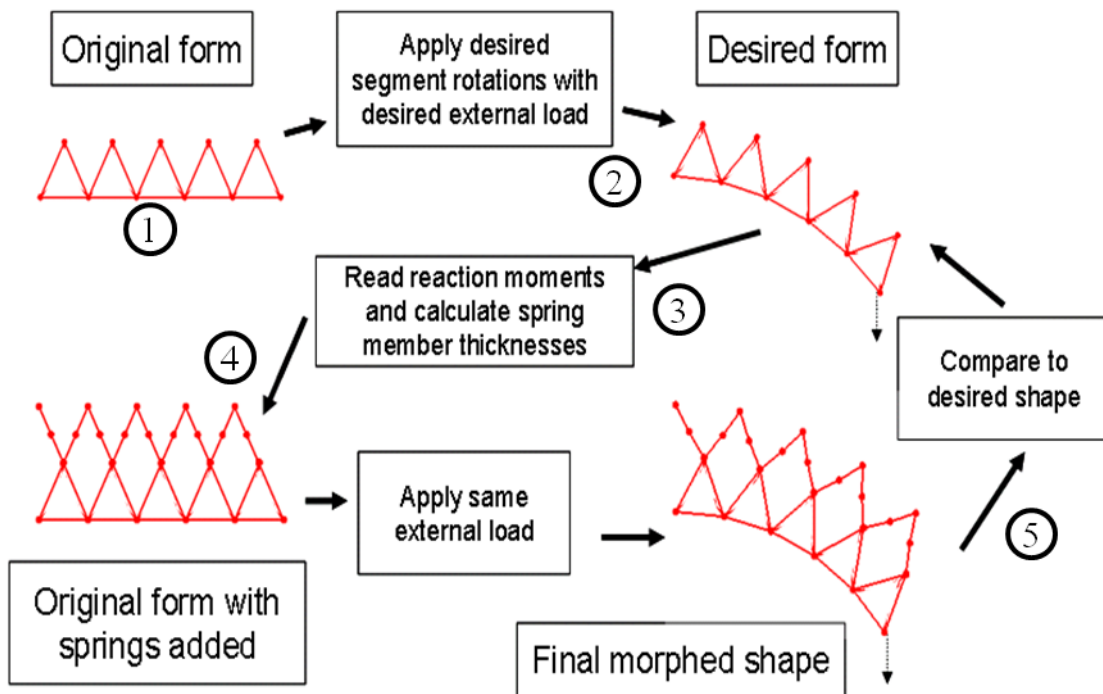


Figure 3.9: Summary of the direct displacement synthesis method.

3.4.1 Structural Development

The first step in the design method is to establish the geometry of the skin structure including the segments and segment trusses, but with no springs. The geometry and the behavior of the morphing triangular sections are required to understand the interactions necessary to achieve the desired morphing behavior. At this point, the profiles being considered for both the initial shape and the morphed shape must be discretized to form the segments, where each segment has an associated angle. Both discretized profiles must have an equal number of equal length segments so that each segment in the initial profile corresponds to the same segment in the morphed profile.

Once the profiles are discretized, the next step is to create the geometry of the triangular truss. The truss shapes are added to the structure at this point because the separation between the top points of the trusses is required to establish the force/displacement relationships used in later steps. All of the truss sections in the structure have the same geometry, except that they are in different locations and orientations based on the angle and location of the segments.

The result of this step is two initial segmented structures which can be used in later steps to quantify the desired morphing behavior.

3.4.2 Morphing Characteristics

The morphing characteristics used in this design method are based on the rotation angles and truss deflections as the structure morphs from one shape to another. The initial segmented structures developed in step 1 are now analyzed to quantify these values. The rotation angles are found by calculating the difference between corresponding segment angles in both structures. That is, the rotation angle for the first segment is the angle difference between the first segment of the initial profile and the first segment in the morphed profile.

To calculate the truss point deflections, the relative rotation between two adjacent truss points is used along with the geometry of the truss sections. The location of the truss points is known relative to the positions of two adjacent segments, and the rotation of one segment relative to the adjacent segment will cause the truss points of those two segments to displace relative to each other. The truss deflections are found by calculating

the difference in separation between two truss points from the initial shape to the morphed shape.

3.4.3 Reaction Moment Analysis

The reaction moment analysis step is the critical step in the design process that allows for the spring stiffnesses to be designed for directly without the use of optimization or iterative processes. The goal of this step is to find the reaction moments of each skin segment when it is in the morphed shape and the load is applied which can later be used to calculate the required spring stiffnesses.

This is done by first placing the initial non-morphed structure into a finite element analysis program. Within the FEA program, the segment rotations found in the previous step are added to each segment in the form of rotational boundary conditions. At this point, the structure is fully constrained in the desired morphed shape and should resemble the initial morphed shape structure developed in the previous step. The final input into the analysis program is the desired load before the analysis is run. The resulting output of this analysis step is the reaction moments for each segment along the skin.

The purpose of adding the non-morphed initial structure into the program and changing its shape using boundary conditions, rather than simply adding a fully constrained morphed initial structure, is that the resulting reaction moments will include the effects of the compliant hinges. As the segments rotate relative to each other, the use of compliant hinges will result in additional moments due to material deformation in the hinge. By including the hinge deformation in the analysis, the reaction moments output

from the analysis include the additional moments caused by the hinge sections and further analysis is not required to account for the compliant hinge affects.

In the current stage of this research, the only structures being considered are simple open ended skin structures which act similarly to a cantilever beam. For these simple cases it would be possible to directly calculate the reaction moments without the use of finite element analysis by performing a simple analysis on the initial morphed structure. However, in future research, this method will be expanded to include more complex morphing behavior where a simple analysis will not be possible to find the reaction moments and finite element analysis will be required. For this reason, FEA is included in the design method.

3.4.4 Spring Synthesis

In the spring synthesis step of the design process, the information collected in previous steps on the structural geometry, morphing characteristics, and reaction moments are combined to calculate the required stiffness of each spring section. The objective of this step is to convert the moment/rotation relationship to a force displacement relationship for each spring section as is discussed previously in Figure 3.8.

At this point, three of the values are known, where the segment rotation is the relative segment rotation found in step 1, the moment is the reaction moment for the segment found in step 3, and the displacement is the relative truss displacement found in step 1. The only remaining value is the force required at the truss point. The required force is calculated as the force at the truss point which will supply a moment equal to the

reaction moment. There are several geometry considerations in the calculation of the required force concerning the location of the truss point and the direction of the force relative to the segment which will be discussed further in the morphing skin design algorithm section. There are also some considerations to account for the affect of the spring force on the adjacent segment which will also be discussed further in the algorithm section.

Once the required force is known, it is combined with the truss deflection to find the required stiffness. At this stage in the research, it is assumed that the shape of the spring sections is fixed and that the only variable left to modify spring stiffness is the spring thickness. The thicknesses of the spring sections are calculated so that the spring elements, which are modeled as beams, supply the required force when deflected by the distance specified by the truss deflection. Further details on these calculations are provided in the algorithm section.

The result of this design step is a series of spring thicknesses which can be added to the initial structure and will produce the desired morphed shape when the load is applied.

3.4.5 Error Analysis

The final step in the design method is to check the accuracy of the resulting design. The initial non-morphed structure within the FEA program is modified to include the spring elements with their corresponding thicknesses. A second FEA analysis is run in which the same load is applied and the rotation boundary conditions are removed. The

output from this analysis is the resulting position of each segment of the structure. The position of each segment is coordinates of the end point of the segment furthest from the base of the structure. The error in the design is calculated as the error between the resulting segment positions and the desired segment positions defined by the initial morphed structure and the total absolute distance traveled by each segment. Further details of the error calculation are provided in the algorithm section.

3.4.6 Morphing Skin Limitations

The morphing skin design method is useful for designing shape morphing skins only if the rotations required to morph from the original shape to the desired shape agree with the moment directions caused by the load. That is, if the skin is designed as a cantilever beam with a downward load on the end, all segment rotations must rotate in the same direction as the applied force to prevent a negative spring constant value. Additionally, at this point in the research, the focus is primarily on the synthesis procedures, and issues such as material stress limitations are not yet considered.

Future work on this topic will address material stress limitations and the used of additional load cases for the skin including multiple force loads and pressure loads. For this thesis, these load scenarios are deemed out of scope.

3.5 MORPHING SKIN DESIGN ALGORITHM

A design algorithm is developed to design morphing skins which morph from an initial to a final desired shape when a load is applied. The morphing skin algorithm is similar to the honeycomb design algorithm in that it is constructed using Matlab and uses

Abaqus for finite element analysis. The major differences between the two programs is that the morphing skin algorithm does not require an iterative process and it uses a Python script to communicate with Abaqus rather than an Abaqus input file.

The objectives of the morphing skin design algorithm are to first construct the topology of the morphing skin structure based on input parameters, and then to design the spring elements to achieve the desired morphing characteristics. Within the algorithm, the steps described in the morphing skin design method are automated so that the user must only specify the input parameters and the algorithm will output the structure design and the associated error.

The design algorithm, which is summarized in the flow chart in Figure 3.10, has six essential steps; 1) the initial and morphed skin shapes and several structural parameters are input, 2) the base skin structure is formed for both shapes based on the inputs, 3) pre-analysis calculations occur to quantify the differences between the two shapes in terms of segment rotation and truss point deflection, 4) an initial FEA analysis is run including the desired load and rotation BC's to find reaction moments, 5) the spring thicknesses are designed using the reaction moments and, 6) the spring members are added to the base structure and a final FEA analysis is run to test the results.

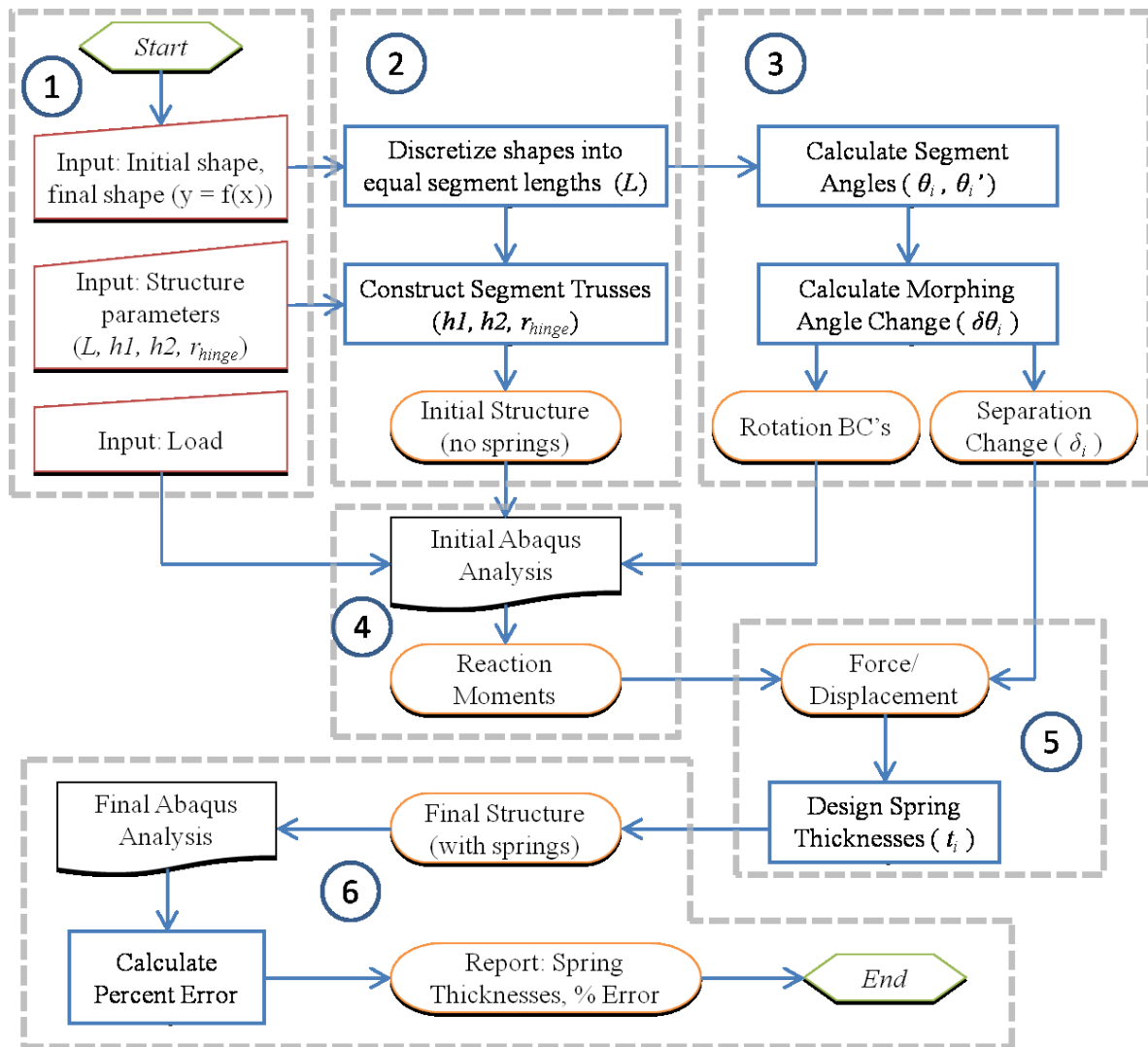


Figure 3.10: Morphing skin design algorithm flow chart

3.5.1 Step 1: Morphing Skin Input Parameters

The input parameters for the morphing skin algorithm, shown in Figure 3.11, are used to specify the desired characteristics of the skin structure and the morphing behavior.

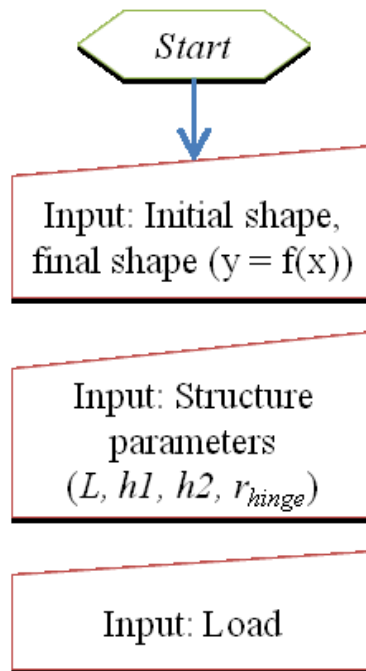


Figure 3.11: Algorithm flow chart inputs.

The algorithm is set up by first indicating the initial shape of the skin, the final shape of the skin, and the desired load to be applied at the end to obtain the morphed shape. The shapes of the skin are input as algebraic expressions so that the shapes are a function, $y=F(x)$ as shown in Figure 3.12. The input load is a downward global force that is applied to the end of the skin.

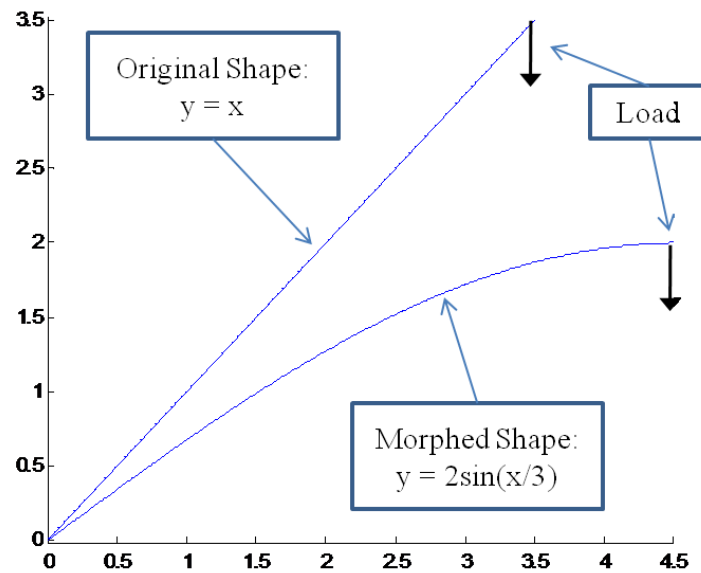


Figure 3.12: Algorithm shape and load inputs.

The program also takes several geometric options for the structure that are shown in Figure 3.13. These input variables are for the number of segments used, the length of the segments, L , the material properties, the relative lengths of the compliant hinges connecting the segments, r_{hinge} , the compliant hinge thickness, the relative height of the segment trusses, h_1 , and the relative height of the spring members, h_2 .

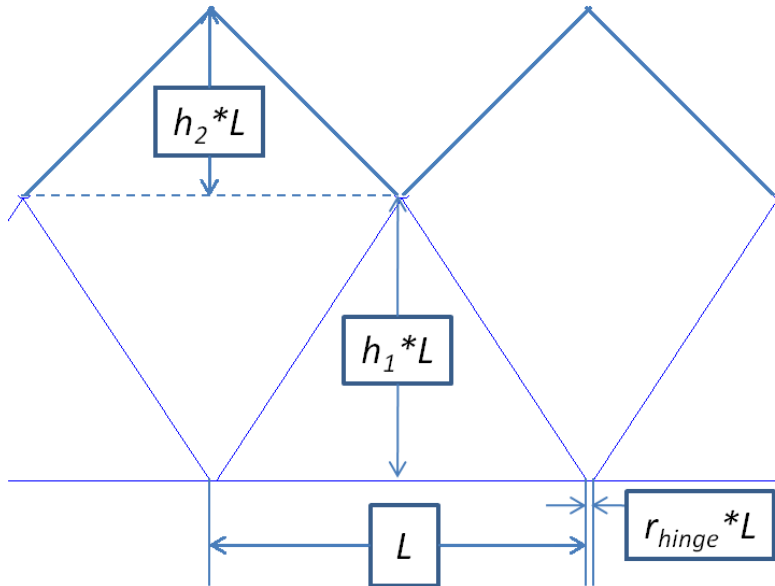


Figure 3.13: Geometric features for the truss elements.

The focus of the design method in its current form is to design only the spring elements of a structure based on the specified geometric inputs to achieve the desired shape change. In the current stage of development, the geometric properties of the rest of the structure, such as the length and thickness of the hinge members, are not considered to be limited in terms of manufacturability and stress failure. Further development of the design method to ensure manufacturability and flexure stress limitations is reserved for future work.

3.5.2 Step 2: Base Skin Structure

In this step of the algorithm, the initial structure is developed based on the input parameters and the desired shapes following the steps in Figure 3.14.

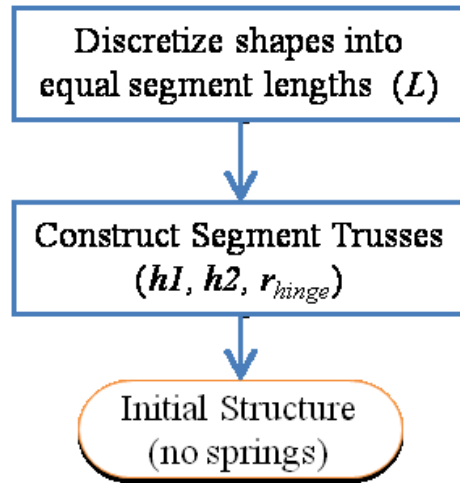


Figure 3.14: Algorithm flow chart development of the skin structures

The two shapes which are input in algebraic form are first discretized into an equal number of equal length segments. This is done by using the *fzero* command in Matlab to find points along the input curves which have absolute separation lengths of L . The process begins at the origin of the curve and a second point along the curve is found which has an absolute distance of L from the first point. Once the second point is found, the process repeats using the second point in the first step as the new first point until the total number of segments specified is reached. Equation 3.1 shows how the *fzero* command is used to find the x -location along the curve with an absolute distance L from the initial point, where $F(x)$ is the curve equation. The limits for the *fzero* command are set to $[x \ x+L]$.

$$\text{Equation 3.1: } x_2 = fzero \left(((x_1 - x_2)^2 + (f(x_1) - f(x_2))^2)^{\frac{1}{2}} - L \right)$$

For each calculated segment, the angle is recorded and the results are two series of segment angles and positions which form the profiles specified by the input shapes as shown in Figure 3.15.

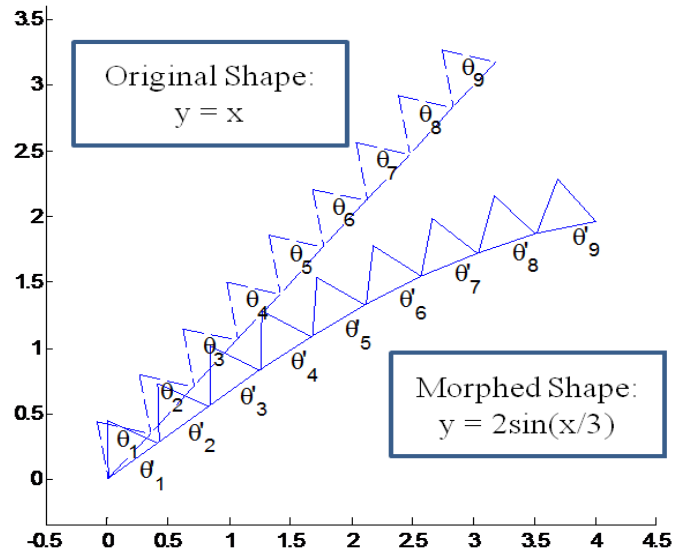


Figure 3.15: Development of structure segments in terms of segment angle.

The additional input parameters concerning the dimensions of the truss sections can then be applied to each individual segment as shown in Figure 3.13. The geometry of the truss sections is the same for each segment and is determined by the input parameters, L , H_I and r_{hinge} . The truss sections are attached to the segments at two points; the segment end point furthest from the base of the profile, and a distance $L * r_{hinge}$ from the end point nearest to the base. The truss point, which is the vertex of the triangular section, is located at the midpoint of the two truss connection locations and at a distance of $L * h_I$ from the segment.

3.5.3 Step 3: Pre-Analysis Calculations

At this point, the geometry of both profile structures is established and can be used to quantify the differences between the two shapes following the steps in Figure 3.16.

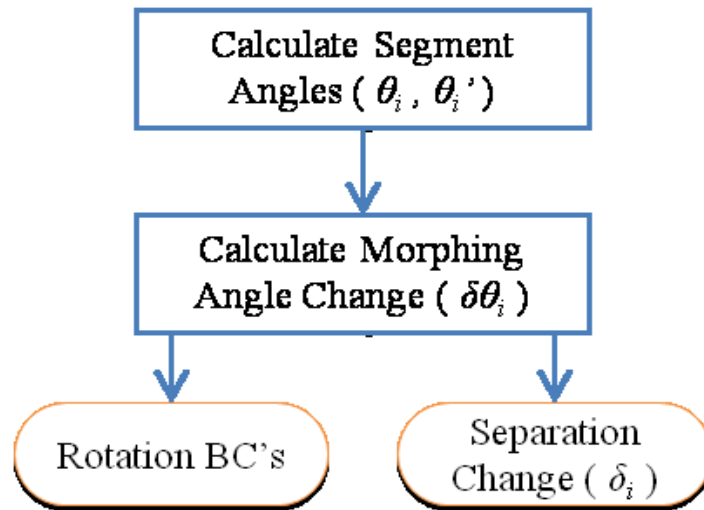


Figure 3.16: Algorithm flow chart steps used to quantify the morphing behavior.

The differences between the two structures are quantified in two ways; by the difference in angle of the initial structure segments and the corresponding final structure segments (see Figure 3.7), and the difference in separation of two adjacent segment truss points as the structure morphs from one shape to another (see $d+\delta$ in Figure 3.17).

The difference in angle between the two shapes is used to determine how each segment must be rotated to achieve the desired morphing behavior. It is found as the difference between corresponding segment angles in both structures using Equation 3.2, and as shown in Figure 3.17.

Equation 3.2:
$$\delta\theta_i = \theta'_i - \theta_i$$

The truss deflections are calculated using Equation 3.3 to determine the change in separation, δ , between two adjacent truss points when the skin is morphed as shown in Figure 3.17.

Equation 3.3:
$$\delta = \|TP'_2 - TP'_1\| - \|TP_2 - TP_1\|$$

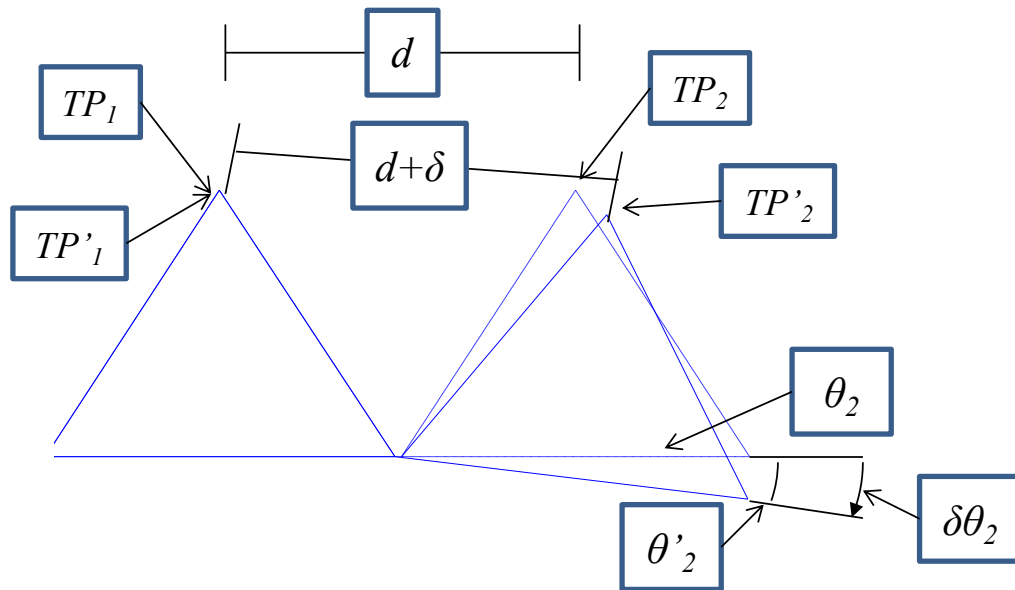


Figure 3.17: Segment angle rotations and truss displacements.

The rotation angles are used in the initial FEA analysis in the form of rotation boundary conditions, and the truss deflection data is stored for later use when designing the spring thicknesses.

3.5.4 Step 4: Initial Finite Element Analysis

In the initial finite element analysis, the original shape structure is analyzed to find the reaction moments in each segment when the desired load is applied and the structure is morphed to the final shape. The algorithm finds the required reaction

moments by combining the information on the structure geometry, load and morphing characteristics, as shown in Figure 3.18, to form a model which can be run in Abaqus for analysis

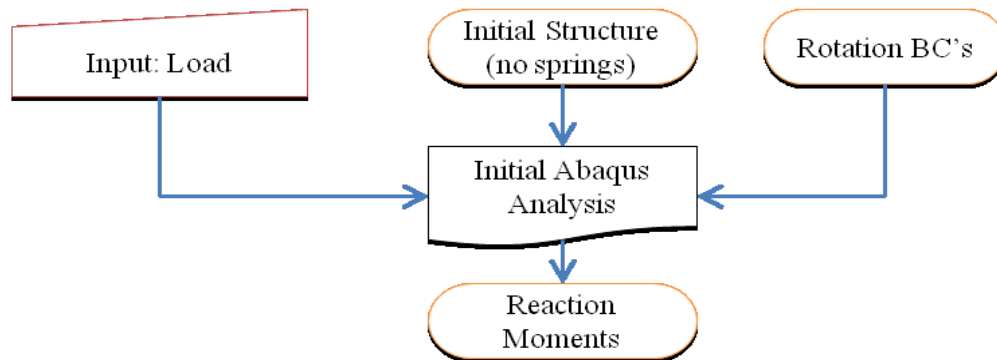


Figure 3.18: Algorithm inputs and outputs for the initial analysis step.

The analysis model applies two sets of boundary conditions to the structure; a fully constrained boundary condition is applied at the base of the structure, and rotation boundary conditions, $\delta\theta_i$, are applied to each segment. The desired downward load is also applied to the end of the structure. After the analysis, the reaction moments for each segment are recorded for use in the synthesis process.

The algorithm runs the analysis job by creating a python script containing the structure geometry, material properties, loading conditions and boundary conditions. The python script is then submitted to Abaqus and the resulting reaction moments are extracted from the results. The analysis job created by the python script and the results of the analysis are shown in Abaqus in Figure 3.19.

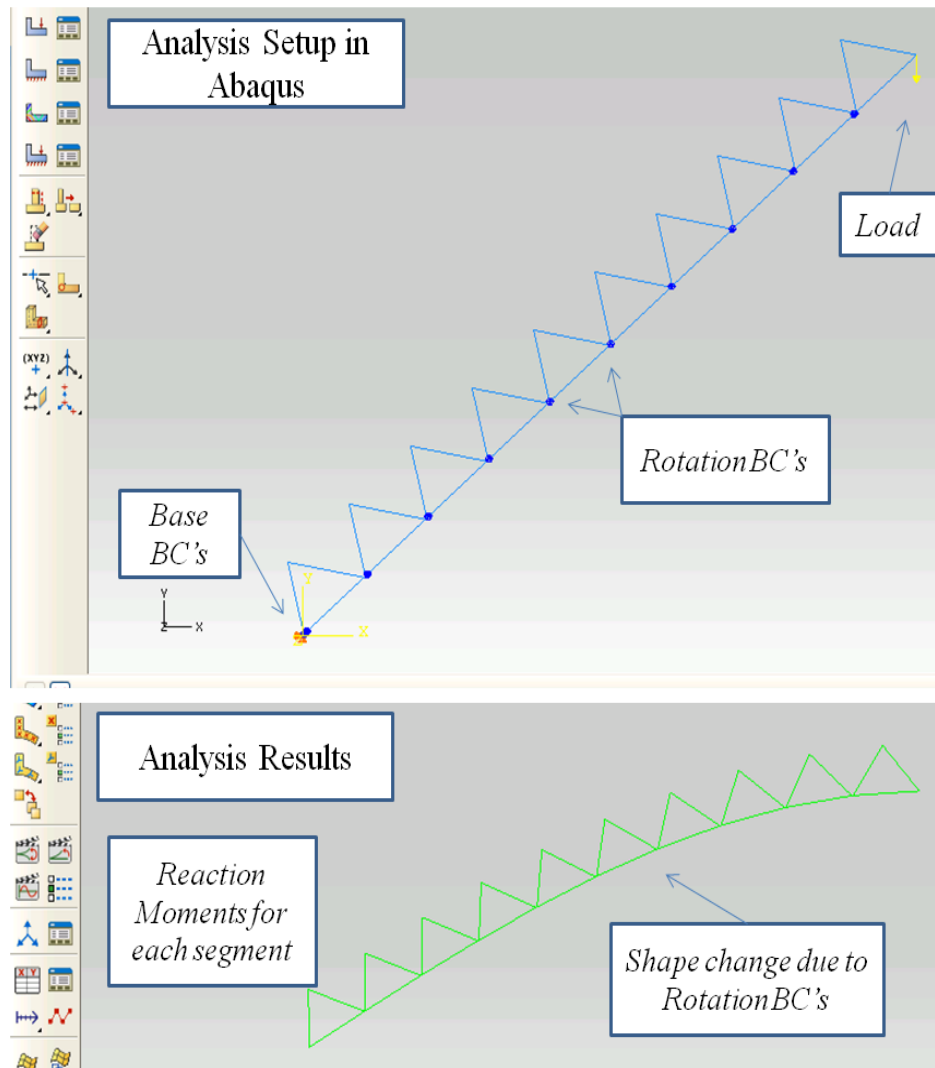


Figure 3.19: Abaqus analysis produced from Python script file and the analysis results.

3.5.5 Step 5: Spring Synthesis

The reaction moment data for each segment, along with the truss displacement data are then used to calculate the required stiffness of each compliant spring as shown in Figure 3.20.

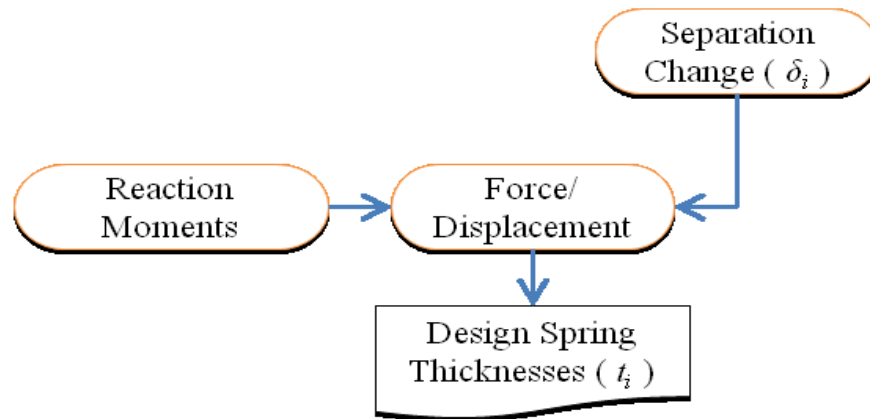


Figure 3.20: Spring synthesis flow chart.

The first objective in this section of the algorithm is to determine the spring forces which must be applied to the segment trusses to recreate the reaction moments caused by the rotation boundary conditions. One of the challenges to finding these forces is that the direction of the applied force will vary from segment to segment depending on the relative angle difference between two adjacent segments. For example, in Figure 3.21, two segments of a morphed structure are shown and the required force, F_M , of the springs must be found which will equal the reaction moment found for segment 2. As the line of force is directly between the two truss points, the direction of the force relative to segment 2 will depend on the relative angle difference between the two segments. The algorithm uses the relative angle, $\theta'1 - \theta'2$, to find the effective distance, h' , of the force used to create a moment about the center of rotation. The resulting moment force is found using Equation 3.4:

Equation 3.4
$$F_{Mi} = \frac{M_{Ri}}{h'_i}$$

Where h' is found using Equation 3.5:

Equation 3.5
$$h'_i = L\sqrt{h_1^2 + 0.5^2} \sin\left(\text{atan}\left(\frac{1}{2h_1}\right) + \frac{\theta'_{i-1} - \theta'_i}{2}\right)$$

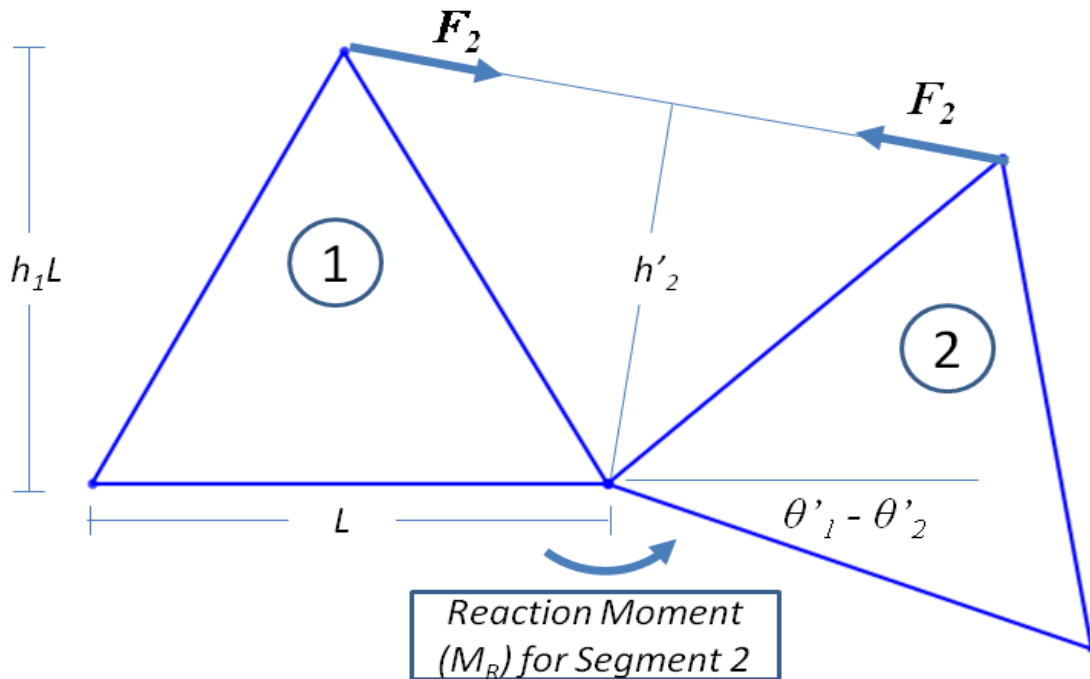


Figure 3.21: Geometry used to find the required spring force from the reaction moment data.

Before the spring thicknesses can be designed, one additional step must be taken to determine the correct force/displacement relationships due to the spring interactions from segment to segment. This is necessary because the force required to create a moment in one segment will produce an opposing moment on the adjacent segment, as can be seen in Figure 3.21, where the force required for segment 2 produces a reaction force in segment 1. The algorithm accounts for the spring interactions by considering the load path of the springs along the structure.

The diagram in Figure 3.22 shows the process used by the algorithm to calculate the required force, F_2 , when the force for segment 3, F_3 , is already known. In this case, there are two separate forces acting at different angles on the truss point of segment 2.

The force, F_2 , must provide enough force to create the required moment in segment 2, M_{R2} , and counteract the opposing force, F_3 , as shown in Figure 3.22A. The reaction moment force vector, F_{M2} , is calculated using Equation 3.4 and Equation 3.5, and the reaction force vector for segment 2, F_2 , is already known. The resulting force is calculated by summing the force vectors along the line of force between segments 1 and 2, as shown in Figure 3.22B, using Equation 3.6.

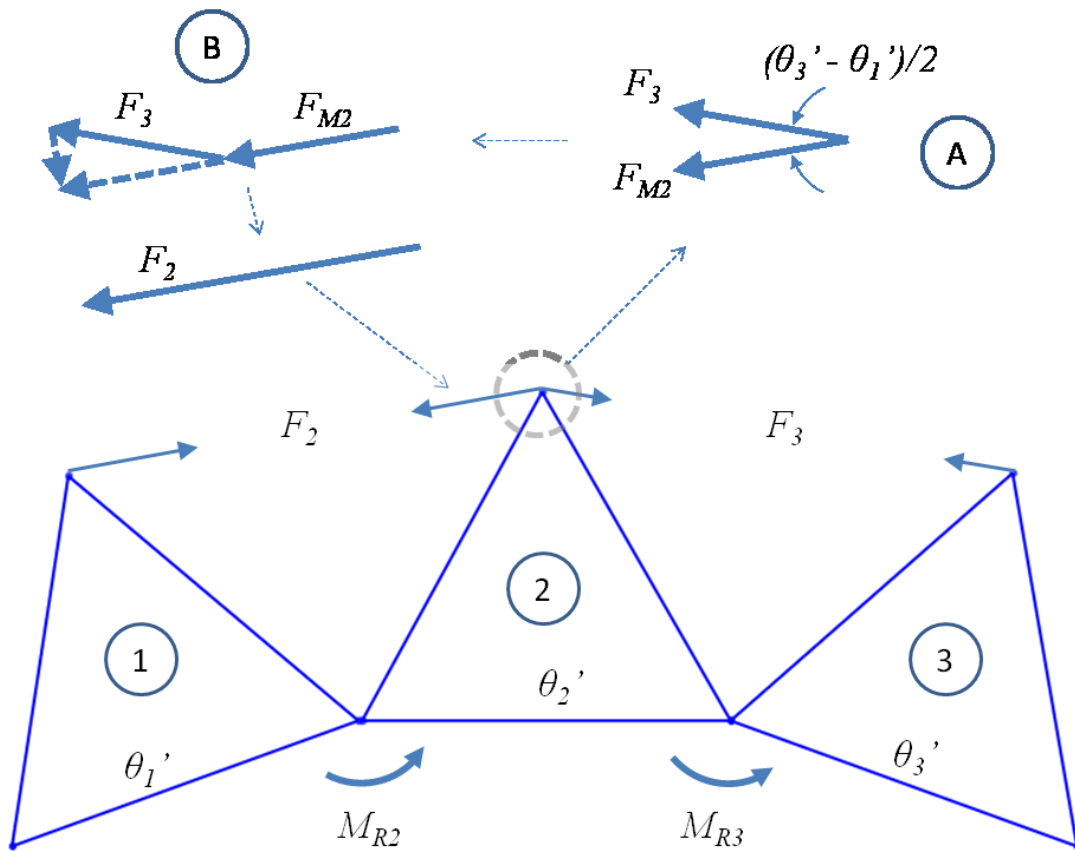


Figure 3.22: Diagram of the process used to account for spring force interactions along the skin structure.

Equation 3.6
$$F_i = F_{Mi} + F_{i+1} \cos\left(\frac{\theta'_{i+1} - \theta'_{i-1}}{2}\right)$$

The load path calculations begin at the free end of the structure where the load is applied and works back to the base of the structure segment by segment. For example, in Figure 3.23 the stiffness of spring 4 is determined first using the reaction moment of segment 4. The stiffness of spring three is determined second, after considering both the reaction moment found for segment three and the additional load caused by spring four. This process continues along the skin from the point of the applied load to the base.

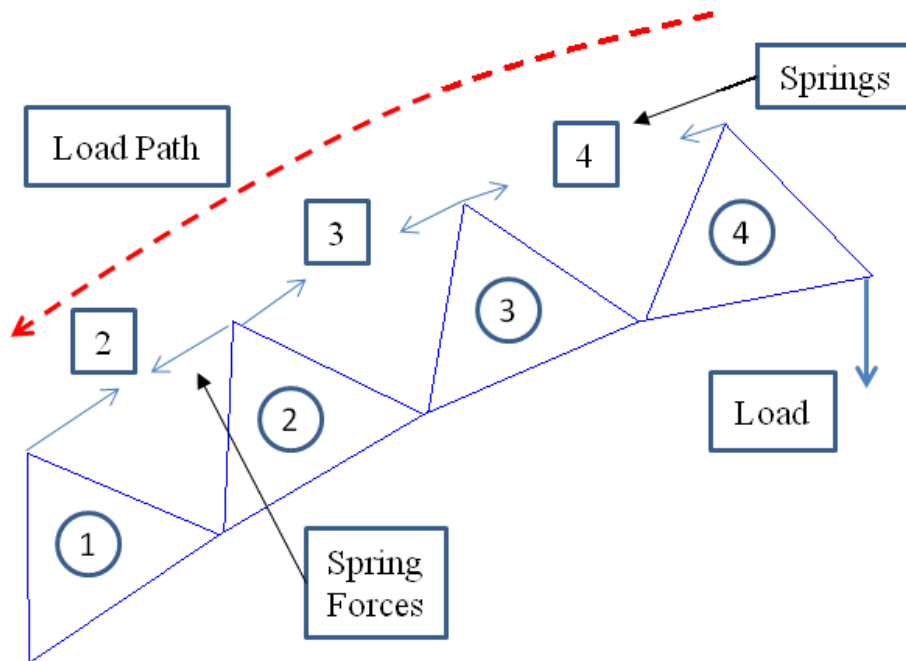


Figure 3.23: Load path used to determine spring stiffness along the skin.

After the spring load path is taken into account, what is left is a series of spring forces which must be present between the segments. The forces are combined with the truss deflections, δ , to create the force-displacement relationships for each spring member.

Before performing stiffness calculations, the algorithm creates the geometry of the spring members based on the input parameter h_2 . The spring geometry is created using the same method used to create the truss member geometries. The only differences for the spring members are that two truss points are used rather than the segment end points to form the base of the structure and the actual geometry of the spring members will vary do to varying truss separations. As the algorithm generates the spring geometries, the lengths and the relative angle between the two spring members are recorded for future analysis.

The spring members are modeled, as shown in Figure 3.6, as two beam members attached at a vertex which are connected to two adjacent truss points using thin compliant hinge members. They are modeled so that relative rotations between the two segments will cause the ends of the beam members to pull apart or push together, creating a resistive force between the two truss points. The use of compliant hinges allows for the beams to be analyzed under the assumption that the beam ends are free to rotate as they are deflected.

As the shape of the compliant spring members is already established based on input parameters and the only remaining variable to design the stiffness of each spring member is the spring thickness. The thickness of each spring is calculated so that the end of one spring member will deflect by the amount $\delta/2$ when the required force for the segment is applied. The algorithm uses Equation 3.7 (40) to solve for the thickness, t .

Equation 3.7:
$$\frac{\delta}{2} = \frac{Fl}{E} \left(\frac{\sin^2(\phi)}{t} + \frac{4L^2 \cos^2(\phi)}{t^3} \right)$$

Where $\delta/2$ is the relative displacement of one leg of the spring, F is the required reaction force, ϕ is the angle of the spring member, l is the length of the spring member, and E is the material Young's modulus.

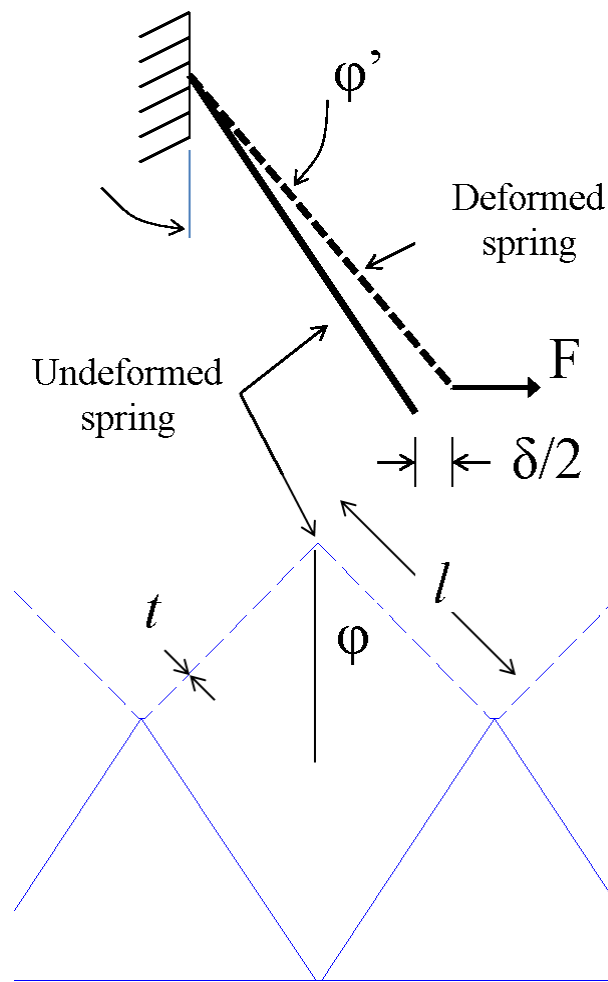


Figure 3.24: Free body diagram used to solve for spring thickness.

Equation 3.7 assumes linear geometry when solving for t , however, the spring members can experience large deformations that can affect the accuracy of the equation. To account for geometric nonlinearities, the springs are evaluated to find t assuming that the spring is in the deformed position. The free body diagram used to calculate the spring

thickness is shown in Figure 3.24, where the dashed line represents the assumed final angle of the spring, φ' , based on the fixed beam length, l , and the deflection, $\delta/2$. By using the assumed deformed angle, φ' , in place of the original spring angle, φ , in Equation 3.7, the linear solution is able to produce spring thicknesses which more accurately supply the required reaction force when deflected by the amount $\delta/2$.

3.5.6 Step 6: Final Structure and Error Analysis

Once all of the spring thicknesses, t_i , in the structure are known, the algorithm modifies the original shape structure used in the first analysis by adding the individual spring elements with their associated thicknesses. A second Python script is created for the new structure in which same load is applied and the rotation boundary conditions are removed. The desired information from this analysis is the actual deflection of each segment in the structure.

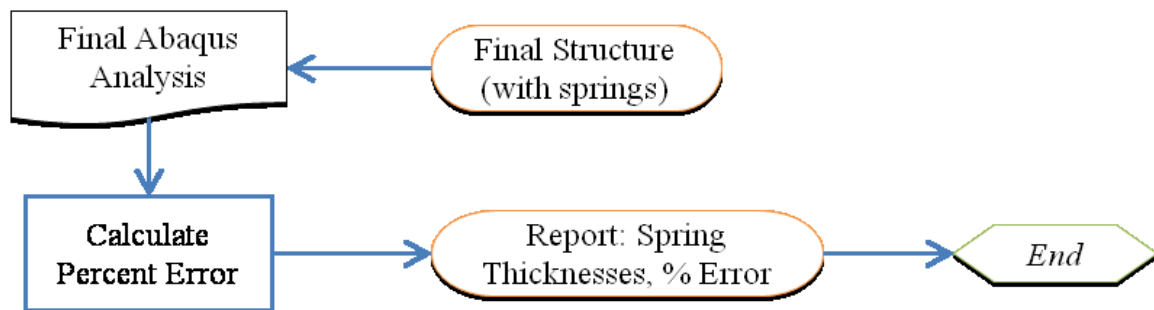


Figure 3.25: Algorithm flow chart for checking the accuracy of the design.

The final step in the algorithm is to calculate the percent error of the actual solution. The range of displacements among the segments can vary greatly and the percent error is calculated as an average error for all segments to prevent large errors as a

result of small desired segment displacements. In Equation 3.8 the percent error is calculated as a ratio of the sum of the absolute distance traveled by each segment and the sum of the absolute separation between the desired final segment locations and the actual final segment locations, where P_i is the position coordinates of the second endpoint of each segment and n is the number of segments.

Equation 3.8:
$$Error = \frac{\sum_{i=1}^n |P_{i_desired} - P_{i_actual}|}{\sum_{i=1}^n |P_{i_original} - P_{i_actual}|}$$

3.6 EXAMPLE PROBLEM: SINUSOIDAL CURVE

This example demonstrates how the direct displacement synthesis method can be used to generate a desired shape change when a load is applied. The initial curve is a straight skin with an initial slope of one which is morphed to a half sinusoidal curve described by the equation:

Sinusoidal Example:
$$y_1 = x, \quad y_2 = 2 \sin\left(\frac{x}{2.9}\right)$$

The two shapes are shown in Figure 3.26. In this example, 20 segments are used, each segment has a length of 0.5m, the heights of the trusses are 0.75 times the length of each segment, the heights of the springs are 0.5 times the length of the segment, the length of the compliant hinge portion of the skin is 0.02 times the length of the segment, and the downward force applied to the end of the skin is 100N.

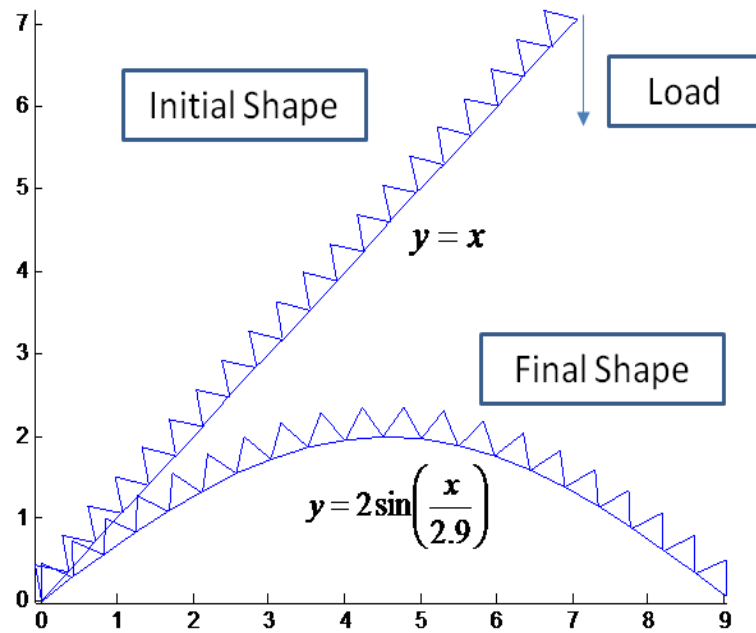


Figure 3.26: Initial and final desired shape with applied load.

In this problem, several of the input parameters are examined to determine their influence on the accuracy of this method. The parameters tested are the direction of the springs, the effective length of the compliant hinges along the skin, and the thickness of the compliant hinges along the skin.

The results from this synthesis method are then compared to the deformation of the same skin when no synthesis method is used. For the non-synthesis results, the thicknesses of the springs are all set to the average thickness found using the synthesis method. The resulting structure simulates how a skin with constant bending stiffness will respond to the applied load.

3.6.1 Algorithm Results

The results from Figure 3.27 show that the direction of the springs has a significant impact on the accuracy of the synthesis method. The model using the inverted springs produces an error of 0.48% and the model with outward springs produces an error of 9.45%.

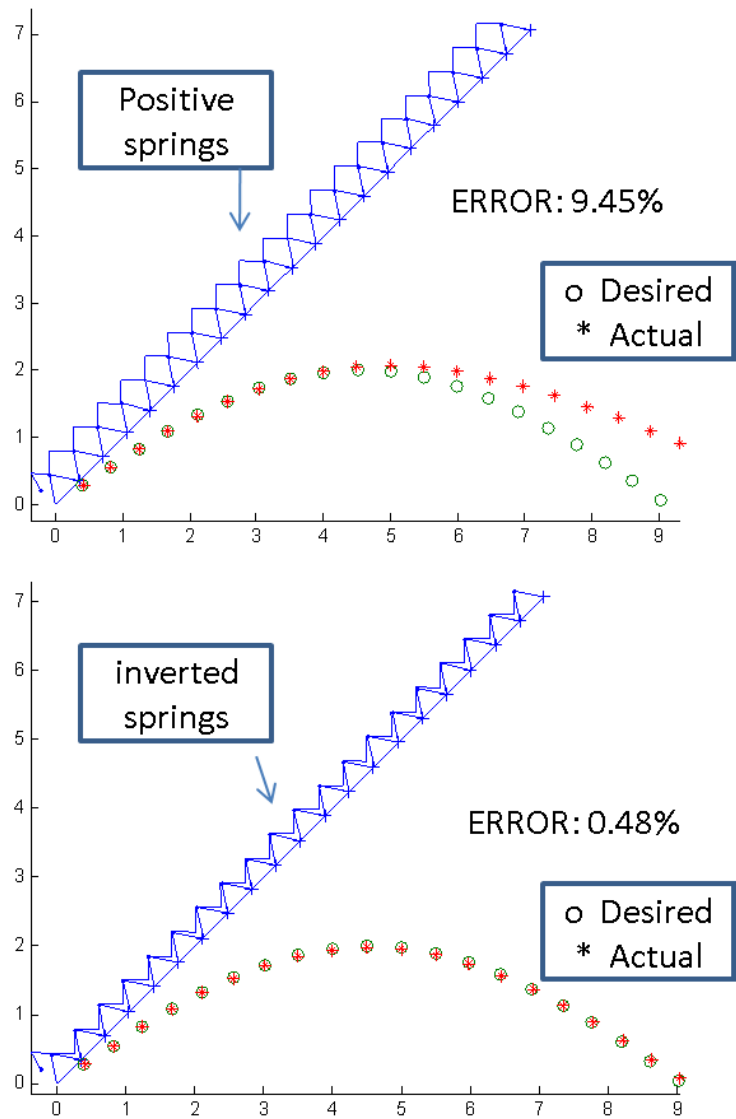


Figure 3.27: Two models synthesized using outward and inverted spring directions.

The results for the influence of the compliant hinges used along the skin are shown in Table 3.1.

3.6.2 Results Data

The results from this study show that the direction of the springs has a large impact on the accuracy of the synthesis method, the length of the compliant hinge sections of the skin have a moderate impact on accuracy, and the thickness of the compliant hinges has little impact. All of the resulting errors from the study are given in Table 3.1.

Table 3.1: Summary of the error results for the structure geometric parameters.

| Geometric Properties | | Error |
|--|----------|-------|
| Spring Orientation ($r_{\text{hinge}}=.02$, Thickness= 2mm) | Outward | 9.45% |
| | Inverted | 0.48% |
| Hinge Thickness ($r_{\text{hinge}}=.02$, Inverted) | 1mm | 0.48% |
| | 2mm | 0.48% |
| | 3mm | 0.55% |
| Hinge Length (r_{hinge}) (Thickness=2mm, Inverted) | 0.01 | 4.32% |
| | 0.02 | 0.48% |
| | 0.03 | 3.22% |

The difference in the results depending on spring direction can be explained by the way the spring thicknesses are determined. Equation 3.7 is used to calculate the force-displacement relationship for a fixed cantilever beam loaded at an angle. It is assumed that the hinge is a free joint with only a point force load and no additional moment loads created at the hinge locations. When the beams are in the outward orientation, the rotation of the segment trusses is in the opposite direction of the natural rotation of the supposedly free end of the beam. This introduces additional moment

loading conditions to the beam that are not accounted for in the synthesis process. When the springs are inverted, the rotation of the segment trusses is in the same direction as the natural rotation of the spring ends. This reduces the effects of additional load conditions at the point where the spring attaches to the trusses, leading to higher accuracy in the synthesis process.

The results for the compliant hinge parameters can also be explained by the formulation of the synthesis process. During the first FEA run, the rotation boundary conditions are applied only to the truss portions of each segment, and not to the hinge sections. When the analysis is run, this compliant section of the skin introduces a small degree of freedom that is not accounted for. The negligible influence of the compliant hinge thickness is a result of the direct displacement analysis step. In the first FEA run, the addition of the compliant hinges results in reaction moment data that is dependent on the influence of the hinge bending moments. That is, the results from this analysis already account for the bending moments caused by the compliant hinges.

To illustrate the effectiveness of the direct displacement method, Figure 3.28 shows the synthesized structure results compared to a non-synthesized result, where the circular points represent the desired locations of the segments and the star points represent the actual segment locations. This figure shows that the direct displacement synthesis method allows for a significant amount of control over how the structure will deform when loaded.

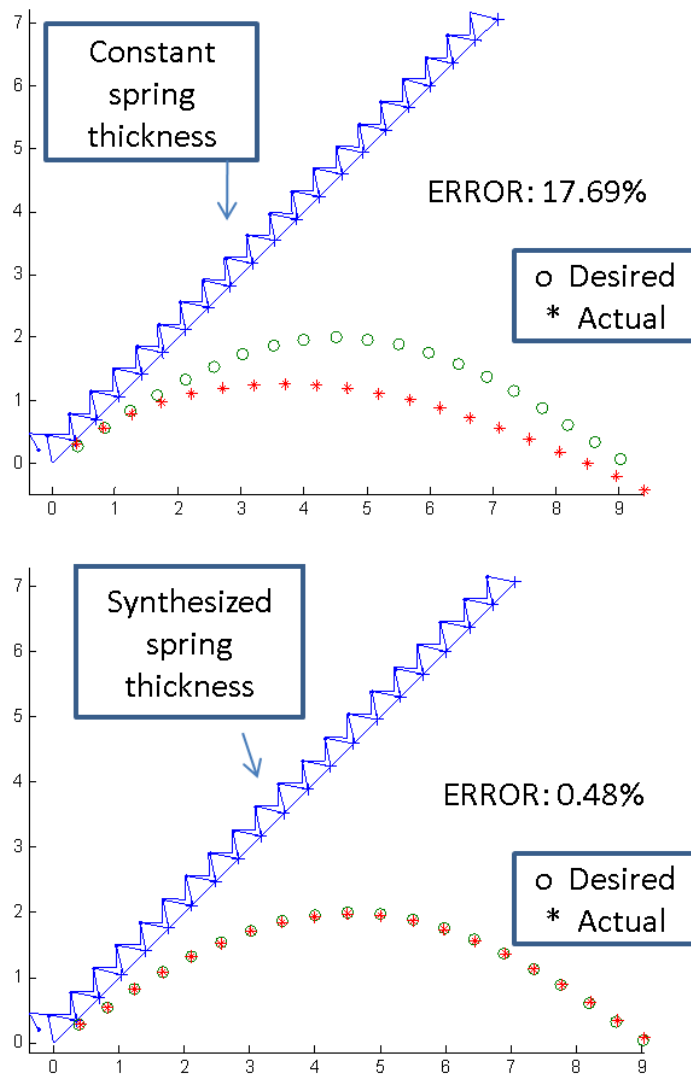


Figure 3.28: Synthesized structure and constant spring thickness structure.

Also, Figure 3.29 shows two additional shape morphing profiles designed using the direct displacement synthesis method with high deformation with errors of around 2.6%.

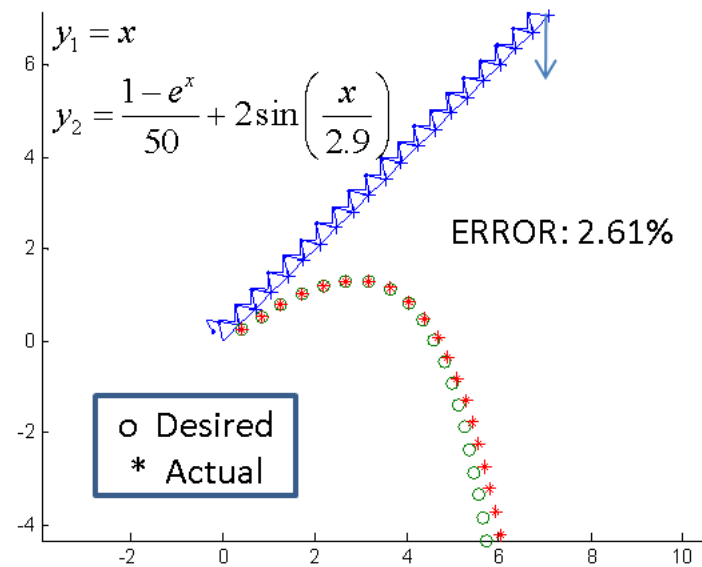
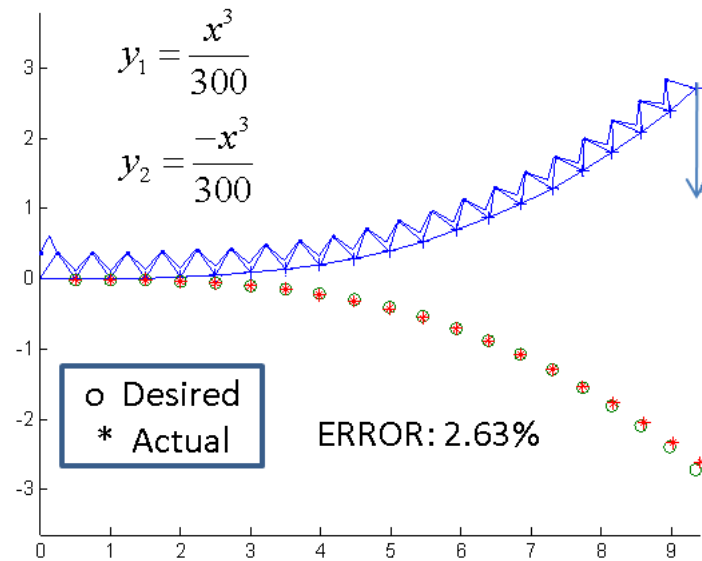


Figure 3.29: Shape morphing profiles designed using direct displacement.

The results from the direct displacement synthesis method show promise for simplifying the synthesis processes used for shape morphing compliant mechanisms. The strength of this method is that it requires no computationally expensive optimization processes and it can generate a direct solution using a single finite element analysis. The

sinusoidal example illustrated that this method is able to synthesis a shape morphing compliant mechanism with 20 control points with an error of 0.48% in one minute.

3.7 MORPHING SKIN DESIGN SUMMARY

Compliant mechanisms have potential to expand the functionalities of products by allowing for precise deformations and shape morphing characteristics unattainable using traditional mechanisms. One challenge with compliant mechanisms is that the use of material deformation makes the synthesis of these structures difficult. Several methods (41; 47) have been devised to improve the efficiency of compliant mechanism synthesis. Thus far, these methods utilize pseudo-rigid-body synthesis and continuum structure synthesis.

The direct displacement synthesis method offers an effective alternative solution for the design of shape morphing skins. This method is capable of synthesizing desired shape change using a direct displacement approach which permits a direct solution. The example of a sinusoidal shape skin illustrates that this method is capable of designing a compliant structure with 20 control points with an error of 0.49%. The entire process, including the accuracy check analysis, takes one minute to complete.

CHAPTER FOUR: CONCLUSIONS AND FUTURE WORK

The use of cellular structures presents many opportunities for the improvement of mechanical design by improving the performance and functionality of design components. Two such cases are discussed in this thesis; the use of cellular structures to achieve desired effective properties which are unattainable using homogenous materials, and the use of cellular skin structure to achieve desired morphing behavior. However, the use of cellular materials presents challenges to the design process due to additional geometry requirements, where the geometry of the material must be designed to facilitate the desired functionality. The objective of the work presented in this thesis is to aid engineers in the challenging task of designing new cellular components by providing them with systematic and automatable design methods.

4.1 HONEYCOMB DESIGN METHOD

The honeycomb design method developed in this thesis is motivated by the Michelin Tweel™, where a cellular material is needed which has a specific effective shear modulus, G_{12}^* , and is able to withstand a specific level of shear strain, $(\gamma_{12}^*)_{max}$, before material yielding occurs. The primary challenge of this design problem is that it is difficult to achieve both high modulus (G_{12}^*) and high compliance $((\gamma_{12}^*)_{max})$ simultaneously as required for the Tweel™. The honeycomb design method is created to achieve both properties under this condition using constituent materials which reduce hysteretic energy loss.

4.1.1 Honeycomb Design Results

The honeycomb design method is developed using two new parameters, R and d , which are dependent on the required overall dimensions, H and L , of the structure and allow for the structural geometry to be modified easily without changing the overall dimensions. It is found through parametric studies that the effective vertical member height, R , and the horizontal separation, d , significantly influence the resulting target property G_{12}^* , but that only one parameter, R , has significant influence on the resulting target property $(\gamma_{12}^*)_{max}$. The relatively small affect of the parameter d on $(\gamma_{12}^*)_{max}$ is used in the method to design the honeycomb geometry in two steps; 1) d is held constant and R is designed to achieve the desired $(\gamma_{12}^*)_{max}$, and 2) the value of R found in step 1 is held constant and d is designed to achieve the desired G_{12}^* resulting in only small changes to the resulting target value for $(\gamma_{12}^*)_{max}$.

A design algorithm is developed to implement the honeycomb design method and is tested for three different target property value combinations. For each target property combination, eight structures having different cell wall thicknesses, t , and number of vertical honeycomb cells, N_v , are designed. The final results of the algorithm tests are as follows; Case 1: ($G_{12}^*=4.25\text{Mpa}$, $10\% < (\gamma_{12}^*)_{max} < 10.5\%$) three of structures are within the target range for $(\gamma_{12}^*)_{max}$, and all of the structures are within 2.6% of the target G_{12}^* , Case 2: ($G_{12}^*=10.25\text{Mpa}$, $6\% < (\gamma_{12}^*)_{max} < 6.5\%$) three of the structures are within the target range for $(\gamma_{12}^*)_{max}$, and all of the structures are within 6.9% of the target G_{12}^* , and Case 3: ($G_{12}^*=2.25\text{Mpa}$, $15\% < (\gamma_{12}^*)_{max} < 15.5\%$) four of the structures are within the target range for $(\gamma_{12}^*)_{max}$, and all of the structures are within 1.4% of the target G_{12}^* .

4.1.2 Honeycomb Design Future Work

In the current form, the honeycomb algorithm is intended to be used as an exploratory tool to generate many initial honeycomb geometry designs having effective properties closely matching the target properties. The resulting designs can then be further developed using more accurate analysis models and the structures can be refined to produce more accurate effective properties. This is due to the simplifications used in the current honeycomb model which uses beam elements and assumes elastic material properties and linear geometry deformation.

Future work on the honeycomb design algorithm will focus on expanding the honeycomb model by including additional material classes, such as elastomers, and through the use of 2D and 3D elements to improve the accuracy of the results. Future work on this topic will also include modifications to the iterative processes in the algorithm to reduce the amount of drift to the resulting $(\gamma_{12}^*)_{max}$ value caused by modifications to the parameter d in the second step of the design method.

4.1.3 Design of Additional Cellular Topologies

The assumptions used in the development of the honeycomb design method were successful in simplifying the design problem so that both target properties can be achieved with an automatable, two step design approach. One of the key aspects of the honeycomb design method is that the assumptions used to develop the method are not limited to the design of hexagonal honeycomb structures and can be adapted for the design of additional cellular topologies. In the current stage of this research, we have

shown that the two step design approach is successful for two structural topologies (honeycomb and bristle). Further research on this topic will examine how successful the basic design approach discussed here can be adapted to develop additional design methods for different cellular topologies.

4.2 MORPHING SKIN DESIGN METHOD

The morphing skin design concept developed in this thesis is motivated by the need for new skin materials to facilitate the requirements of morphing airfoil designs. The objective of this work is to aid in further developments of morphing airfoil design by providing engineers with an additional conceptual design for morphing skins as well as a systematic process to achieve desired properties. The current concept differs from previous design concepts that view morphing skins as passive elements in the design which rely entirely on the morphing characteristics of an internal compliant mechanism. The morphing skin discussed here allows for additional functionality by making the skin an active component in the shape morphing design. This can potentially be used as an additional tool in the design of future morphing airfoils, where both the skin and internal structures are designed to achieve the desired morphing characteristics.

The morphing skin design method developed in this thesis represents a first step, or proof of concept, to show the potential benefits of using direct displacement synthesis for the design of shape morphing structures. As such, the focus of this work has been in developing the basic foundational components of the design method for morphing skins. This includes the development of the geometric framework for morphing skins using rigid triangular truss segments and compliant spring members, and the development of

the direct displacement synthesis steps required to design structures under the most basic conditions, where the skin acts as a cantilever beam with a single load acting on the end.

The results from this work indicate that the direct displacement synthesis method is effective in the design of simple case morphing skins. The results in Figure 3.28 show that a skin structure synthesized using a morphing skin design algorithm is capable of achieving an error of 0.48% with 20 control points, while the same structure with non-synthesized, constant thickness springs results in an error of 17.69%.

The initial success of the morphing skin design method serves as motivation for further development of the direct displacement design approach for morphing structures. Future work on this topic will seek to address several research questions which aim to find the possibilities and limitations of this design approach as it pertains to morphing skins.

4.2.1 Future Work: Additional Loading Conditions

The morphing skin design method, in the current form, is only established for a single force loading condition. While the method is effective in this case, there are limitations to the possible shape morphing characteristics when a single force is used due to the requirement that the skin segments rotations must agree with the moment direction in the structure. These limitations lead to the first research question: **RQ1 – What new shape morphing behaviors are possible when different and/or multiple loading conditions are applied to the skin and how must the design method change to facilitate the additional loads?**

Future work on this topic will seek to answer RQ1 by considering two additional loading conditions, moments and pressure, and studying how these conditions can be used singly or in combinations to facilitate a variety of shape morphing characteristics. For example, future work will explore the possibility of achieving more complex shape morphing characteristics as shown in Figure 4.1, where two combinations of loading conditions, two forces and one force with a moment, may be used to generate shape morphing characteristics which are not possible using a single force load.

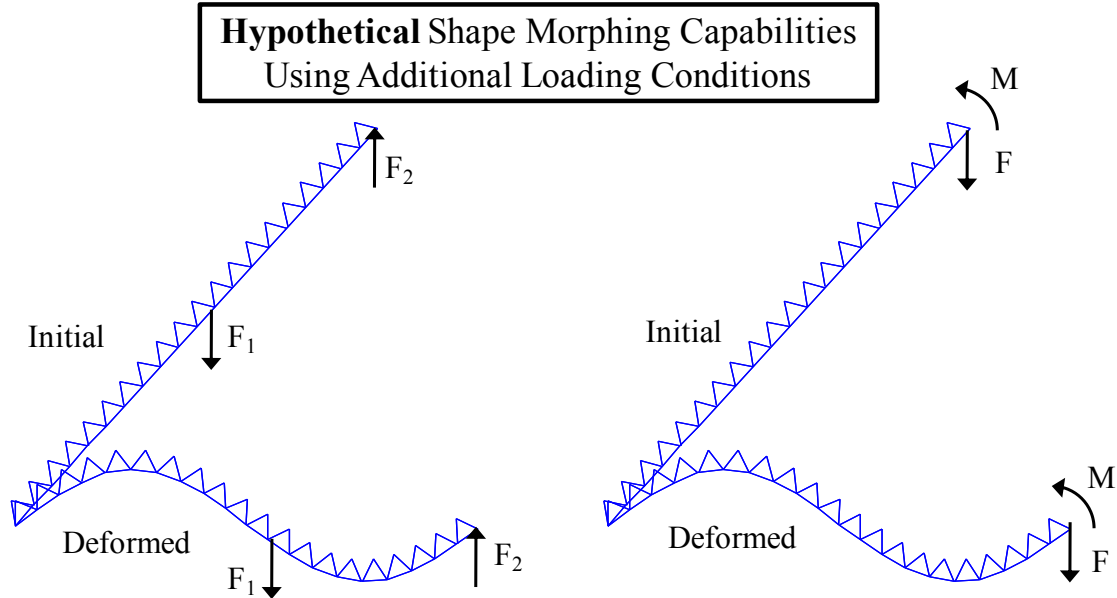


Figure 4.1: Multiple loading conditions used to generate shape morphing characteristics not possible with a single force load condition.

Future work will focus on how each loading condition must be approached in the design method. It is unclear at this time whether the same process used for a single force load, where all loads are applied and the resulting moments are used to design the springs, will be applicable to the new loading conditions. Additional questions also

remain as to how flexible a new design method will be in terms of desired input loads. For instance, in the force-moment structure in Figure 4.1, it is uncertain whether it will be possible to specify both a desired force, F , and a desired moment, M , to produce the desired shape change, or if only a single load may be specified and the additional load must be determined based on the specific shape change characteristics.

The third loading condition, pressure, will be a particular point of focus in future work. As the initial motivation for the morphing skin design concept is for morphing airfoil applications, pressure loading conditions will be of high importance due to the complex pressure loads experienced by airfoils. Apart from airfoil applications, the use of pressure loading conditions and the direct displacement method will be investigated as a tool for contact pressure design applications. For example, in Figure 4.2 a hypothetical morphing skin is desired which will not only morph from a curved shape to a flat shape when a force is applied, but will also produce an uniform contact pressure profile on a flat contact surface. One possible solution to this problem is to apply the desired pressure profile to the direct displacement model which will mimic the load applied to the skin by the surface when in the deformed position. The springs can then be designed with the applied pressure load in an attempt to produce the same pressure profile on the flat surface as shown in Figure 4.2.

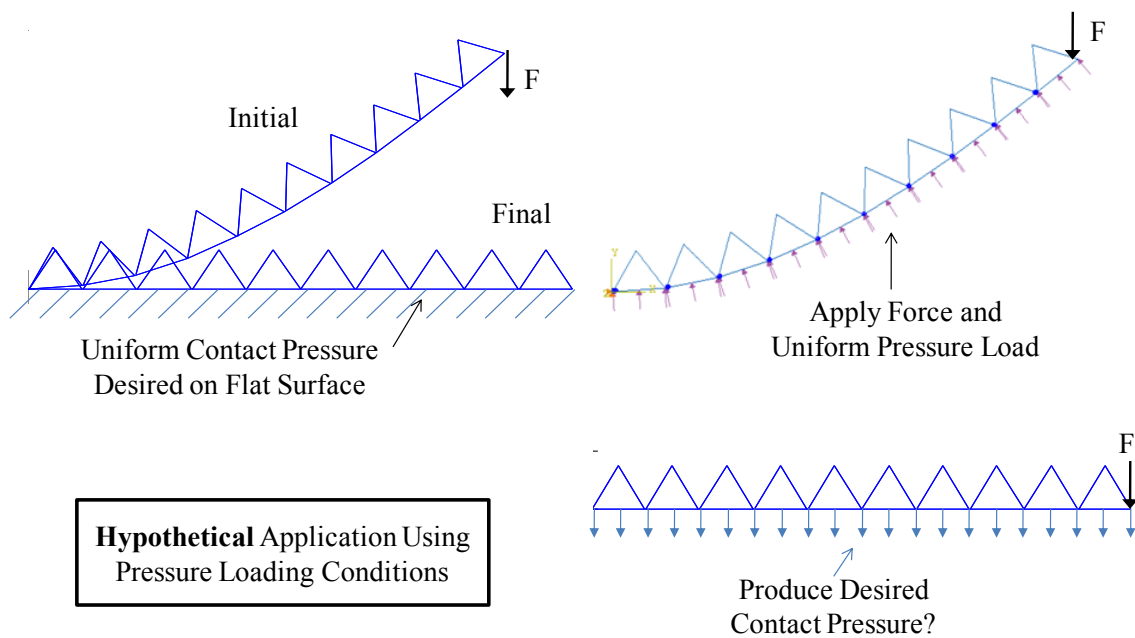


Figure 4.2: Force and pressure loading conditions used to create uniform pressure profile.

4.2.2 Future Work: Closed Profile Skin Structures

All previous discussion on morphing skins has dealt with a skin structure which acts similarly to a cantilever beam, where the base of the structure is anchored at one end and the opposite end is free. However, the goal of this research is to eventually develop a skin based design method for morphing airfoils which have closed profiles as shown in Figure 4.3. The inclusion of closed profile morphing skin structures presents several research questions which will be addressed in future work.

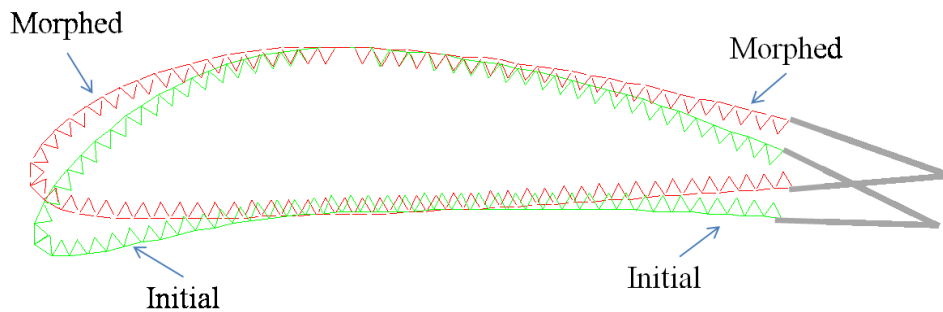


Figure 4.3: Closed profile morphing airfoil structures

The second research question concerns the shape morphing requirements for closed profile structures: **RQ2 – What are the additional shape morphing geometric requirements for closed profile structures and what methods can be employed to meet these requirements?** The open profile skins discussed in this thesis only require that the segment rotations agree with the direction of the applied load. However, for closed profile morphing the skin has no free end, so the morphing behavior must ensure that both the initial profile and the morphed profile having equal skin lengths form closed loops when morphed. That is, the desired morphing behavior must not cause the skin to separate as it changes from one shape to the other. For example, the two skin profiles in Figure 4.3 are attached to a rigid tail section and have equal skin lengths. In order for the desired shape change to be feasible, both ends of the morphed profile skin must attach to the tail section and not result in a separation between the skin and the tail. Future work will seek to develop the methods necessary to satisfy these requirements when two closed profiles are input.

The third research question to be addressed in future work deals with the further development of the morphing skin design method for closed profiles: **RQ3 – Will the**

direct displacement design approach developed for open profile skin synthesis be applicable to closed profile skins, and if so, what modifications to the design approach are necessary for closed profile morphing skins? Future work in this area will investigate how the mechanics of the structure will differ for closed loop structures. In the simple cantilever beam case, the flow of forces through the structure is intuitive for single load, where the global moment throughout the system is continuous in a single direction. The closed profile case is more complex due to the shifting moment direction in the structure required to cause the segments to rotate in either direction based on the desired shape morphing behavior. That is, the new method must be capable of designing not only the magnitude of segment rotation, but also the flow of the global moment through the system to ensure that the individual segments rotate in the correct direction to achieve the desired shape change.

Further work in this area will focus on the integration of additional forces (actuators, additional compliant mechanisms) into the system to control the global moment so that the desired shape change is achievable. The direct displacement method will be studied to determine if it can be used to determine the location and magnitude of additional forces required to produce the correct moment direction throughout the structure. That is, if the initial loading conditions required for a particular application are unable to feasibly create the desired shape change, can the direct displacement method be modified to determine what additional loads are required to make the desired shape change possible. The concept is shown in Figure 4.4 where a possible direct

displacement method generates the location and magnitude of actuator forces required for the desired shape change.

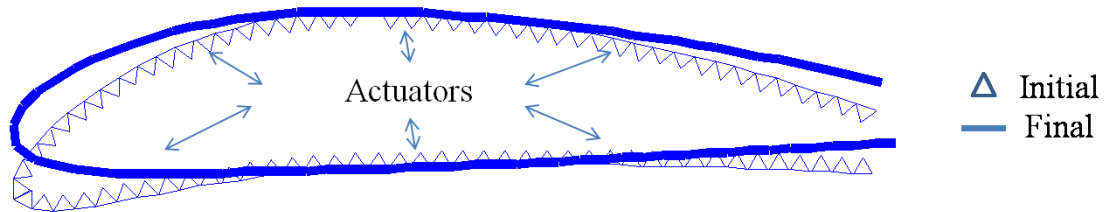


Figure 4.4: Actuator integration to produce desired shape change behavior.

4.2.3 Future Work: Material Stress and Manufacturing

At the current stage of development, the focus of the morphing skin design method has been on the kinematic characteristics of the structure and the basic approach used to design the unknown variables in the system to produce a desired shape change. At this point, material stress limitations, manufacturability and sensitivity are not considered. In future work on the design method the individual design steps discussed here will be modified to account for these issues. The process of designing the spring elements to produce a specific force at a given direction will be a primary focus. In the current process, the geometry of the spring element is fixed at the beginning of the design process and the thickness is designed to produce the desired force and deflection only. In future work, the geometry of the spring elements will be an additional variable in this design step so more flexibility is permitted in the resulting spring thickness values based on material stress and manufacturing limitations.

REFERENCES

1. *Development of a Non-Pneumatic Wheel*. **Rhyne, T. and Cron, S.** (Submitted for Publication) 2005, Tire Science and Technology.
2. *Aluminum Taper Bristle Shaped Shear Band for a Non-pneumatic Tire*. **Berglind, L., Ju, J. and Summers, J.** Akron, OH : The Tire Society, 2010.
3. *Design of Cellular Shear Bands of a Non-Pneumatic Tire –Investigation of Contact Pressure*. **Ju, J., et al.** Detroit, MI : SAE, 2010. 10AC-0108/2010-01-0768.
4. **Ju, J., Summers, J and Czech, C.** *Quarterly Report (Q1 - 2009) Design of Meta-Materials*. s.l. : Clemson University, 2009.
5. *Static Aeroelastic Response of Chiral-core Airfoils*. **Spadoni, A. and Ruzzene, M.** May 2007, Journal of Intelligent Material Systems and Structures.
6. *Design of honeycomb meta-materials for high shear flexure*. **Ju, J., Summers, J. D. and Ziegert, J.:Fadel, G.** San Diego, CA : s.n., 2009. ASME 2009 International Design Engineering Technical Conference, IDETC/CIE.
7. *Design of Chiral Honeycomb Meso-Structures for High Shear Flexure*. **Kolla, A., Ju, J. and Summers, J.** Montreal : ASME, 2010. IDETC 2010/DAC-28557.
8. *Morphing Skins*. **Thill, C., et al.** March 2008, The Aeronautical Journal, p. 3216.
9. *An Automated Design Synthesis Method for Compliant Mechanisms with Application to Morphing Wings*. **Wang, H. and Rosen, D.** Philadelphia, PA : ASME, 2006. Proceedings of IDETC/CIE 2006. pp. DETC2006-99661.

10. *Aircraft Structural Morphing Using Tendon-Actuated Compliant Cellular Trusses*. **Ramrakhiani, D., et al.** 2005, Journal of Aircraft, Vol. 42.
11. **Berglind, L., Summers, J. and Ju, J.** Method for embedding honeycomb structures into an airfoil. *Invention Disclosure presented to CURF*. Clemson, SC : s.n., August, 2009.
12. *The Design of Morphing Aerofoils using Compliant Mechanisms*. **Baker, D. and Friswell, M.I.** 2008. 19th International Conference on Adaptive Structures and Technologies.
13. *An Effective Method of Synthesizing Compliant Adaptive Structures using Load Path Representation*. **Lu, K and Kota, S.** April 2005, Journal of Intelligent Material Systems and Structures, Vol. 16.
14. *Design and application of compliant mechanisms for morphing*. **Kota, S., et al.** 2003, Smart Structures and Materials, Vol. SPIE Vol. 5054.
15. *Synthesis of Adaptive and Controllable Compliant Systems with Embedded Actuators and Sensors*. **Trease, B and Kota, S.** Philadelphia, Pennsylvania : s.n., 2006. Proceedings of IDETC/CIE 2006. pp. DETC2006-99266.
16. *Flexible Skin Development for Morphing Aircraft Applications via Topology Optimization*. **Joo, J. J., Reich, G. W. and Westfall, J. T.** November 2009, Journal of Intelligent Material Systems and Structures, Vol. 20.
17. *Mechanical properties of corrugated composites for candidate materials of flexible wing structures*. **Yokozeki, T., et al.** 2006, Composites Part A: Applied science and manufacturing, Vol. 37, pp. 1578–1586.

18. *Method to Design Honeycombs for a Shear Flexible Structure.* **Berglind, L., Ju, J. and Summers, J.** s.l. : SAE International Journal of Passenger Cars – Mechanical Systems, 2010. 3(1):588-597.
19. **Gibson, L. J. and Ashby, M. F.** *Cellular Solids Structure and Properties.* 2. Cambridge : Cambridge University Press, 1997.
20. *Models for the Elastic Deformation of Honeycombs.* **Masters, I. G. and Evans, K. E.** 1996, Composite Structures, Vol. 35, pp. 403-22.
21. *A Novel Centresymmetric Honeycomb Composite Structure.* **Bezai, A., Scarpa, F. and Remillat, C.** 2005, Composite Structures, Vol. 71, pp. 536-64.
22. *A Refined Model for the Effective in-Plane Elastic Moduli of Hexagonal Honeycombs.* **Balawi, S. and Abot, J. L.** 2008, Composite Structures, Vol. 84, pp. 147-58.
23. *Homogenization of Equivalent in-Plane Properties of Two Dimensional Periodic Lattices.* **Gonella, S. and Ruzzene, M.** 2008, International Journal of Solid and Structures, Vol. 45, pp. 2897-915.
24. *In-Plane Stiffness and Yield Strength of Periodic Metal Honeycombs.* **Wang, A. J. and McDowell, D. L.** 2004, ASME Journal of Engineering Materials and Technology, Vol. 126, pp. 137-56.
25. *Compressive Response and Failure of Circular Cell Polycarbonate Honeycombs under in-plane Uniaxial Stresses.* **Chung, J. and Wass, A. M.** 1999, ASME Journal of Engineering Materials and Technology, Vol. 121, pp. 494-502.

26. *In-Plane Crushing of a Polycarbonate Honeycomb*. **Papka, S. and Kyriakides, S.** 1998, International Journal of Solid Structures, Vol. 35, pp. 239-67.
27. *Elastic Buckling of Hexagonal Chiral Cell Honeycombs*. **Scarpa, F., et al.** 2007, Composites Part A, Vol. 38, pp. 280-9.
28. *Effective Mechanical and Transport Properties of Cellular Solids*. **Torquato, S., et al.** 1, 1998, International Journal of Mechanical Science, , Vol. 40, pp. 71-82.
29. *Thermal Stress and Instability of Sandwich Cylinders on Rigid Supports*. **Gellatry, R. A., Bijlaard, P. P. and Gellaherm, R. H.** 1, 1965, Journal of Aircraft, Vol. 2, pp. 44-8.
30. *The Point Force Response of Sandwich Panels and Its Application to Impact Problems*. **Lin, W.** Salt Lake City, UT : s.n., 1996. 37th Structures, Structural Dynamics, and Materials Conference, AIAA/ASME/ASCE/AHS/ASC.
31. *Closed-Form analysis of the Thickness Effect of Regular Honeycomb Core Material*. **Becker, W.** 2000, Composite Structures, Vol. 48, pp. 67-70.
32. *Static Analysis of Sandwich Panels with Square Honeycomb core*. **Kapania, R. K., et al.** 3, 2008, AIAA Journal, Vol. 46, pp. 627-34.
33. *Thermal Fatigue Analysis of Solar Panel Structure for Micro-satellite Applications*. **Abdelal, G. F. and Atef, A.** 2008, International Journal of Mechanics and Materials in Design, Vol. 4, pp. 53-62.
34. *Study of a Honeycomb-type Rigidified inflatable Structure for Housing*. **Khire, R. A., et al.** 10, 2006, Journal of Structural Engineering, Vol. 132, pp. 1664-72.

35. *Zero-Nu Cellular honeycomb Flexible skins for One-dimensional Wing Morphing*. **Olympio, K. R. and Gandhi, F.** Honolulu, Hawaii : s.n., 2007. 48th Structures, Structural Dynamics, and Materials Conference.
36. *Design and Fabrication of a Passive 1D Morphing Skin*. **Bubert, E. A., et al.** Schaumburg, IL : s.n., 2008. 49th Structures, Structural Dynamics, and Materials Conference.
37. *Multifunctional Topology Design of Cellular Material Structures*. **Seepersad, C. C., et al.** 2008, Journal of Mechanical Design, Vol. 130, pp. 031404-13.
38. *Microstructural Design of Cellular Materials - I: Honeycomb Beams and Plates*. **Huang, J. S. and Gibson, L. J.** 1999, Acta Metallurgica et Materialia, Vol. 43, pp. 1643-50.
39. **Matweb.** SABIC Innovative Plastics Lexan EXRL0627 PC Copolymer. *Matweb.com*. [Online] [Cited: June 13, 2010.] <http://www.matweb.com/search/DataSheet.aspx?MatGUID=a79cb8e83d064d41b83482f4ab00e0c3>.
40. **Cook, R. D. and Young, W. C.** *Advanced Mechanics of Materials*. 2. Upper Saddle River : Prentice Hall Inc., 1999.
41. **Howell, L.** *Compliant Mechanisms*. New York : John Wiley and Sons, 2001.
42. *Design of Compliant Mechanisms for Morphing Structural Shapes*. **Lu, K and Kota, S.** June 2003, Journal of Intelligent Material Systems and Structures, Vol. 14.
43. *Shape Morphing of Aircraft Wing: Status and Challenges*. **Sofla, A. Y. N, et al.** 2009, Materials and Design, Vol. 31, pp. 1284-1292.

44. *Optimal Design of Compliant Trailing Edge for Shape Changing*. **Shili, L., Wenjie, G. and Shujun, L.** 2008, Chinese Journal of Aeronautics, Vol. 21, pp. 187-192.
45. *Analysis of large-displacement compliant mechanisms using an incremental linearization approach*. **Lan, C.** June 2007, Mechanism and Machine Theory.
46. *Compliant mechanism design for realizing of axial link translation*. **Pavlovic, N. T and Pavlovic, N. D.** 2009, Mechanism and Machine Theory, Vol. 44, pp. 1082-1091.
47. *Design and Application of Compliant*. **Kota, S., et al.** November 2005, Journal of Biomechanical Engineering, Vol. 127.
48. *Topology and Dimensional Synthesis of compliant Mechanisms using Discrete Optimization*. **Lu, K and Kota, S.** September 2006, Journal of Mechanical Design, Vol. 128.
49. *A Kinetoelastic Formulation of Compliant Mechanism Optimization*. **Wang, M. Y.** May 2009, Journal of Mechanisms and Robotics, Vol. 1.
50. *Design of compliant mechanisms with selective compliance*. **Hasse, A and Campanile, L.** September 2009, Smart Materials and Structures.
51. *An analysis of the compliant mechanism models*. **Wang, M. Y.** London : s.n., 2009. ASMEFTOMM International Conference on Reconfigurable Mechanisms and Robots.
52. *Direct Displacement-based Seismic Design*. **Priestley, M. J. N., Grant, D. N. and Blandon, C. A.** 2005. NZSEE Conference.
53. **Pang, W. and Rosowsky, D.** *Direct Displacement Procedure for Performance-Based seismic Design of Multistory Woodframe structures*. NEESWOOD. 2007.

54. *Performance-based seismic design of wood framed buildings*. **Filiatrault, A. and Folz, B.** 2002, ASCE Journal of Structural Engineering, pp. 39-47.
55. *The optimization of hierarchical structures with applications to morphing aircraft*. **Friswell, M., et al.** Gijon, Spain : s.n., 2008. Second International Conference on Multidisciplinary Design Optimization and Applications.
56. *Approximating Planar, Morphing Curves with Rigid-Body Linkages*. **Murray, A, Korte, B and Schmiedeler, J.** Ljubljana, Slovenia : s.n., 2006. Proceedings of the 10th International Symposium on Advances in Robot Kinematics.
57. *Rolling Resistance of a Non-Pneumatic Tire having a Porous Elastomer Composite Shear Band*. **Ju, J., et al.** Akron : The Tire Society, 2010.